Coherent Control of Multi-Wave Mixing in Atomic Media

Lou Lan[1], Wen Feng[2], Qin Meng-Zhe[2], He Jia-Nan[2], Zhang Yan-Peng*[2], Xiao Min[3]

1. *Public Security Fire Department of Guangdong Province, Guangzhou 510640, China*
2. *Key Laboratory for Physical Electronics and Devices of the Ministry of Education & Shaanxi Key Lab of Information Photonic Technique, Xi' an Jiaotong University, Xi'an 710049, China*
3. *Department of Physics, University of Arkansas, Fayetteville, Arkansas 72701, USA & National Laboratory of Solid State Microstructures and Department of Physics, Nanjing University, Nanjing 210093, China*

Multi-wave mixing (MWM) is an important nonlinear optical process, and has significant applications in nonlinear optics and quantum information science. This article reviews these advances and recent development in this field. In the frequency domain, the coexistence of four-wave mixing (FWM) and six-wave mixing (SWM) is first experimentally demonstrated via electromagnetically ally induced transparency, and in addition mutual competition with energy as well as exchange spatio-temporal interference is also observed. Furthermore, the enhancement and suppression between the competing FWM and SWM and corresponding Autler-Townes splitting have been experimentally obtained. In the spatial domain, the electromagnetically induced grating resulted from interference between two pump beams is studied, and the related spatial properties (e.g. "shift" and "splitting") of MWM are also involved. Also spatial gap solitons, vortex solitons, charged dipole-mode solitons, and two-dimensional surface solitons are obtained. Such concepts can be extended to quantum area, and the corresponding effects mentioned above can be investigated. The review also includes a discussion of future prospects and application potentials of MWM in cavity QED, the Rydberg states, and all-solid-state quantum computing.

Key words: four-wave mixing; six-wave mixing; electromagnetic induced transparency; cavity; dipole solitons

CLC number : O43 Document Code : A

CONTENTS

Received date: 2012-12-05
*ypzhang@mail.xjtu.edu.cn

I. INTRODUCTION

Enhanced nonlinear processes due to atomic coherence have been experimentally demonstrated in several multilevel atomic systems. The keys to such enhanced nonlinear optical processes include the enhanced nonlinear susceptibility due to the induced atomic coherence and slowed laser beam propagation in the atomic medium, as well as greatly reduced linear absorption of the generated optical field due to electromagnetically induced transparency (EIT)[1,2]. On the other hand, two-photon and three-photon destructive interferences have also been studied in various four-level Y-type[3], N-type[4], and double-type[5,6] atomic systems. The generation of six-wave mixing (SWM) in a closed-cycle N-type system[7] and eight-wave mixing (EWM) in a folded five-level atomic system[8] has been experimentally demonstrated recently. In the previously studied close-cycled (ladder-type, N-type, double-Λ-type, and folded) systems, the four-wave mixing (FWM), SWM, and EWM processes cannot coexist in a given configuration and different order nonlinearities can only be observed individually. In our recent studies, distinctly different from and advantageous over the previously reported SWM processes[7,9], generating highly efficient FWM, SWM, EWM processes simultaneously in an open-cycle Y-type atomic system was experimentally demonstrated[10,11]. We also demonstrated that the third-order and fifth-order nonlinear processes can coexist in open (such as V-type, Y-type, and inverted Y-type) atomic systems. The coexisting SWM processes can become comparable with or even greater than the companion FWM processes in amplitude by manipulating the atomic coherence and multi-photon interferences between different energy levels in the systems[10,12,13]. Such coexistence of FWM and SWM processes allows us to investigate spatio-temporal coherent interference between FWM and SWM processes[14], and to obtain the beat signal between them to get the $\chi^{(5)}$ coefficient. Such a coherent control technique has been used to control the transition probability in atoms[15], photoelectron angular distribution[16], phase-controlled current in semiconductors[17], and various chemical reactions. Also, a fifth-order time-frequency Raman spectroscopy technique was used to study the two-quantum transition or Raman overtone for the rephasing pathway[18].

As two or more laser beams propagate through an atomic medium, the cross-phase modulation (XPM), as well as the modified self-phase modulation (SPM), can significantly affect the propagations and spatial patterns of the traveling laser beams. Self-focusing[19], deflection[20], breaking[21], and pattern formation[22,23] of laser beams have been extensively studied with two laser beams propagating in two-level atomic vapors. It has been shown that the self- and cross-Kerr nonlinearities can be significantly enhanced and modified in three-level atomic systems due to laser induced atomic coherence or EIT[24~26]. At the same time, enhanced FWM[5], EIT-induced waveguide effect[26], as well as elimination of beam filamentation[27,28] were observed in atomic system. Such sharp nonlinear dispersions in frequency domain of EIT systems can be converted into spatial domain for probe and FWM signals[24,29], which exactly mimics the dispersion curve for the Kerr nonlinear index of refraction controlled by the strong coupled laser beam. Also, spatial splits of degenerate and non-degenerate FWM signals have been theoretically simulated and experimentally demonstrated[30]. Such electromagnetically induced spatial dispersion (EISD) can be used for spatial switching and routing, and as an easy way to measure the Kerr-nonlinear indices of refraction for the multi-level atomic media.

Spatial optical soliton[31] is formed when the spatial diffraction is balanced by either the self-focusing effect due to the self-Kerr nonlinearity or the cross-focusing effect due to strong XPM nonlinearity[32]. In recent years, new type spatial solitons, such as discrete solitons[34,34], gap solitons[35] have been investigated (both theoretically and experimentally) in waveguide arrays, fiber Bragg gratings[36], Bose-Einstein condensates[37], and photorefractive crystals[33,34]. Band gaps of the linear spectra are essential for the formation of the gap solitons, which is originated from the periodical structure in fiber Bragg gratings, photonic crystals[28], and even the standing wave in an atomic ensemble[38]. Therefore, large refractive index modulations are needed either by fixed periodic structures (such as waveguide arrays) or reconfigurable optical lattices induced by laser beams. Vortex soliton is generated in a self-defocusing medium owing to the counterbalanced effects of diffraction and nonlinear refraction at the phase singularity[39]. Several interesting effects including cascade generation of multiple charged optical vortices and helically shaped spatio-temporal solitons in Raman FWM, and coupled vortex solitons supported by cascade FWM in a Raman active medium excited away from the resonance have been investigated[40,41]. Spatial solitons can split into two parts with opposite phases, if a phase delay for half of the soliton beam is in-

troduced, which is called dipole-mode vector soliton with a Hermite-Gaussian mode structure[42]. In an optically induced two-dimensional photonic lattice, dipole-mode solitons can be created with either opposite phases or same phase between the two parts[43]. Vector solitons with one nodeless fundamental component and another dipole-mode component can couple to each other and be trapped jointly in the photonic lattices[42,44,45]. A radially symmetric vortex soliton can decay into a radially asymmetric dipole-mode soliton with a nonzero angular momentum, which can survive for a very long propagation distance[42]. Surface soliton is formed at the edge of two mediums[37,45~49]. Different from the case with two uniform media, the trapping mechanism for optical surface waves formed at the interface of uniform media and periodical refractive index media is that the propagation eigenvalues fall within the photonic band gap (PBG) of the system[37,50]. There are many new interesting features in optical surface waves with different kinds of nonlinearities, such as nonlocal surface solitons[51], polychromatic surface solitons[52], and spatio-temporal surface light bullets[53]. As an example, one-dimensional (1D) in-phase surface solitons in the AlGaAs array[54] and two-dimensional (2D) discrete surface solitons forming at the corner of a finite optically-induced 2D waveguide lattice and a continuous medium have been experimentally observed[55,56]. To systematically investigate these interesting phenomena, it is important to construct a medium with flexible periodic nonlinearity. Until now, enhanced by laser-induced atomic coherences, spatial gap solitons[57], vortex solitons[24,29], charged dipole-mode solitons[58], as well as 2D surface solitons are experimentally observed in atomic media.

Investigations on the interactions of doubly dressed states and the corresponding effects of atomic systems have attracted many researchers in recent years. The interaction of double-dark states (nested cascade scheme of doubly dressing) and splitting of a dark state (the secondarily dressed states) were studied theoretically in a four level EIT atomic system by Lukin *et al.*[59]. Later, the triple-peak absorption spectrum, which was observed in the N-type cold atomic system by Zhu *et al.*, verified the existence of the secondarily dressed states in the nested-cascade scheme[60]. A similar result was obtained in the inverted-Y system[61,62]. The doubly dressed FWM (DDFWM) in the nested-cascade with close-cycled atomic system[63], parallel and nested-cascade schemes in an open five-level atomic system was reported[64]. After that, the similarities and differences among these different dressing schemes are studied in detail[65]. Enhancement and suppression between the competing FWM[66] and SWM[67] processes, as well as the Autler-Townes (AT)[68,69] splitting have been experimentally observed. In addition, due to the interactions of doubly dressed states, probe transmission, FWM and fluorescence signals are allowed to transmit through the atomic medium, and ultra-narrow two-photon fluorescence signal is obtained in a ladder or Y-type atomic system[70].

In the investigation of non-classical optics, for many decades, spontaneous parametric down conversion (SPDC) in nonlinear crystals has been used as the standard method to generate nonclassical correlated photons. Recently, much research interest has been drawn to the production of photons with MWM process. By simultaneously creating a destructive interference in absorption and a constructive interference in the nonlinear susceptibility, Harris demonstrated the first FWM experiment in cold atoms[71], where the generated weak Stokes and anti-Stokes fields counterpropagate through an optically thick atomic medium with backward-wave geometry. Following, Lukin[72] and Kimble[73] realized, controllable counter-propagating waveforms[74] and narrow-bandwidth[75] paired photons with FWM process, and then two-photon interference of paired photons with time-frequency and polarization entanglement is achieved[76]. FWM process in a hot vapor cell can be used as the basis for constructing a variety of interesting quantum processing devices: a source of spatially broadband twin beams[77], a low noise amplifier for quantum states[78], a device to produce entangled images[79], and a delay line for a portion of an entangled quantum state[80], noiselessly amplify complicated 2D images[81] as well as stimulated superluminal pulses with negative group velocities[82]. Moreover, studies on strong coupling between atoms and cavity field have been very active due to the importance in fundamental and potential applications in quantum computation and quantum information processing. Normal-mode splitting in ensembles of cold atoms[83,84] and hot atomic vapor cell have been observed[85,86]. Furthermore, the triply-resonant atom-cavity system has been experimentally demonstrated[87]. On one hand, quantum correlated bright light beams have been also produced with SPDC inside an optical cavity above its threshold[88], however, they suffer from the low production rate and short correlation time for their broad bandwidths[89]. Todate, generating correlated photon pairs by large photon pair-generation rate with the help of an optical cavity[90], entanglement amplifier based on two-mode correlated emission lasers[91], and bright correlated beams by manipulating the large dispersion of the intra-cavity medium[92] have been also experimentally studied. On the other hand, the nonlinear processes involved the high-excited Rydberg states have attracted a lot of attention. Specifically, dramatic sup-

pression of ultracold atoms to Rydberg states by laser excitation has been experimentally demonstrated[93], where Rydberg atoms strongly inhibit excitation of their neighbors. Thus, with strong Rydberg-level interactions, single-quantum excitation of a cold atomic gas is fast prepared, where no more than a single excitation was retrieved[94].

Throughout this review, we present the coherent control of MWM that arises as a result of EIT and describe some recent progresses in outline. In the frequency domain, the coexistence of MWM and spatio-temporal interference will be discussed. Then, the enhancement and suppression of coexisting MWM signals as well as the corresponding AT splitting are presented. In the spatial domain, EISD which can be used for describing spatial "shift" and "splitting" of MWM-, as well as some types of spatial solitons is discussed. Future prospects and new application potentials of MWM in cavity quantum electrodynamics (QED) and Rydberg blockade are introduced at last.

The review is constructed as follows: in Sec. II, we introduce the fundamental theories of nonlinear susceptibility, undressed MWM and the fundamental concept of enhancing MWM by dressing effect; in Sec. III, we discuss the generating highly-efficient coexisting FWM, SWM and EWM nonlinear processes, temporal and spatial interferences between FWM and SWM processes in detail; in Sec. IV, we treat the spatial coherent control of MWM and review the spatial modulation of FWM signal by the EISD in an atomic medium, including the "shift" and "splitting" of MWM, spatial gap solitons, vortex solitons, charged dipole-mode solitons, as well as 2D surface solitons. Furthermore, the utility of the interactions between doubly-dressed states and the corresponding effects is discussed; in Sec. V we turn to the treatment of the fluorescence accompanying with MWM, the MWM in cavity, Rydberg MWM, in which the middle case need the consideration of MWM in few-photon level, where it is necessary to apply a fully quantum treatment of the fields. Finally in Sec. VI, we draw conclusions and discuss future prospects in quantum optics and nonlinear optics as a result of coherent control of MWM.

II. ENHANCED HIGH-ORDER NONLINEAR SUSCEPTIBILITY

A. Nonlinear Susceptibility

In order to describe an optical nonlinearity more precisely, we consider how the dipole moment per unit volume, or polarization $\mathcal{P}$ a medium depends upon the strength of the applied optical field $\boldsymbol{E}$. The induced polarization depends nonlinearly upon the electric field strength described by the relationship $\mathcal{P} = \mathcal{P}_L + \mathcal{P}_{NL}$. Here, $\mathcal{P}_L = \mathcal{P}^{(1)}$, $\mathcal{P}_{NL} = \mathcal{P}^{(2)} + \mathcal{P}^{(3)} + \cdots = \varepsilon_0(\boldsymbol{X}^{(2)} : \boldsymbol{EE} + \boldsymbol{X}^{(3)} \vdots \boldsymbol{EEE} + \cdots)$.

In nonlinear optics, the optical susceptibility can be generally expressed as, $\chi = \sum_{j=0}^{\infty} \chi^{(2j+1)}|E|^{2j}$. The constant of proportionality $\chi^{(1)}$ is known as the linear susceptibility. The quantities $\chi^{(2)}$ and $\chi^{(3)}$ are known as the second- and third-order nonlinear optical susceptibilities, respectively.

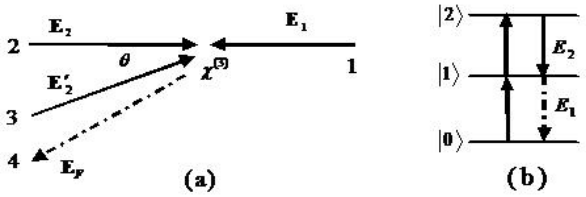

FIG. 1. (a) Schematic diagram for the phase-conjugate FWM process. (b) Energy-level diagram for FWM in a close-cycled three-level cascade system

As an important nonlinear phenomenon, in the weak interaction limit, FWM is a pure third-order nonlinear optical process and is governed by the third-order nonlinear susceptibility. Let us consider a special case of FWM processes, which involves three laser fields $\boldsymbol{E}_1$ $(\boldsymbol{k}_1, \omega_1)$, $\boldsymbol{E}_2$ $(\boldsymbol{k}_2, \omega_2)$ and $\boldsymbol{E}_2^{'}$ $(\boldsymbol{k}_2^{'}, \omega_2)$. Here, ω_i and $\boldsymbol{k}_i$ represent the corresponding frequency and wave vector, respectively. And there is a small angle θ between the input pump laser beams $\boldsymbol{k}_2$ and $\boldsymbol{k}_2^{'}$. The probe laser beam $(\boldsymbol{k}_1)$ propagates along a direction that is almost opposite to that of the beam $\boldsymbol{k}_2$ (see Fig. 1). The corresponding nonlinear atomic polarization $\mathcal{P}_3$ along the i $(i = x, y)$ direction, from first-order perturbation theory, is given by

$$\mathcal{P}_i^{(3)}(\omega_i) = \varepsilon_0 \sum_{jkl} \chi_{ijk}^{(3)} E_{1j}(\omega_1) E_{2k}^{'*}(\omega_2) E_{2l}(\omega_2) \quad (1)$$

where the third-order susceptibility contains the microscopic information about the atomic system. The susceptibility of the nonlinear tensor $\chi_{ijkl}^{(3)}(\omega_F; \omega_1, -\omega_2, \omega_2)$ is also related to the polarization components of the incident and generated fields. For an isotropic medium, as in the atomic vapor, only four elements are not zero and they are related to each other.

For the generated SWM signal, the fifth-order nonlinear polarization along the i $(i = x, y)$ direction is then given by

$$\mathcal{P}_i^{(5)}(\omega_1) = \varepsilon_0 \sum_{jklmn} \chi_{ijklmn}^{(5)} E_{1j}(\omega_1) E_{2k}^{'*}(\omega_2) E_{2l}(\omega_2) E_{3m}^{'*}(\omega_3) E_{3n}(\omega_3) \tag{2}$$

where $\chi_{ijklmn}^{(5)}$ is the fifth-order nonlinear susceptibility. For an isotropic medium, there are sixteen nonzero components and only fifteen of them are independent.

B. FWM Grating

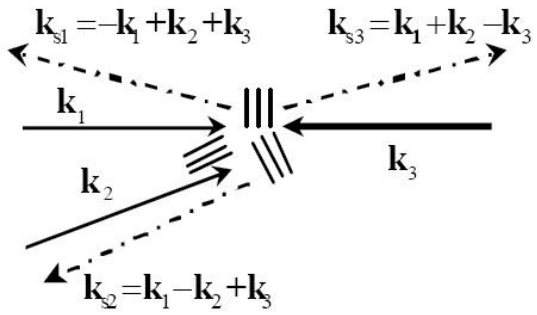

FIG. 2. Schematic diagram of phase-conjugate FWM

As we know in section A, FWM is governed by third-order nonlinear susceptibility in the weak interaction limit. Unlike second-order process, the third-order process can exist in all media. We now consider a special case of FWM processes with beams $\boldsymbol{E}_1(\omega_1, \boldsymbol{k}_1)$, $\boldsymbol{E}_2(\omega_2, \boldsymbol{k}_2)$ and $\boldsymbol{E}_3(\omega_3, \boldsymbol{k}_3)$. There exists a small angle θ between beams $\boldsymbol{k}_2$ and $\boldsymbol{k}_1$. The probe beam ($\boldsymbol{k}_3$) propagates along a direction that is almost opposite to that of beam $\boldsymbol{k}_1$ (Fig. 2). Third-order nonlinear susceptibility can be triply resonant if ω_i is near their respective resonance. Such third-order process is even observable with CW laser beams for the strong resonant enhancement. The output of FWM can be easily understood if two of the three input waves interfere and form either a static grating or a moving grating, which scatters the third input wave to yield the output wave. As illustrated in Fig. 2, the grating formed by $\boldsymbol{k}_1$ and $\boldsymbol{k}_2$ scatters $\boldsymbol{k}_3$ yields outputs $\boldsymbol{k}_3 \pm (\boldsymbol{k}_1 - \boldsymbol{k}_2)$. Altogether, three output waves with different wave vectors, $\boldsymbol{k}_{s1} = -\boldsymbol{k}_1 + \boldsymbol{k}_2 + \boldsymbol{k}_3$, $\boldsymbol{k}_{s2} = \boldsymbol{k}_1 - \boldsymbol{k}_2 + \boldsymbol{k}_3$, and $\boldsymbol{k}_{s3} = \boldsymbol{k}_1 + \boldsymbol{k}_2 - \boldsymbol{k}_3$, can be expected. However, only $\boldsymbol{k}_{s2} = \boldsymbol{k}_1 - \boldsymbol{k}_2 + \boldsymbol{k}_3$ always satisfies the phase-matching condition ($\Delta \boldsymbol{k}_{s2} = 0$). More specifically, if $\boldsymbol{k}_1$ and $\boldsymbol{k}_2$ have the same frequency (i.e. $\omega_1 = \omega_2$) with a small angle θ between them, the coherence length of FWM signal at $\boldsymbol{k}_{s2}$ is given by $l_c^f = 2c/[n(\omega_1/\omega_3)|\omega_1 - \omega_3|\theta^2]$, which is much larger than that of the other two. Here, the nonlinear interaction between $\boldsymbol{k}_1$ and $\boldsymbol{k}_2$ with an absorbing medium gives rise to the molecular-reorientation and the thermal non-resonant static gratings (i.e. $Q_{\rm M}$ and $Q_{\rm T}$), respectively. If the frequency difference $\Delta_a = \omega_3 - \omega_1 \approx 0$, two resonant moving gratings $Q_{\rm RM}$ and $Q_{\rm RT}$ with large angle are formed by the interference between $\boldsymbol{k}_2$ and $\boldsymbol{k}_3$. Beam $\boldsymbol{k}_1$ is diffracted by them to enhance the FWM signal. Thus, we get the Rayleigh-enhanced FWM with wave vector $\boldsymbol{k}_{s2}$ along the direction of $\boldsymbol{k}_4$. While, if the frequency difference $\Delta_b = \omega_3 - \omega_1 - \Omega_{\rm R} \approx 0$ ($\Omega_{\rm R}$ is the Raman resonant frequency), one large resonant moving grating, $Q_{\rm R}$ formed by the interference between $\boldsymbol{k}_2$ and $\boldsymbol{k}_3$ will excite the Raman-active vibrational mode of the medium and enhance the FWM signal (i.e., Raman-enhanced FWM).

C. Generalized Resonant MWM

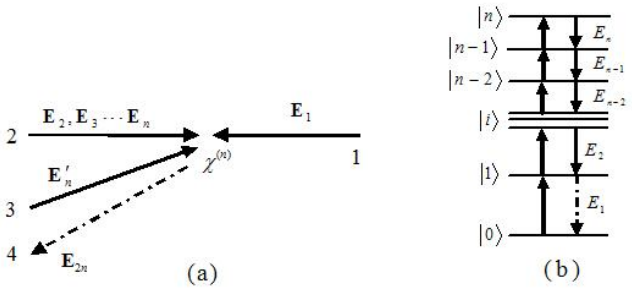

FIG. 3. (a) Schematic diagram of phase-conjugate doubly-dressed ($2n$) WM. (b) Energy-level diagram for ($2n$) WM in a closed-cycle $(n+1)$-level cascade system

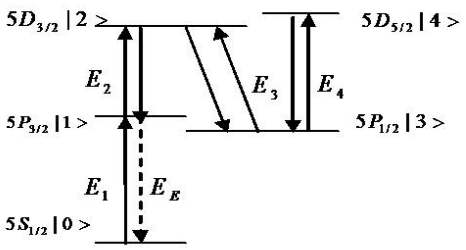

FIG. 4. Energy-level diagram of a closed-cycle five-level atomic system

The atomic coherence effects can be used to enhance both the FWM process and even higher order nonlinear process as well. In this section, we will introduce the EIT assisted higher order nonlinear process. The mathematical structure of the $(2n)$ WM can be obtained with density matrix dynamic equations. First of all, we obtain $\partial\hat{\rho}(t)/\partial t = [\hat{H}_0 + \hat{H}_1(t), \hat{\rho}(t)]/i\hbar - \Gamma\hat{\rho}$, where $\hat{H}_1 = -E\hat{\mu}$ and $\hat{\rho}(t)$ can be expanded as $\hat{\rho}(t) = \hat{\rho}^{(0)}(t) + \hat{\rho}^{(1)}(t) + \hat{\rho}^{(2)}(t) + \cdots + \hat{\rho}^{(r)}(t) + \cdots$.

Therefore we get

$$i\hbar\frac{\partial}{\partial t}[\hat{\rho}^{(0)}(t) + \hat{\rho}^{(1)}(t) + \hat{\rho}^{(2)} + \cdots + \hat{\rho}^{(r)}(t) + \cdots] = [\hat{H}_0 + \hat{H}_1, \hat{\rho}^{(0)}(t) + \hat{\rho}^{(1)}(t) + \hat{\rho}^{(2)} + \cdots + \hat{\rho}^{(r)}(t) + \cdots] - i\hbar[\hat{\rho}^{(0)}(t) + \cdots + \hat{\rho}^{(r)}(t) + \cdots] \quad (3)$$

The series $\rho^{(0)} \cdots \rho^{(r)}$ can be obtained by solving the following equations step by step.

$$\frac{\partial\rho_{10}}{\partial t} = \frac{1}{i\hbar}[\rho_{10}(E_1 - E_0) - E(-\mu_1\rho_{11} + \mu_1\rho_{00} + \mu_2\rho_{20})] - \Gamma_{10}\rho_{10} \quad (4\text{-}1)$$

$$\frac{\partial\rho_{20}}{\partial t} = \frac{1}{i\hbar}[\rho_{20}(E_2 - E_0) - E(-\mu_1\rho_{21} + \mu_2\rho_{10} + \mu_3\rho_{30})] - \Gamma_{20}\rho_{20} \quad (4\text{-}2)$$

$$\vdots$$

$$\frac{\partial\rho_{n-1,0}}{\partial t} = \frac{1}{i\hbar}[\rho_{n-1,0}(E_{n-1} - E_0) - E(-\mu_1\rho_{n-1,1} + \mu_{n-1}\rho_{n-2,0} + \mu_n\rho_{n,0})] - \Gamma_{n-1,0}\rho_{n-1,0} \quad (4\text{-n-}1)$$

$$\frac{\partial\rho_{n,0}}{\partial t} = \frac{1}{i\hbar}[\rho_{n,0}(E_n - E_0) - E(-\mu_1\rho_{n,1} + \mu_n\rho_{n-1,0})] - \Gamma_{n,0}\rho_{n,0} \quad (4\text{-n})$$

Next, we consider a five-level atomic system in Fig. 4 as a practical example for the above derivation. So, we can obtain the following equations

$$\frac{\partial\rho_{10}}{\partial t} = \frac{1}{i\hbar}[\rho_{10}(E_1 - E_0) - E(\mu_1\rho_{00} + \mu_2\rho_{20} - \mu_1\rho_{11})] - \Gamma_{10}\rho_{10} \quad (5\text{-}1)$$

$$\frac{\partial\rho_{20}}{\partial t} = \frac{1}{i\hbar}[\rho_{20}(E_2 - E_0) - E(\mu_2\rho_{10} + \mu_3\rho_{30} - \mu_1\rho_{21})] - \Gamma_{20}\rho_{20} \quad (5\text{-}2)$$

$$\frac{\partial\rho_{30}}{\partial t} = \frac{1}{i\hbar}[\rho_{30}(E_3 - E_0) - E(\mu_3\rho_{20} + \mu_4\rho_{40} - \mu_1\rho_{31})] - \Gamma_{30}\rho_{30} \quad (5\text{-}3)$$

$$\frac{\partial\rho_{40}}{\partial t} = \frac{1}{i\hbar}[\rho_{40}(E_4 - E_0) - E(\mu_4\rho_{30} - \mu_1\rho_{41})] - \Gamma_{40}\rho_{40} \quad (5\text{-}4)$$

In the bare-state picture, the atomic polarization and population equations of motion (atomic response) are considered up to different orders of Liouville pathways. Thus, we can employ perturbation theory to calculate the density-matrix elements. In this five-level system as shown in Fig. 4, the perturbation chains are written as following,

$$\mathrm{I}: \rho_{00}^{(0)} \xrightarrow{\omega_1} \rho_{10}^{(1)} \xrightarrow{\omega_2} \rho_{20}^{(2)} \xrightarrow{-\omega_2} \rho_{10}^{(3)}$$
$$\mathrm{II}: \rho_{00}^{(0)} \xrightarrow{\omega_1} \rho_{10}^{(1)} \xrightarrow{\omega_2} \rho_{20}^{(2)} \xrightarrow{-\omega_3} \rho_{30}^{(3)} \xrightarrow{\omega_3} \rho_{20}^{(4)} \xrightarrow{-\omega_2} \rho_{10}^{(5)}$$
$$\mathrm{III}: \rho_{00}^{(0)} \xrightarrow{\omega_1} \rho_{10}^{(1)} \xrightarrow{\omega_2} \rho_{20}^{(2)} \xrightarrow{-\omega_3} \rho_{30}^{(3)} \xrightarrow{\omega_4} \rho_{40}^{(4)} \xrightarrow{-\omega_4} \rho_{30}^{(5)} \xrightarrow{\omega_3} \rho_{20}^{(6)} \xrightarrow{-\omega_2} \rho_{10}^{(7)}$$

Here, to proceed further, and to simplify the mathematics, we will neglect the ground-state depletion ($\rho_{00}^{(0)} \approx 1$) and not consider the propagation characteristics of the pulsed pump, probe and FWM fields. Also, we only retain the resonant dipole interaction terms in the derivation of the complex susceptibility, known as the rotating-wave approximation (RWA). Because of the selectivity imposed by the RWA, each pulse interaction contributes in a unique way to the phase matching direction of the nonlinear signal. Chains (I)-(III) correspond to the FWM, SWM and EWM processes, respectively. Finally, we obtain

$$\rho_{10}^{(3)} = \frac{-iG_1G_2(G_2^{'})^* \mathrm{e}^{i\boldsymbol{k}_\mathrm{F}\cdot\boldsymbol{r}}}{(\Gamma_{10}+i\Delta_1)^2[\Gamma_{20}+i(\Delta_1+\Delta_2)]} \tag{6}$$
$$\rho_{10}^{(5)} = \frac{iG_1G_2(G_2^{'})^*G_3(G_3)^* \mathrm{e}^{i\boldsymbol{k}_\mathrm{S}\cdot\boldsymbol{r}}}{(\Gamma_{10}+i\Delta_1)^2[\Gamma_{20}+i(\Delta_1+\Delta_2)]^2[\Gamma_{30}+i(\Delta_1+\Delta_2-\Delta_3)]} \tag{7}$$
$$\rho_{10}^{(7)} = \frac{-iG_1G_2(G_2^{'})^*G_3(G_3)^*G_4(G_4)^* \mathrm{e}^{i\boldsymbol{k}_\mathrm{E}\cdot\boldsymbol{r}}}{(\Gamma_{10}+i\Delta_1)^2[\Gamma_{20}+i(\Delta_1+\Delta_2)]^2[\Gamma_{30}+i(\Delta_1+\Delta_2-\Delta_3)]^2[\Gamma_{40}+i(\Delta_1+\Delta_2-\Delta_3+\Delta_4)]} \tag{8}$$

where, $\boldsymbol{k}_\mathrm{F} = \boldsymbol{k}_1+\boldsymbol{k}_2-\boldsymbol{k}_2^{'}$, $\boldsymbol{k}_\mathrm{S} = \boldsymbol{k}_1+\boldsymbol{k}_2-\boldsymbol{k}_2^{'}+\boldsymbol{k}_3-\boldsymbol{k}_3^{'}$, $\boldsymbol{k}_\mathrm{E} = \boldsymbol{k}_1+\boldsymbol{k}_2-\boldsymbol{k}_2^{'}+\boldsymbol{k}_3-\boldsymbol{k}_3^{'}+\boldsymbol{k}_4-\boldsymbol{k}_4^{'}$.

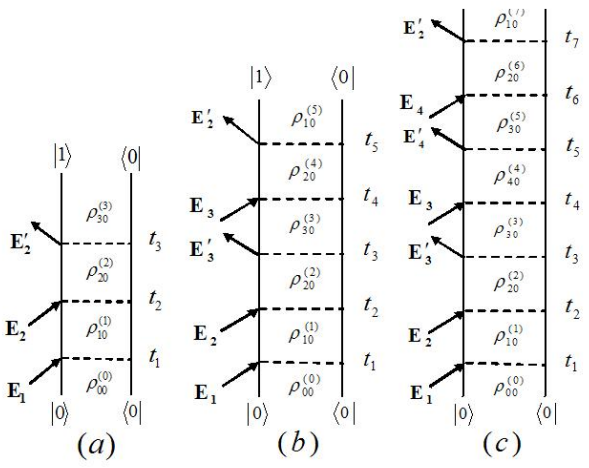

FIG. 5. Double-sided Feynman diagrams. (a), (b) and (c) represent FWM, SWM and EWM processes, respectively

The response functions ($\rho_{10}^{(3)}$, $\rho_{10}^{(5)}$, $\rho_{10}^{(7)}$) of the perturbation chains (I)-(III) are given by using double-sided Feynman diagrams (DSFD) as shown in Fig. 5. The time evolutions of the density-matrix elements of the optically driven atoms or molecules can be represented schematically by either the Liouville space coupling representation [chains (I)-(III)], or the DSFD (Fig. 5). Each diagram represents a distinct Liouville space pathway. We show the diagrammatic representations corresponding to the three, five, and seven orders of the resonant dipole interactions applied to the atomic system with five electronic states. In the Liouville space coupling representation. the state of the system is designated by a position in Liouville space, with indices corresponding to the ket-bra "axis". Up and down transitions on the ket are excited by positive and negative frequency fields, whereas negative and positive frequency fields induce up and down transitions on the bra. The DSFD can be described as follows: the vertical left and right lines of the diagram represent the time evolution (bottom to top) of the ket and bra, respectively; the applied electric fields are indicated with arrows oriented toward the left if propagating with a negative wave vector and toward the right for a positive wave vector. Each interaction with the electric field produces a transition between the two electronic states of either the bra or the ket. The ability to track the evolution of the bra and ket simultaneously makes the density matrix representation a most appropriate tool for the description of many

dynamical phenomena in nonlinear optical processes.

D. Singly-Dressed FWM

MWM process can be effectively controlled by the external laser fields, in which the external fields can give considerable perturbation to the atomic levels, namely, the dressing effect, which will be introduced in the following in detail.

As shown in Fig. 6 (a), in the presence of a strong dressing field G_2 (Rabi frequency of $\boldsymbol{E}_2$, and $G_2 = \mu E_2/\hbar$), the dressed states $|+\rangle$ or $|-\rangle$ can be generated with the separation $\Delta_\pm = 2|G_2|$. When scanning the frequency detuning of the dressing field Δ_2, we can obtain EIT for the probe field and a suppressed FWM signal (Fig. 6 (b)), or electromagnetically induced absorption (EIA) for the probe field and an enhanced FWM (Fig. 6 (c)). For the probe field propagating through the medium we define the baseline versus Δ_2 to be the probe field intensity without dressing effect. Thus, this baseline is just the Doppler-broadened absorption signal of the material. With G_2 beam on, we can obtain one EIT peak at $\Delta_1 + \Delta_2 = 0$ where the transmitted intensity is the largest comparing to the baseline. Since there is no energy level in the original position of $|1\rangle$ and the probe field is no longer absorbed by the material, the degree of transmission (or suppression of absorption) of the probe field is the highest. An EIA dip is obtained at $\Delta_1 + \Delta_2 = |G_2|^2/\Delta_1$, where the transmitted intensity is the smallest compared to the baseline. The reason is that the dressed state $|+\rangle$ or $|-\rangle$ is resonant with the probe field which is absorbed by the material and the degree of transmission (or enhancement of absorption) of the probe field is the lowest. Moreover, since the transparent degree (or suppression of absorption) of the probe field G_1 is the largest at $\Delta_1 = 0$, the EIT peaks for G_2 are the highest. While at certain detuning $|\Delta_1|$, the induced transparent degree decreases and the EIT peak reduces. When $|\Delta_1|$ becomes much larger, the degree of transparency decreases and the suppression of absorption changes to enhance absorption.

Such dressing effect can influence the MWM in this way: when the probe field is resonating with the dressed state $|+\rangle$ or $|-\rangle$, i.e., in the case of EIA, the MWM will be enhanced; when the probe and dressing fileds satisfy the two-photon resonance, the MWM will be suppressed. Such influence leads to the AT splitting, suppression and enhancement of MWM.

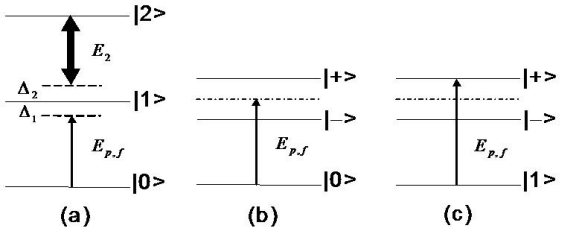

FIG. 6. (a) Diagram of three-level ladder-type system with a dressing field $\boldsymbol{E}_2$ (and detuning Δ_2). The dressed-state pictures of the (b) suppression (or EIT) and (c) enhancement (or EIA) of FWM $\boldsymbol{E}_\mathrm{f}$ (or probe field $\boldsymbol{E}_\mathrm{p}$ with detuning Δ_1) for the two-level system, respectively

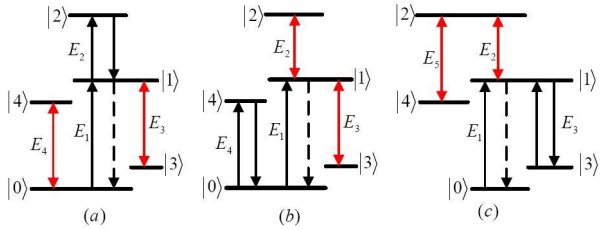

FIG. 7. (a) Parallel-cascade, (b) sequential-cascade, and (c) nested-cascade mode doubly-dressed FWMs

E. Doubly-Dressed FWM

Next, we introduce doubly-dressed effect on the generation process of FWM or probe transmission signal. It is generally divided into parallel-, nested-, and sequential-cascade modes. First in the parallel-type doubly-dressed case, as shown in Fig. 7 (a), the fields $\boldsymbol{E}_3$ and $\boldsymbol{E}_4$ dress different levels $|1\rangle$ and $|0\rangle$, via the subchains $\rho_{10} \xrightarrow{-\omega_3} \rho_{30} \xrightarrow{\omega_3} \rho_{10}(\rho_{(G_3\pm)0})$ and $\rho_{20} \xrightarrow{-\omega_4} \rho_{24} \xrightarrow{\omega_4} \rho_{20}(\rho_{2(G_4\pm)})$, respectively. This means that the dressing effects of $\boldsymbol{E}_3$ and $\boldsymbol{E}_4$ lay parallels. In parallel-cascade case, the profiles (dashed curves in Fig. 8(a)) are induced by one dressing field, and the transition between bright and dark states (in Fig. 8(a)) is caused by the other dressing field. So, the two dressing fields in parallel-dressed cascade mode have no interaction. And there is only one symmetric center at $\Delta_1 = 0$.

In Fig. 7 (b), the FWM signal is in sequential-cascade doubly-dressed mode (dressed by $\boldsymbol{E}_2$ and $\boldsymbol{E}_3$), in which the fields $\boldsymbol{E}_2$ and $\boldsymbol{E}_3$ dress the same level $|1\rangle$ via the subchain $\rho_{10} \xrightarrow{\omega_2} \rho_{20} \xrightarrow{-\omega_2} \rho_{10} \xrightarrow{-\omega_3} \rho_{30} \xrightarrow{\omega_3} \rho_{10}$. This means that the dressing effects of $\boldsymbol{E}_2$ ($\rho_{10} \xrightarrow{\omega_2} \rho_{20} \xrightarrow{-\omega_2} \rho_{10}$) and $\boldsymbol{E}_3$ ($\rho_{10} \xrightarrow{-\omega_3} \rho_{30} \xrightarrow{\omega_3} \rho_{10}$) join together sequentially, therefore, we call this type of dressing mode as sequential-cascade mode. The profiles of the FWM (i.e., AT-splitting) and probe transmission (i.e., EIT) (the dashed curves in Fig. 8 (b)) show a double-peak and double-dip structure ver-

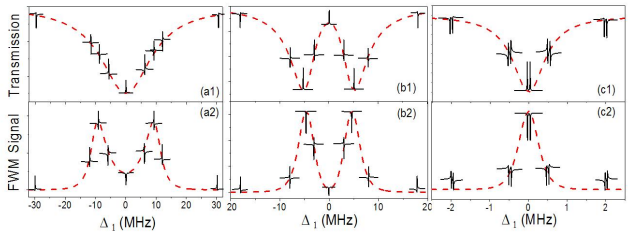

FIG. 8. (a1), (b1) and (c1) Parallel, sequential and nested-cascade doubly-dressed probe transmission signals, respectively. (a2), (b2) and (c2) the corresponding FWM signals. The dashed curves in (a), (b) and (c) are the probe transmission ((a1)-(c1)) and the corresponding pure FWM signals ((a2)-(c2)) without $\boldsymbol{E}_3$ or $\boldsymbol{E}_5$, respectively

sus Δ_1 with $\boldsymbol{E}_2$ blocked. The transition between bright and dark states (in Fig. 8 (b)) is caused by $\boldsymbol{E}_2$. Both of the two signals in Fig. 8 (b) show three symmetric centers which reflect the interaction between two dressing fields. In the comparison between sequential and parallel-cascade modes, the transition between the bright and dark states reveals interaction between the two dressing fields in the former mode, while no interaction is revealed in the latter mode.

In Fig. 7 (c), the FWM signal is in nested doubly-dressed mode (inner-dressing field $\boldsymbol{E}_2$ and outer-dressing field $\boldsymbol{E}_5$), in which $\boldsymbol{E}_5$ dresses the same level $|1\rangle$ after $\boldsymbol{E}_2$ having dressed it. This means the dressing effect of $\boldsymbol{E}_5$ ($\rho_{20} \xrightarrow{-\omega_5} \rho_{40} \xrightarrow{\omega_5} \rho_{20}$) is nested in that of $\boldsymbol{E}_2$ ($\rho_{10} \xrightarrow{\omega_2} \rho_{20}$ and $\rho_{20} \xrightarrow{-\omega_2} \rho_{10}$). By scanning the detuning of inner-dressing field $\boldsymbol{E}_2$, the dashed curves in Fig. 8 (c) show one AT splitting structure in the pure FWM signal and one EIT window in probe transmission signal. In such case, there is only one symmetric center when inner dressing field is scanned, but three symmetric centers when outer-dressing field is scanned, which reflects the strong interaction between two dressing fields. Compare the nested-cascade modes with the sequential-cascade dressing modes, the interaction between two dressing fields in the former case is stronger, which is reflected as dual-bright-state and dual-dark-state in the evolution of FWM signal and probe transmission.

III. COHERENT CONTROL OF MWM VIA EIT

A. Enhanced MWM Process

There are three basic configurations for three-level atomic systems, i.e. ladder-type, V-type, and Λ-type systems, as shown in Fig. 9. A strong coupling (pump) laser beam (with frequency ω_2 and Rabi frequency G_2) drives the atomic transition between state $|2\rangle$

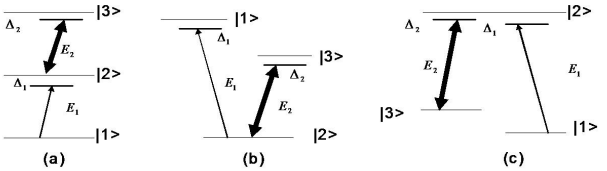

FIG. 9. Sketches of (a) the three-level ladder-type atomic system; (b) the three-level Λ-type atomic system; and (c) the three-level V-type atomic system. Δ_1 and G_1 (Δ_2 and G_2) are the frequency detuning and the Rabi frequency of the probe (the coupling) field, respectively.

and state $|3\rangle$, and a weak probe laser (frequency ω_1 and Rabi frequency G_1) drives the transition between state $|1\rangle$ and $|2\rangle$. The strong coupling beam dramatically modifies the probe transmission properties. For a given coupling beam strength, a transparency window is created for the probe beam near the two-photon resonance condition $\Delta_1 + \Delta_2 = 0$ (with a dip in χ''), where Δ_1 and Δ_2 are the frequency detunings of the probe and coupling beams, respectively. A sharp normal dispersion slope is created at the center of the EIT window, which can be used to slow down the group velocity of the probe light pulses. Both of the absorption reduction and dispersion enhancement are important in increasing the efficiencies of nonlinear optical processes. The slowing down of the optical pulses inside the medium increases the effective interaction length, and the opened EIT window will allow the generated signal beam to propagate through the medium with greatly reduced absorption.

For atoms inside a vapor cell, the Doppler effect can dramatic affect the atomic coherence and EIT-related effects. Actually, Doppler-broadening at room temperature can wipe out most of the coherence effects unless the coupling laser power is extremely large (which needs to use pulsed lasers). However, by using two-photon Doppler-free configurations, first-order Doppler effect can be eliminated; such EIT and related effects can be observed with cw diode lasers near atomic resonance. To achieve the two-photon Doppler-free configuration, the coupling and the probe lasers have to counter-propagate through the atomic vapors for the three-level ladder-type system and copropagate through the atomic vapors for Λ and V-type systems.

B. Coexistence and Interaction between High-Order Nonlinear Processes

1. Opening FWM and SWM channels via Dual EIT windows

To understand the approach of simultaneously generating different nonlinear wave mixing processes, we

will take the generate of highly efficient coexistence FWM and SWM as an example. This section is based on Ref. [10], which will offer more details for the readers. Several features in this work are distinctly different from and have advantageous over the previously reported SWM processes. First, FWM and SWM processes can be observed simultaneously in this open-cycled Y-type system, which is not the case in the close-cycled N-type system. Such coexistence of FWM and SWM processes allows us to investigate the interplay between the two interesting nonlinear optical effects, and to obtain the beat signal between them to get the $\chi^{(5)}$ coefficient. Second, the generated FWM and SWM signals fall into two separate EIT windows in this four-level dual-EIT system, so the linear absorptions for the generated FWM and SWM signals are both greatly suppressed. By individually controlling (or tuning) the EIT windows, the generated FWM and SWM signals can be clearly separated and distinguished or pull together (by frequency detuning) to observe interferences between them. Third, since the amplitude of the FWM signal can be controlled (enhanced or suppressed) by the coupling beam (via dressed states), the relative strengths of the FWM and SWM can be adjusted easily. So, the SWM signal can be made to be in the same order as the FWM signal. Fourth, multi-photon destructive interference effects for both FWM (three-photon interference) and SWM (five-photon interference) are clearly observed in the experiment. Although double- and triple-resonance EIT spectroscopies have been reported previously by detecting fluorescence, the current method is a coherent phenomenon. Finally, by designing the propagation directions of the (pump, coupling and probe) laser beams, we can achieve Doppler-free configurations for all the EIT subsystems in this Y-type atomic system. This makes the FWM and SWM processes very efficient even with relatively weak cw laser beams in an atomic vapor cell.

The pump and coupling laser beams are aligned spatially in the pattern as shown in Fig. 10 (a), with four pump and coupling beams ($\boldsymbol{E}_2$, $\boldsymbol{E}_2^{'}$, $\boldsymbol{E}_3$, $\boldsymbol{E}_3^{'}$) propagating through the atomic medium in the same direction with small angles ($\sim 0.3^{\circ}$) between them in a square-box pattern (the angles are exaggerated in the figure). During our experiment, one of the pump beams ($\boldsymbol{E}_2^{'}$) is always blocked so we will only consider the system shown in Fig. 10 (c). The probe beam ($\boldsymbol{E}_1$) propagates in the opposite direction with an angle as shown in Fig. 10 (a). Since the angles between the propagation directions are very small, this configuration satisfies the two-photon Doppler-free conditions for the two ladder-type EIT subsystems. For simplicity, we will only consider the diffracted FWM and SWM signals relevant to our experimental measurements. By setting the propagation direction of the probe beam $\boldsymbol{E}_1$ as indicated in Fig. 10 (a) and blocking $\boldsymbol{E}_2^{'}$, the diffracted FWM ($\boldsymbol{E}_{\rm f}$) and SWM ($\boldsymbol{E}_{\rm s}$) signal beams will be in the same direction determined by the phase-matching conditions: $\boldsymbol{k}_{\rm f} = \boldsymbol{k}_1 + \boldsymbol{k}_3 - \boldsymbol{k}_3^{'}$ and $\boldsymbol{k}_{\rm s} = \boldsymbol{k}_1 + \boldsymbol{k}_2 - \boldsymbol{k}_2 + \boldsymbol{k}_3 - \boldsymbol{k}_3^{'}$, respectively. The total FWM process can be considered as a result of the constructive or destructive interference between the two dressed FWM channels ($\rho_{00}^{(0)} \xrightarrow{\omega_1} \rho_{\pm 0}^{(1)} \xrightarrow{\omega_3} \rho_{30}^{(2)} \xrightarrow{-\omega_3} \rho_{\pm 0}^{(3)}$), where $|+\rangle$ and $|-\rangle$ are the two dressed states for level $|1\rangle$ due to $\boldsymbol{E}_2$ coupling. We can write down the two SWM processes (indicated in Figs. 10 (e) and (f)) as: (II) $\rho_{00}^{(0)} \xrightarrow{\omega_1} \rho_{10}^{(1)} \xrightarrow{\omega_2} \rho_{20}^{(2)} \xrightarrow{-\omega_2} \rho_{10}^{(3)} \xrightarrow{\omega_3} \rho_{30}^{(4)} \xrightarrow{-\omega_3} \rho_{10}^{(5)}$ and (III) $\rho_{00}^{(0)} \xrightarrow{\omega_1} \rho_{10}^{(1)} \xrightarrow{\omega_3} \rho_{30}^{(2)} \xrightarrow{-\omega_3} \rho_{10}^{(3)} \xrightarrow{\omega_2} \rho_{20}^{(4)} \xrightarrow{-\omega_2} \rho_{10}^{(5)}$, respectively. Of course, if $\boldsymbol{E}_3^{'}$ is blocked instead of $\boldsymbol{E}_2^{'}$ (Fig. 10 (d)), same results can be obtained just with the indices 2 and 3 switched.

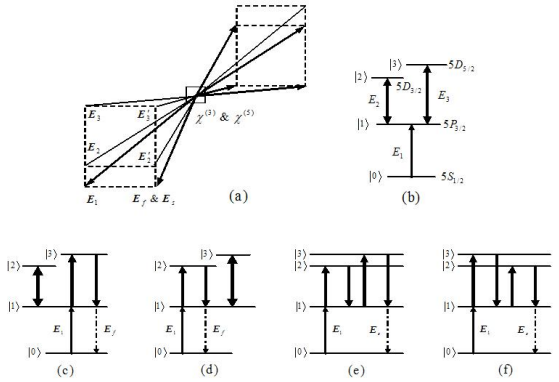

FIG. 10. (a) Spatial beam geometry used in the experiment. (b) Simple Y-type atomic system with dual ladder-type EIT; (c) and (d) FWM processes with two pump beams in one upper transition dressed by a strong coupling beam in another upper transition; (e) and (f) SWM processes with two pump beams in one upper transition and two photons from the coupling beam from another upper transition. $\boldsymbol{E}_{\rm f}$ and $\boldsymbol{E}_{\rm s}$ (dash-dotted lines) are the generated FWM and SWM signals, respectively. The bold double heading arrows imply the strong coupling beam

In general, for arbitrary field strengths of $\boldsymbol{E}_2$, $\boldsymbol{E}_3$, and $\boldsymbol{E}_3^{'}$, one needs to solve eleven coupled density-matrix equations to obtain $\rho_{10}^{(3)}$ for the FWM process and $\rho_{10}^{(5)}$ for the SWM process. In order to see the relation and interplay between the FWM and SWM processes, we calculate these nonlinear susceptibilities via appropriate perturbation chains for simplicity. When both $\boldsymbol{E}_2$ and $\boldsymbol{E}_2^{'}$ are blocked, the simple FWM via chain (I) gives $\rho_{10}^{(3)} = -iG_a {\rm e}^{i\boldsymbol{k}_{\rm f}\cdot\boldsymbol{r}}/(d_1^2 d_3)$, where $G_a = G_1 G_3 (G_3^{'})^*$, $d_1 = \Gamma_{10} + i\Delta_1$, $d_3 = \Gamma_{30} + i(\Delta_1 + \Delta_3)$ with $\Delta_i = \Omega_i - \omega_i$ and Γ_{ij} is transverse relaxation rate between states $|i\rangle$ and $|j\rangle$. Next, when the coupling

field $\boldsymbol{E}_2$ is turned on, the above simple FWM process will be dressed and a perturbative approach for such interaction can be described by the following coupled equations:

$$\partial\rho_{10}^{(1)}/\partial t = -d_1\rho_{10}^{(1)} + iG_1 e^{i\boldsymbol{k}_1\cdot\boldsymbol{r}}\rho_{00}^{(0)} + iG_2^* e^{-i\boldsymbol{k}_2\cdot\boldsymbol{r}}\rho_{20}$$
$$\text{and } \partial\rho_{20}/\partial t = -d_2\rho_{20} + iG_2 e^{i\boldsymbol{k}_2\cdot\boldsymbol{r}}\rho_{10}^{(1)} \quad (9)$$

$$\partial\rho_{10}^{(3)}/\partial t = -d_1\rho_{10}^{(3)} + iG_2^* e^{i\boldsymbol{k}_2\cdot\boldsymbol{r}}\rho_{20} + iG_3^{'*} e^{-i\boldsymbol{k}_3\cdot\boldsymbol{r}}\rho_{30}$$
$$\text{and } \partial\rho_{20}/\partial t = -d_2\rho_{20} + iG_2 e^{i\boldsymbol{k}_2\cdot\boldsymbol{r}}\rho_{10}^{(3)} \quad (10)$$

where $d_2 = \Gamma_{20} + i(\Delta_1 + \Delta_2)$. Equations (9) and (10) ($\rho_{00}^{(0)} \approx 1$) can be solved together with chain (I) to give $\rho_{10}^{'} = -2iG_a e^{i\boldsymbol{k}_f\cdot\boldsymbol{r}} d_2/[d_1 d_3(d_1 d_2 + |G_2|^2)]$.

Expression $\rho_{10}^{'}$ shows an interesting interplay between the FWM and SWM processes. With coupling field $\boldsymbol{E}_2$ on, the energy level $|1\rangle$ is dressed to split into two levels $|+\rangle$ and $|-\rangle$ with induced coherence between them. The FWM signals will have quantum interference via the two intermediate levels $|+\rangle$ and $|-\rangle$, which can either enhance or suppress the total observed FWM signal. When the coupling field $\boldsymbol{E}_2$ is very strong ($\boldsymbol{E}_2 >> \boldsymbol{E}_3(\boldsymbol{E}_3^{'}) >> \boldsymbol{E}_1$), there exists a maximum suppression of the FWM at the exact multiple-EIT of condition $\Delta_1 = -\Delta_2 = -\Delta_3$. Also, one can easily calculate the susceptibility $\rho_{10}^{(5)}$ for SWM from pathways (II) and (III) (as shown in Figs. 10 (e) and (f)) directly to be $\rho_{10}^{(5)} = \rho_{10}^{(\mathrm{II})} + \rho_{10}^{(\mathrm{III})} = 2iG_a|G_2|^2 e^{i\boldsymbol{k}_s\cdot\boldsymbol{r}}/(d_1^3 d_2 d_3)$. Since $\rho_{10}^{(3)}$ and $\rho_{10}^{(5)}$ have opposite signs, multi-dimensional solitons and light condensates can be considered in this system with competitive and giant $\chi^{(3)}$ and $\chi^{(5)}$.

The two EIT windows are generated by the double-ladder EIT subsystems in the Y-type four-level system with both pump fields (between $|1\rangle$ and $|3\rangle$) and coupling field (between $|1\rangle$ and $|2\rangle$) stronger than the probe beam (between $|0\rangle$ and $|1\rangle$), as shown in Fig. 10 (c). Since the generated SWM signal falls into one ladder-type EIT window ($|0\rangle - |1\rangle - |2\rangle$ branch), the SWM processes can be very efficient, especially when the FWM signal is suppressed. For finite frequency detunings Δ_2 and Δ_3, the two EIT windows in the Y-type system will be separated, and the generated FWM and SWM signals in these two EIT windows are easily distinguishable. Specifically, it is easy to see that there exist dual ladder-type EIT windows for $\boldsymbol{E}_1$, $\boldsymbol{E}_f$, as well as the SWM signal ($\boldsymbol{E}_s$). There are one three-photon interference pathway (i.e., interference between $\omega_1 + \omega_3 - \omega_3$ and ω_1) for the FWM process and two five-photon interference pathways (i.e., between five-photon $\omega_1 + \omega_2 - \omega_2 + \omega_3 - \omega_3$ and ω_1, and between five-photon $\omega_1 + \omega_3 - \omega_3 + \omega_2 - \omega_2$ and ω_1) for the SWM processes. In this system, the three-photon and five-photon interferences are destructive that $\chi^{(3)}$ and $\chi^{(5)}$ are zeros at the line centers. Coexisting SWM and FWM signal efficiencies and amount of suppression of the FWM signal are most prominent under the multiple EIT condition of $\Delta_1 = -\Delta_2 = -\Delta_3$ and $\boldsymbol{E}_2 >> \boldsymbol{E}_3(\boldsymbol{E}_3^{'}) >> \boldsymbol{E}_1$ in Fig. 10 (c) (and $\boldsymbol{E}_3 >> \boldsymbol{E}_2(\boldsymbol{E}_2^{'}) >> \boldsymbol{E}_1$ in Fig. 10 (d)).

The experimental demonstrations of co-existing FWM and SWM processes, as well as controllable FWM and SWM processes, were carried out in atomic vapor of ^{87}Rb. The energy levels of $5s_{1/2}$ ($F = 2$), $5p_{3/2}$, $5d_{3/2}$, and $5d_{5/2}$ form the four-level Y-type system as shown in Fig. 10 (b). The laser beams were carefully aligned as indicated in Fig. 10 (a) (without $\boldsymbol{E}_2^{'}$). The vapor cell temperature is set to be 60°C. The probe laser beam $\boldsymbol{E}_1$ (with a wavelength of 780 nm, from an external cavity diode laser (ECDL), connecting $\boldsymbol{E}_f$ $5s_{1/2} - 5p_{3/2}$, and vertical polarization) is horizontally polarized and has a power of about $P_1 \approx 3.5$ mW. The pump laser beams $\boldsymbol{E}_3$ and $\boldsymbol{E}_3^{'}$ (wavelength 775.98 nm, connecting transition $\boldsymbol{E}_f$ $5p_{3/2} - 5d_{5/2}$, and vertical polarization) are split from a CW Ti: Sapphire laser with equal power ($P_3 \approx P_3^{'}$). The coupling laser beam $\boldsymbol{E}_2$ (with power P_2, wavelength 776.16 nm, and connecting $5p_{3/2} - 5d_{3/2}$) is from another ECDL and is vertically polarized. Great cares were taken in aligning the laser beams with spatial overlaps and wave vector phase-matching conditions with small angles ($\sim 0.3°$) between them, as indicated in Fig. 10 (a). The diameters at the vapor cell center for the pump and coupling beams are about 0.5 mm, and the diameter of the probe beam ($\boldsymbol{E}_1$) is about 0.3 mm. The diffracted FWM and SWM signals ($\boldsymbol{k}_f$ and $\boldsymbol{k}_s$ satisfying phase matching conditions) with horizontal polarization are in the direction of $\boldsymbol{E}_f$ & $\boldsymbol{E}_s$ (at the lower right corner of Fig. 10 (a)) and are detected by an avalanche photodiode detector (APD). The transmitted probe beam is simultaneously detected by a silicon photodiode.

The dual-EIT windows of the Y-type system are measured by setting $\Delta_2 = -112$ MHz and $\Delta_3 = 0$, with three laser beams ($\boldsymbol{E}_2$, $\boldsymbol{E}_3$ and $\boldsymbol{E}_3^{'}$) on. These two modified EIT windows from the two ladder-type EIT subsystems (at standard $\Delta_1 = -\Delta_2$ and $\Delta_1 = -\Delta_3$ EIT positions in probe transmission trace detected at the silicon photodiode) are depicted in Fig. 11 (peaks 4 and 5 of curve (b)). Meanwhile, as Δ_1 is scanned, several generated wave-mixing signals are observed (curve (a) of Fig. 11). We identify peak 2 as a combination of the FWM signal and a small amount of SWM signal. Peak 3 is the SWM signal and peak 1 is another FWM signal outside the EIT windows.

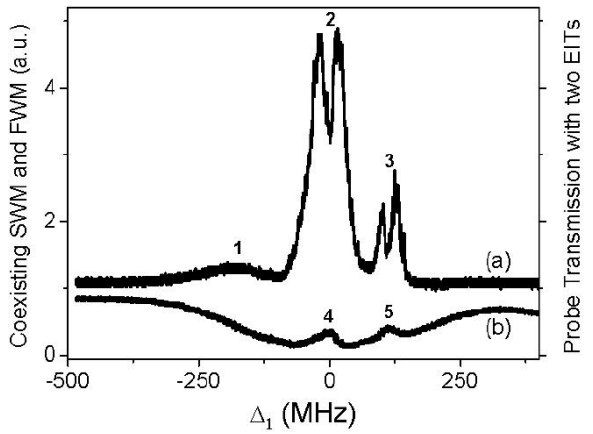

FIG. 11. (a) Measured SWM (peak 3) and FWM (peaks 1 and 2) signals. (b) Probe beam transmission (peaks 4 and 5: two ladder-type EIT windows) versus Δ_1. The experimental parameters are P_1 =3.6 mW, $P_2^{'}$ =0, P_2 =33 mW, $P_3 = P_3^{'}$ =130 mW, $\Delta_2 = -112$ MHz, and $\Delta_3 = 0$[10]

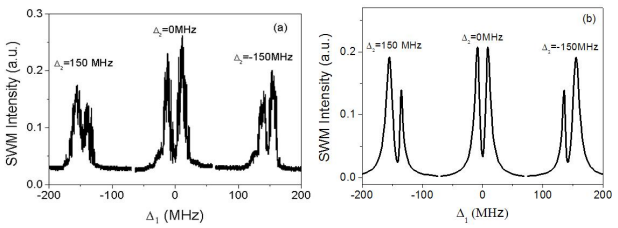

FIG. 12. (a) Measured SWM signal spectra for different coupling field $\boldsymbol{E}_2$ frequencies; (b) Theoretical plot of SWM intensity versus Δ_1 for different Δ_2 values. P_1 =3.4 mW, $P_2^{'}$ =0, P_2 =34 mW, $P_3 = P_3^{'}$ =96 mW, $\Gamma_{10}/2\pi$ =3 MHz, $\Gamma_{20} = \Gamma_{30} = 2\pi \times 0.5$ MHz, and $\Delta_3 = -450$ MHz[10]

Since the FWM and SWM signals are diffracted in the same spatial direction, we identify them by selectively blocking different laser beams and detuning different laser frequencies. We intentionally set large frequency detuning to separate the generated FWM and SWM signals in Fig. 11 for clarity. When the difference between Δ_2 and Δ_3 is reduced, the two EIT windows start to merge and the FWM and SWM signals begin to interfere. The dip in the middle of the FWM signal (peak 2 of curve (a) in Fig. 11) is due to three-photon destructive interference, which is clearly observed in this coherent signal detection.

Figure 12 presents the changes of the SWM signal (corresponding to the peak 3 in Fig. 11) as a function of the coupling field frequency detuning. It is seen from Fig. 12 (a) that, as Δ_2 changes, the generated SWM signal changes from symmetric to asymmetric, which is due to two-photon or three-photon resonant emission enhancement. Such asymmetric SWM spectra have been simulated by numerically solving the eleven coupled density-matrix equations for the system at the steady state and are displayed in Fig. 12 (b). The dips at the line center of the SWM spectra are due to five-photon (one probe photon plus four pump and coupling photons) destructive interference with the generated signal photon, which looks like a multi-photon EIT phenomenon, but is actually a suppression of generating SWM due to multi-photon destructive interference at the exact resonance.

The maximal FWM and SWM efficiencies in this system are quite high (measured to be about 10% and 1%, respectively). The coexistence of these two nonlinear wave-mixing processes in this system can be used to evaluate the high-order nonlinear susceptibility $\chi^{(5)}$ by beating the FWM and SWM signals. Since $|\rho_{10}^{(3)}| >> |\rho_{10}^{(5)}|$ is generally true, the real and imaginary parts of $\chi^{(5)}$ can be measured by homodyne detection with the FWM signal as the strong local oscillator. We have also measured the FWM and SWM signals when all the four strong laser beams ($\boldsymbol{E}_2$, $\boldsymbol{E}_2^{'}$, $\boldsymbol{E}_3$, $\boldsymbol{E}_3^{'}$) are present. This four-level atomic system with co-existing FWM and SWM is consisted of three conventional two-photon Doppler-free EIT subsystems, i.e., $|0\rangle - |1\rangle - |2\rangle$ (ladder-type), $|0\rangle - |1\rangle - |3\rangle$ (ladder-type) and $|2\rangle - |1\rangle - |3\rangle$ (V-type). In general, we can investigate interesting interplays between two fundamental nonlinear wave-mixing processes, and identify ways to enhance the higher-order nonlinear optical processes through opening new nonlinear channels via atomic coherence and quantum interference.

2. Temporal and Spatial Interference between FWM and SWM

In the section III. B. 1, the dual-EIT windows are used to transmit the generated FWM and SWM signals, therefore highly efficient FWM and SWM can be simultaneously generated. If the generated FWM and SWM are transmitted in the same EIT window, spatial-temporal coherent interference between FWM and SWM will occur.

Since the angles between the laser beams in the square-box pattern are very small (0.3°), the optical alignments of the laser beams are quite tedious and challenging. In the generated FWM and SWM signal beams, the coherence lengths are given by $l_{\rm F} = 2c/[n(\omega_2/\omega_1)|\omega_2 - \omega_1|\theta^2]$ and $l_{\rm S} = 2c/[n(\omega_3/\omega_1)|\omega_3 - \omega_1|\theta^2]$, respectively, with n being the refractive index at the frequency ω_1. In the experiment, θ is very small (0.3°) that $l_{\rm F}$ and $l_{\rm S}$ are much larger than the interaction length L, so the phase-mismatch effect can be neglected.

With the current condition (G_3, $G_3^{'}$)> G_2 >>($G_2^{'}$, G_1), and neglecting other MWM processes that are either very weak or propagate in other directions, the total detected intensity at angle θ is given by the co-

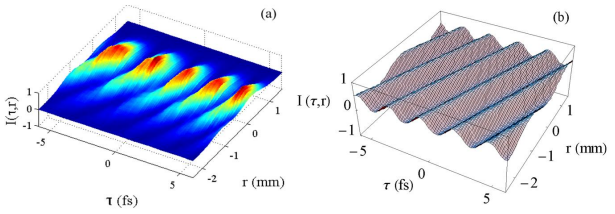

FIG. 13. (a) A three-dimensional spatial-temporal interferogram of the FWM and SWM signal intensity $I(\tau, r)$ versus time-delay τ and transverse position r. (b) The theoretically simulated result from Eq. (11). The signal intensity is normalized to 1. The parameters are Ω_2 =2.427 fs^{-1}, Δk=1. 9 mm^{-1}, and η =1.5

existing FWM ($\boldsymbol{E}_{\rm F}$) and SWM ($\boldsymbol{E}_{\rm S}$) signal as

$$I(\tau, r) \propto |\chi^{(3)}|^2+|\eta\chi^{(5)}|^2+2\eta|\chi^{(3)}||\chi^{(5)}|\cos(\varphi_3-\varphi_5+\varphi) \quad (11)$$

where $\eta = \varepsilon_2\varepsilon_3\varepsilon_3^{'}/\varepsilon_2^{'}$, $\chi^{(3)} = -i\mu_1^2\mu_2^2N/\{\varepsilon_0\hbar^3 d_1 d_2[d_1 + (G_3 + G_3^{'})^2/d_3]\} = |\chi^{(3)}|\exp(i\varphi_3)$, $\chi^{(5)} = 2i\mu_1^2\mu_2^2\mu_3^2N/(\varepsilon_0\hbar^5 d_1^3 d_2 d_3) = |\chi^{(5)}|\exp(\imath\varphi_5)$, $d_3 = \Gamma_{30} + i(\Delta_1 - \Delta_3)$ with $\varphi = \Delta\boldsymbol{k}\cdot\boldsymbol{r}-\omega_2\tau$ and $\Delta\boldsymbol{k} = \boldsymbol{k}_{\rm F}-\boldsymbol{k}_{\rm S} = (\boldsymbol{k}_2-\boldsymbol{k}_2^{'})-(\boldsymbol{k}_3-\boldsymbol{k}_3^{'})$. μ_1, μ_2 and μ_3 are the dipole moments of the transitions $|0\rangle - |1\rangle$, $|1\rangle - |2\rangle$ and $|3\rangle - |1\rangle$, respectively, and ε_2, ε_2, ε_3, ε_3 are the respective amplitudes of the fields.

From Eq. (11), it is clear to see that the total signal has not only spatial interference with a period of $2\pi/\Delta k$, but also an ultrafast time oscillation with a period of $2\pi/\omega_2$, which form a spatial temporal interferogram. With a plane-wave approximation and the square-box configuration for the laser beams with small angles, the spatial interference occurs in the plane perpendicular to the propagation direction.

Figure 13 depicts a typical three-dimensional interferogram pattern (Fig. 13 (a)). Figure 13 (b) presents a theoretical simulation for the total intensity with appropriate parameters. The temporal oscillation period is $2\pi/\omega_2$=2.588 fs, which corresponds to the transition from $5P_{3/2}$ to $5D_{5/2}$ with a frequency of Ω_2=2.427 fs^{-1} in ^{85}Rb. Such measurement of atomic transition frequency in optical wavelength range is Doppler-free and can be used as a tool for precision frequency measurement. If this technique is used on a transition with larger energy difference, sub-femtosecond time resolution can be achieved by scanning translation stage in nanometer precision. The spatial interference is determined by the value of $\Delta k \approx 2\pi|\lambda_2 - \lambda_3|\theta/\lambda_2\lambda_3$. In our experimental situation, we have $2\pi/\Delta k$=3.3 mm along the direction of $\Delta\boldsymbol{k}$, which gives a little more than one interference fringe. When the phase delay is varied with $\boldsymbol{E}_2^{'}$ beam, the spatial interference pattern can be changed from destructive to constructive at the center of the beam profile ($r = 0$).

To see how well the transition frequency Ω_2 can be determined from such time interference fringe, we need to consider two cases. When the laser linewidths are much narrower than the homogeneous linewidths of the transitions, the phase fluctuations of the laser fields will limit the range of the time delay, which puts an upper boundry on the accuracy of the modulation frequency measurement. In such case, the accuracy of measuring modulation frequency is determined by the laser linewidths. This measurement depends on how well ω_2 can be tuned to the transition frequency Ω_2, and is Doppler-free, which can be useful in optical spectroscopy and precision measurements. For the other case, when the laser bandwidths are larger than the atomic decay rates, the modulation frequency corresponds directly to the resonant frequency Ω_2. The accuracy in the modulation frequency measurement will then be determined by the homogeneous linewidths of the atomic transitions, even in the Doppler broadened atomic medium, which is applicable to transitions between metastable states.

A few points are worth mentioning here. First, our experimental results indicate that we can not only enhanced SWM to be in the same order of intensity as the co-existing FWM signal, but also manipulate their spatial and temporal behaviors by controlling the phase delay in one of the laser beams. Such spatial-temporal interferogram between FWM and SWM signals was generated with three independent laser sources. Second, by adjusting the power of $\boldsymbol{E}_2^{'}$ beam, the relative strengths of the FWM and SWM signals can be easily adjusted. In the case of making $\boldsymbol{E}_{\rm S} << \boldsymbol{E}_{\rm F}$ (letting $\boldsymbol{E}_2^{'} \rightarrow \boldsymbol{E}_2$ in power), Eq. (11) can serve as a heterodyne detection method to determine the ratio of high-order nonlinear susceptibilities ($\chi^{(5)}/\chi^{(3)}$). Since $\chi^{(3)}$ can be easily measured, the $\chi^{(5)}$ coefficient in such atomic medium can then be determined. Third, the technique used here can be easily transferred to solid materials, on which EIT and FWM processes can be easily obtained. Fourth, with controlled FWM and SWM processes and enhanced efficiency via atomic coherence and the opened EIT window, three-photon entanglement or correlated triplet photons can be generated for testing fundamental quantum mechanics and quantum information processing.

3. Efficient Energy Transfer between FWM and SWM

The interaction between FWM and SWM is not only reflected by the spatial-temporal coherent interference, but also the energy transfer between them as well. As well know, by manipulating the atomic coherence and quantum interference between different energy levels in the multi-level atomic system with

carefully-designed phase-matching conditions and intensities, as well as setting the optical depth of the atomic medium at certain value, we can generate and control co-existing FWM and SWM processes, and their relative strengths. Spatial-temporal coherent interference between FWM and SWM was discussed in the section III. B. 2, and energy transfer between the FWM and SWM signals during their propagation occurred. In this section, we study how the FWM and SWM signal fields reach their steady-state values during propagation and the coupled equations for the probe, FWM, and SWM fields are used to explain the measured results. Studying such energy exchange during propagation between high-order nonlinear wave-mixing processes can help us to understand and control these higher-order nonlinear optical processes, and hopefully lead to interesting applications in opto-electronic devices, 2D soliton formation, generations of entangled photons, and quantum information processing.

In the generated FWM and SWM signal beams, the coherence lengths are given by $l_{\rm c}^{\rm f} = 2c/[n(\omega_2/\omega_1)|\omega_2 - \omega_1|\theta^2]$ and $l_{\rm c}^{\rm s} = 2c/\{n[(\omega_2+\omega_3)/\omega_1]|\omega_2+\omega_3-\omega_1|\theta^2\}$, respectively, with n being the refractive index at the frequency ω_1. In our experiment, θ is very small (about 0.3°) that $l_{\rm c}^{\rm f}$ and $l_{\rm c}^{\rm s}$ are much larger than the interaction length L, so the phase-mismatch can be neglected.

Under the conditions $(G_3,\, G_3^{'}) > (G_2, G_2^{'}) >> G_{\rm p}$, a set of coupled equations for the probe field and the generated dominant FWM & SWM fields can be used to describe the dynamics of the system as

$$\partial G_{\rm p}/\partial z = i\xi_{\rm p}\rho_{10}^{\rm p} = -\frac{D_1}{D_l}G_{\rm p} + \frac{D_2}{D_{\rm f}}G_{\rm f}\exp(-i\Delta\boldsymbol{k}_{\rm f}\cdot\boldsymbol{r}) - \frac{D_3}{D_{\rm s}}G_{\rm s}\exp(-i\boldsymbol{k}_{\rm s}\cdot\boldsymbol{r}) \tag{12-1}$$

$$\partial G_{\rm f}/\partial z = i\xi_{\rm f}\rho_{10}^{\rm f} = -\frac{D_4}{D_l}G_{\rm f} + \frac{D_5}{D_{\rm f}}G_{\rm p}\exp(i\Delta\boldsymbol{k}_{\rm f}\cdot\boldsymbol{r}) + \frac{D_6}{D_{\rm f}}G_{\rm s}\exp(i\Delta\boldsymbol{k}_{\rm s}\cdot\boldsymbol{r}) \tag{12-2}$$

$$\partial G_{\rm s}/\partial z = i\xi_{\rm s}\rho_{10}^{\rm s} = -\frac{D_7}{D_l}G_{\rm s} - \frac{D_8}{D_{\rm s}}G_{\rm p}\exp(i\Delta\boldsymbol{k}_{\rm f}\cdot\boldsymbol{r}) - \frac{D_8}{D_{\rm s}}G_{\rm f}\exp(i\Delta\boldsymbol{k}_{\rm s}\cdot\boldsymbol{r}) \tag{12-3}$$

where $\xi_{\rm p(f,s)} \equiv 2k_{\rm p(f,s)}\mu^2 N/\hbar$, $\Delta\boldsymbol{k}_{\rm f} = \boldsymbol{k}_1 - \boldsymbol{k}_{\rm f}$, $\Delta\boldsymbol{k}_{\rm s} = \boldsymbol{k}_1 - \boldsymbol{k}_{\rm s}$. When the laser beams are on resonances, $D_1 = \xi_{\rm p}\Gamma_{20}\Gamma_{30}$, $D_2 = \xi_p\Gamma_{30}G_2^2$, $D_3 = \xi_{\rm p}G_2^2G_3^2$, $D_4 = k_{\rm f}D_1/k_{\rm p}$, $D_5 = k_{\rm f}D_2/k_{\rm p}$, $D_6 = k_{\rm f}G_3^2D_2/(G_2^2k_{\rm p})$, $D_7 = k_{\rm s}D_1/k_{\rm p}$, $D_8 = k_{\rm s}G_3^2D_2/(\Gamma_{30}k_{\rm p})$, $D_l = \Gamma_{10}\Gamma_{20}\Gamma_{30} + \Gamma_{30}G_2^2 + \Gamma_{20}G_3^2$, $D_{\rm f} = \Gamma_{10}\Gamma_{20}(\Gamma_{10}\Gamma_{30} + G_3^2)$, and $D_{\rm s} = \Gamma_{10}^3\Gamma_{20}\Gamma_{30}$. N , and μ are the atomic density, decoherence rates, and the dipole moment of the relevant transition, respectively.

Equations (12-1)∼(12-3) are derived from the optical responses of the medium to the probe, the generated FWM and SWM fields, respectively. The first terms in these equations contain the linear susceptibilities with the EIT signature, and the second and third terms in each equation are contributions from the third- and fifth-order nonlinear susceptibilities, respectively, which are the parametric conversion processes. More explicitly, the linear susceptibilities control the dispersion profiles and transmission spectra of the probe and the generated FWM and SWM fields, while the third- and fifth-order nonlinearities play the essential roles in determining the features of energy transfer between FWM and SWM processes.

These coupled equations indicate that not only the probe beam can generate FWM and SWM fields, but also these FWM and SWM fields can affect each other. Competitions between these fields are the key to establish the equilibrium among them. The solutions of these coupled equations determine the propagation characteristics of the generated $\boldsymbol{E}_{\rm f}$ and $\boldsymbol{E}_{\rm s}$ fields. To see the physical picture more clearly without giving the complicated solutions, we rewrite Eqs. (12-2) and (12-3) as

$$\frac{\partial(G_{\rm f}+G_{\rm s})}{\partial z} = -\frac{D_4}{D_l}(G_{\rm f}+G_{\rm s}) + (\frac{D_5}{D_{\rm f}} - \frac{D_8}{D_{\rm s}})G_{\rm p} + (\frac{D_6}{D_{\rm f}}G_{\rm s} - \frac{D_8}{D_{\rm s}}G_{\rm f}) \tag{13}$$

By examining the solutions at large propagation distance (which give $D_1 \approx D_4 \approx D_7$, $D_1 \approx D_4 \approx D_7$ and $D_3 \approx D_8$), we notice that some balance conditions are satisfied, i.e., $D_2D_{\rm f}/D_{\rm f} - D_3D_{\rm s}/D_{\rm s} = 0$ in Eq. (12-1) for the probe beam, and $D_6D_{\rm s}/D_{\rm f} - D_8D_{\rm f}/D_{\rm s} = 0$ in Eq. (13) for the FWM + SWM signals. Quantum destructive interferences between three-photon ($G_{\rm f}$) and five-photon ($G_{\rm s}$) excitation pathways are the underlying mechanisms for the probe and the generated FWM + SWM signals to reach equilibrium.

For given initial conditions of $G_{\rm p}(z=0) = Q_0$, $G_{\rm f}(z=0) = G_{\rm s}(z=0) = 0$ at the entrance face

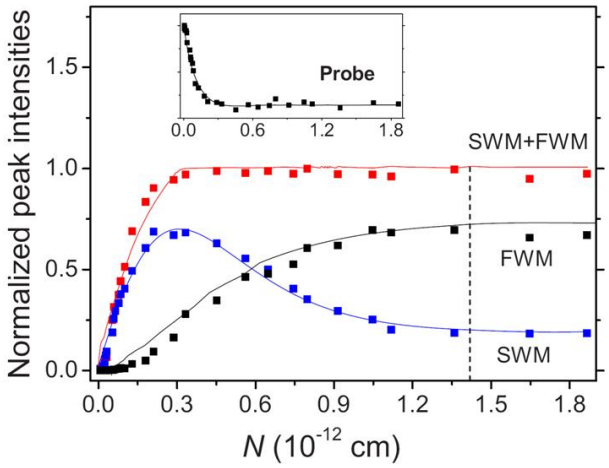

FIG. 14. Square points: Measured FWM and SWM peak intensities versus atom number density (FWM curve, SWM curve, and FWM+SWM curve). Inset: The measured probe intensity at the EIT window. Solid lines: Theoretically calculated curves corresponding to the measured results (square points). The parameters are $G_1 = 2\pi \times 5$ MHz, $G_2 = G_2^{'} = 2\pi \times 35$ MHz, $G_3 = G_3^{'} = 2\pi \times 80$ MHz, $\Delta_3 = 0 - \Delta_1 = \Delta_2 = 312$ MHz, $\Gamma_{10}/2\pi = 3$ MHz, $\Gamma_{20}/2\pi = 0.4$ MHz, and $\Gamma_{30}/2\pi = 2$ MHz

of the medium, Eqs. (12-1) and (12-2) can be solved analytically to be

$$G_{\rm f}+G_{\rm s} = \frac{Q_0 D_1}{D_1 - D_4}\left(\frac{D_8}{D_{\rm s}} - \frac{D_5}{D_{\rm f}}\right)\left[1-\exp\left(1-\frac{D_4 z}{D_l}\right)\right] \quad (14)$$

where $D_4 z/D_l \propto Nz$. From Eq. (14), it is clear to see that for sufficiently large Nz with $4\exp(-D_4 z/D_l) << 1$, the solution reaches a constant value independent on z. These balancing conditions indicate that after an initial propagation distance for the FWM and SWM signals to build up (while the probe intensity decreases accordingly), the probe beam and the total generated FWM + SWM beams reach their equilibrium. After that the FWM and SWM fields will only transfer energies between themselves and, eventually, after a much longer propagation distance, reach their individual steady states, so they will propagate in the medium without further absorption and distortion.

Figure 14 (square points) shows the intensities of the probe, FWM, and SWM signals as a function of atomic density, respectively. The FWM and SWM signals increase initially at low atomic density (or equivalently short propagation distance), as the probe beam intensity decreases. At certain atomic density (about $N = 0.3 \times 10^{12}/\text{cm}^3$), the probe and the FWM + SWM intensities reach their equilibriums, after which energy exchange occurs only between the FWM and SWM signals as they propagate through the medium. Eventually, at a higher atomic density (about $N = 1.2 \times 10^{12}/\text{cm}^3$), the FWM and SWM signals reach their respective steady-state values individually. This is the first observation of energy exchange between the generated FWM and SWM signals in propagation and the process of reaching their steady-state values. The theoretically simulated results from Eq. (12) are plotted in Fig. 14 (solid lines), which match quite well with the measured data.

Such energy exchange during propagation can be influenced by many parameters. For example, the intensities of $\boldsymbol{E}_3$ and $\boldsymbol{E}_3^{'}$ can greatly modify the balance between the FWM and SWM generating processes. By fixing the atomic cell temperature to have $N = 1.4 \times 10^{12}/\text{cm}^3$ (dashed line in Fig. 14), the relative FWM and SWM intensities can be tuned by varying the power of $\boldsymbol{E}_3$ ($\boldsymbol{E}_3^{'}$).

There are a few important issues that are worth raising here. First, if a pulsed laser is used for the probe beam, the generated FWM and SWM signals will be slowed down due to sharp dispersion, and eventually become pulse-matched with the probe pulses, as in the case of FWM. Such system could possibly used to generate entangled FWM (or SWM) photon pairs and even triplet photons for quantum information processing. Second, both FWM and SWM processes described here share the same $\boldsymbol{E}_{\rm p}$, $\boldsymbol{E}_2$ and $\boldsymbol{E}_2^{'}$ beams, so strong competitions between these wave-mixing processes, as well as the three-photon and five-photon interferences, exist in this system. The energy exchange and interactions between the generated FWM and SWM during propagation are the manifestation of strong coupling and competitions between these high-order nonlinear optical processes. Third, in order to investigate the FWM and SWM energy exchange, we selectively suppressed the typically efficient SWM channels in the $\boldsymbol{k}_{\rm m}$ direction (by using lower $\boldsymbol{E}_2$ & $\boldsymbol{E}_2^{'}$ powers and slightly misaligning the $\boldsymbol{E}_3$ & $\boldsymbol{E}_3^{'}$ beams), so only dominant FWM process needs to be considered in this direction.

In summary, FWM and SWM processes were shown to co-exist in the inverted-Y atomic system. The efficient coupling between these high-order nonlinear wave-mixing processes makes them exchange energy in propagation before reaching their respective equilibrium values at long propagation distance (or high optical density) through the medium. Quantum destructive interferences between three-photon and five–photon excitation pathways for FWM and SWM, respectively, as well as reabsorption via nonlinear processes, are the underlying mechanism for the generated FWM and SWM fields to reach equilibrium. By choosing appropriate propagation length (or atomic cell temperature) or pump power $\boldsymbol{E}_3$ and $\boldsymbol{E}_3^{'}$, one can get desired relative strengths between the FWM and SWM signals from $I_{\rm FWM} < I_{\rm SWM}$ to $I_{\rm FWM} > I_{\rm SWM}$.

A theoretical model has been developed to compare with the experimentally measured FWM and SWM generation processes during propagation with excellent agreements. Understanding and controlling the high-order nonlinear optical processes, such as $\chi^{(3)}$ and $\chi^{(5)}$, can be very important in studying new physical phenomena (such as 2D soliton formation and liquid light condensate) and in designing new applications for quantum information processing (such as entangled photon generations and 3-qubit quantum computation).

C. AT Splitting and Enhancement/ Suppression

1. AT Splitting in High-Order Nonlinear Processes

Atomic AT splitting (ac-Stark splitting) was first observed on a radio-frequency transition, and then in Calcium atoms. Such AT splitting effect was also investigated in lithium molecule using cw triple-resonant spectroscopy and in semiconductor material with ultrashort intense laser pulses. Recently, an antiblockade effect due to the AT-split Rydberg population was studied theoretically and experimentally with two-photon excitation in a three-level atomic system. In this section, firstly, the primary and secondary AT splitting of the dressed FWM process in an EIT window of a four-level Y-type atomic vapor system. Theoretical calculations are carried out to well explain the observed results, giving a full physical understanding of the interesting multiple AT splitting in the high-order nonlinear optical processes. Then, we go further to investigate the complex AT splitting phenomena in the SWM process. Although primary AT splitting in molecular lithium has been reported previously by detecting fluorescence, the current method is a coherent phenomenon in high order nonlinear processes, making use of the unique spatial phase-matching conditions and laser induced atomic coherence in the multi-level atomic system, so it can be used to control the direction of optical signals.

The two ladder-type EIT subsystems form two EIT windows. The two EIT windows can either overlap or be separated by changing the frequency detuning of the pump and coupling laser beams. First, without the strong coupling field $\boldsymbol{E}_3$, a simple FWM process (with $\boldsymbol{E}_1$, $\boldsymbol{E}_2$ and $\boldsymbol{E}_2^{'}$) will generate a signal field $\boldsymbol{E}_{\rm F}$ with frequency ω_1. The density-matrix element $\rho_{10}^{(3)}$ of the FWM signal could be got via the perturbation chain (I) $\rho_{00}^{(0)} \xrightarrow{\omega_1} \rho_{10}^{(1)} \xrightarrow{\omega_2} \rho_{20}^{(2)} \xrightarrow{-\omega_2} \rho_{10}^{(3)}$. When the powers of $\boldsymbol{E}_2$ and $\boldsymbol{E}_2^{'}$ are strong enough, they will start to dress the energy level $|1\rangle$ to create the primarily-dressed states $|+\rangle$ and $|-\rangle$, as shown in Fig. 15 (c), which can be described via the perturbation chain (II)

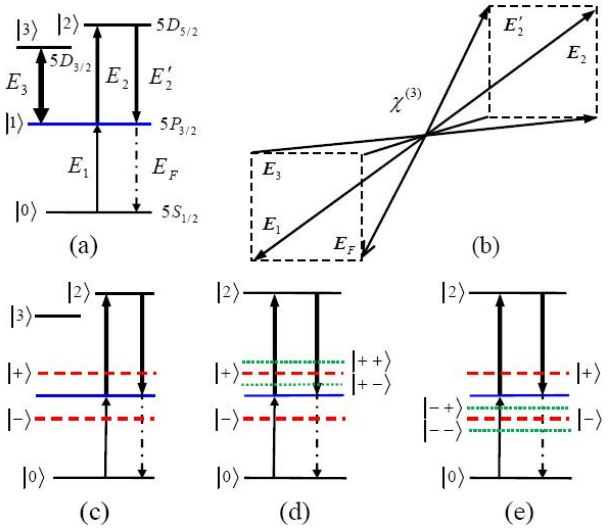

FIG. 15. (a) Four-level Y-type atomic system. (b) Spatial phase-matching beam geometry used in the experiment. (c)∼(e) Corresponding dressed-state pictures of (a)

$\rho_{00}^{(0)} \xrightarrow{\omega_1} \rho_{\pm 0}^{(1)} \xrightarrow{\omega_2} \rho_{20}^{(2)} \xrightarrow{-\omega_2} \rho_{\pm 0}^{(3)}$. Similarly, a stronger probe field $\boldsymbol{E}_1$ can also modify such FWM process. Such self-dressing effect, i.e. the participating FWM fields dress the involved energy level which then affects the FWM process itself, is unique for such MWM processes in multi-level systems and has not been systematically studied before. Next, when the coupling field $\boldsymbol{E}_3$ is added, these fields ($\boldsymbol{E}_2$ ($\boldsymbol{E}_2^{'}$) and $\boldsymbol{E}_3$) can dress the energy level $|1\rangle$ together. $\boldsymbol{E}_2$ ($\boldsymbol{E}_2^{'}$) first creates the primary dressed states $|\pm\rangle$, then $\boldsymbol{E}_3$ creates the secondary dressed states $|\pm\pm\rangle$ at a proper frequency detuning (tuned to near either the upper or lower dressed state $|+\rangle$ or $|-\rangle$), as shown in Figs. 15 (d) and (e), via the perturbation chain (III) $\rho_{00}^{(0)} \xrightarrow{\omega_1} \rho_{\pm\pm 0}^{(1)} \xrightarrow{\omega_2} \rho_{20}^{(2)} \xrightarrow{-\omega_2} \rho_{\pm\pm 0}^{(3)}$, which generates the secondary AT splitting for the FWM signal. The two primary dressed states induced by $\boldsymbol{E}_2$ and $\boldsymbol{E}_2^{'}$ can be written as $|\pm\rangle = \sin\theta_1|1\rangle + \cos\theta_1|2\rangle$ (Fig. 15 (c)). When $\boldsymbol{E}_3$ only couples the dressed state $|+\rangle$, the secondary dressed states are given by $|+\pm\rangle = \sin\theta_2|+\rangle + \cos\theta_2|3\rangle$ (Fig. 15 (d)), where $\sin\theta_1 = -a_1/a_2$, $\cos\theta_1 = G_2^b/a_2$, $\sin\theta_2 = -a_3/a_4$, $\cos\theta_2 = G_3/a_4$, $a_1 = \Delta_2 - \lambda_{\pm}$, $a_2 = \sqrt{a_1^2 + |G_2^b|^2}$, $a_3 = \Delta_3 - \lambda_+ - \lambda_{+\pm}$, $a_4 = \sqrt{a_3^2 + |G_3|^2}$, and $G_2^b = G_2 + G_2^{'}$. The eigenvalues are $\lambda_{\pm} = (\Delta_2 \pm \sqrt{\Delta_2^2 + 4|G_2|^2})/2$ for $|\pm\rangle$, and $\lambda_{+\pm} = (\Delta_3^{'} \pm \sqrt{\Delta_3^{'} + 4|G_3|^2})/2$ for $|+\pm\rangle$, where $\Delta_3^{'} = \Delta_3 - \lambda_+$.

In order to see the AT splitting of the FWM signal in the EIT window, we first calculate these nonlinear susceptibilities via appropriate perturbation chains here for simplicity. When the coupling beam $\boldsymbol{E}_3$ is blocked, the simple FWM (with $\boldsymbol{E}_1$, $\boldsymbol{E}_2$ and $\boldsymbol{E}_2^{'}$)

process via chain (I) gives $\rho_{10}^{(3)} = G_a/(d_1^2 d_2)$, where $G_a = -iG_1G_2(G_2^{'})^* \exp(i\boldsymbol{k}_F \cdot \boldsymbol{r})$. When $\boldsymbol{E}_3$ is turned on, the above simple FWM process will be dressed by fields $\boldsymbol{E}_2$, $\boldsymbol{E}_2^{'}$, $\boldsymbol{E}_3$ and even $\boldsymbol{E}_1$ (if it is not too weak), and the multi-dressed FWM process is

$$\rho_{10}^{(3)} = G_a/[(d_2 + |G_1|^2/d_4)(d_1 + |G_2^b|^2/d_2 + |G_3|^2/d_3)(d_1 + |G_1|^2/\Gamma_0 + |G_3|^2/d_3)] \quad (15)$$

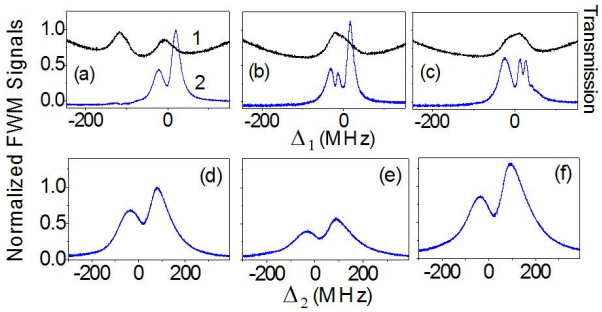

FIG. 16. Measured multi-peak FWM signals (lower curves) and the corresponding EIT (upper curves) induced by the fields $\boldsymbol{E}_2 + \boldsymbol{E}_2^{'}$ and $\boldsymbol{E}_3$ versus Δ_1 for $\Delta_2 = 0$, $\Delta_3 = 125$ (a), $\Delta_3 = 20$ (b), $\Delta_3 = -20$ MHz (c), and versus Δ_2 for $\Delta_1 = -20$, $\Delta_3 = 125$ (d), $\Delta_3 = 20$ (e), $\Delta_3 = -20$ MHz (f). The other parameters are $P_1 = 1.3$ mW, $P_2 = P_2^{'} = 16$ mW and $P_3 = 146$ mW[68]

with $d_4 = \Gamma_{21} + i\Delta_2$. Since the probe field is weak ($G_1 << G_2^b$), the primary AT separation Δ_a is determined mainly by the fields $\boldsymbol{E}_2$ and $\boldsymbol{E}_2^{'}$ (i.e., $\Delta_a = \lambda_+ - \lambda_- \approx 2G_2^b$ as shown in Fig. 16 (a)). The secondary AT separation Δ_c is caused by the dressing field $\boldsymbol{E}_3$ (i.e., $\Delta_c = \lambda_{++} - \lambda_{+-} = \lambda_{-+} - \lambda_{--} \approx 2G_3$ as shown in Figs. 16 (b) and (c)). From the expansions $\rho_{10}^{(3)} \approx G_a[1 - |G_2^b|^2/(d_1 d_2)]/(d_1^2 d_2)$ and $\rho_{10}^{(3)} \approx G_a[1 - |G_3|^2/(d_1 d_2)]^2/(d_1^2 d_2)$, one can see that the first and second terms stand for three-photon and five-photon processes, respectively, which show that the AT splitting results from the destructive interference between the three-photon and five-photon processes.

Figures 16(a)∼(c) present the FWM signal intensity versus the probe field detuning Δ_1 for different dressing field detuning $\Delta_3 = \lambda_\pm \approx G_2^b$. The upper-curve in each figure is the probe transmission with two ladder-type EIT windows, and the lower-curve is the FWM signal. In Fig. 16 (a), the right ($|0\rangle - |1\rangle - |2\rangle$ satisfying $\Delta_1 + \Delta_2 = 0$) EIT window is induced by the pump fields $\boldsymbol{E}_2 + \boldsymbol{E}_2^{'}$ and the left ($|0\rangle - |1\rangle - |3\rangle$ satisfying $\Delta_1 + \Delta_3 = 0$) one is induced by the coupling field $\boldsymbol{E}_3$. The right EIT window contains the double-peak FWM signal $\boldsymbol{E}_{\rm F}$, with the two peaks created by $\boldsymbol{E}_2 + \boldsymbol{E}_2^{'}$(i.e., the primary AT splitting). The left and right peaks of the FWM signal correspond to the dressed states $|+\rangle$ and $|-\rangle$, respectively (Fig. 15 (c)). Since the left EIT window is quite far from the right EIT window, the coupling field $\boldsymbol{E}_3$ basically cannot affect the two peaks in the FWM signal (Fig. 16 (a)).

However, when the frequency of $\boldsymbol{E}_3$ is tuned to move the left EIT window into the left FWM peak, secondary AT splitting occurs and the left FWM signal peak splits into two peaks (Fig. 16 (b)). Moreover, the right FWM peak is enhanced simultaneously, since the coupling field $\boldsymbol{E}_3$ dresses the state $|+\rangle$ and separates it into two secondary dressed states $|++\rangle$ and $|+-\rangle$ (satisfying $\Delta_3 = \lambda_+$). The three peaks in the triple-peak FWM signal (Fig. 16 (b)), from left to right, correspond to the secondary dressed states $|++\rangle$ and $|+-\rangle$, and the primary dressed state $|-\rangle$, respectively (Fig. 15 (d)). Similarly, the right FWM peak is separated into two peaks while the left FWM peak is enhanced when the coupling beam is tuned to the $|-\rangle$ state, as shown in Fig. 16 (c). The three peaks, from left to right, correspond to the primary dressed state $|+\rangle$ and the secondary dressed states $|-+\rangle$ and $|--\rangle$ (satisfying $\Delta_3 = \lambda_-$), respectively (Fig. 15 (e)). Figure 16 (d) shows the AT splitting of the FWM signal versus the pump field detuning Δ_2, when the $|0\rangle - |1\rangle - |3\rangle$ EIT window is tuned quite far from the $|0\rangle - |1\rangle - |2\rangle$ EIT window. In this case the primary AT splitting is mainly caused by $\boldsymbol{E}_2 + \boldsymbol{E}_2^{'}$. When the two EIT windows get close and overlap, Figs. 16 (e) and (f) depict the suppressed and enhanced FWM signal intensities versus Δ_2 for different coupling field detuning Δ_3, respectively. Compared with Fig. 16 (d), the FWM signals are suppressed (Fig. 16 (e)) and enhanced (Fig. 16 (f)) at $\Delta_1 + \Delta_3 = 0$ and $\Delta_1 + \Delta_3 = |G_3|^2/\Delta_1$, respectively. Such FWM signal is enhanced via a single-photon resonance.

With the coupling field $\boldsymbol{E}_3$ blocked and the probe field $\boldsymbol{E}_1$ weak in Fig. 17 (a), the AT splitting separations Δ_a and Δ_b mainly result from the fields $\boldsymbol{E}_2$ and $\boldsymbol{E}_2^{'}$ (i.e. Δ_a, $\Delta_b \approx 2G_2^b$). Such AT splitting separations Δ_a (Fig. 17 (b)) get larger with increasing $\boldsymbol{E}_2$ and $\boldsymbol{E}_2^{'}$. However, when the probe field $\boldsymbol{E}_1$ is strong enough (in Fig. 17 (c)), the AT splitting separations Δ_a and Δ_b are then determined by both the pump fields ($\boldsymbol{E}_2$, $\boldsymbol{E}_2^{'}$) and the probe field $\boldsymbol{E}_1$. As

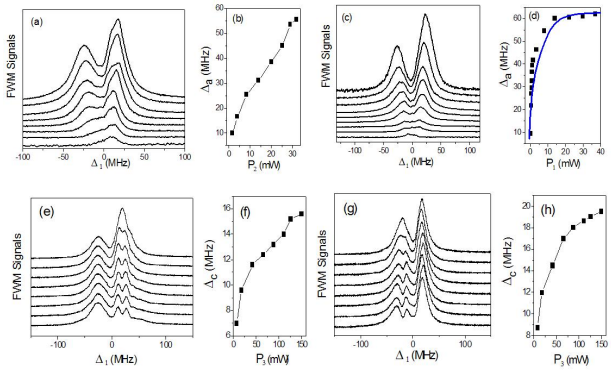

FIG. 17. Measured double-peak FWM signals versus Δ_1 with $\Delta_2 = 0$ for (a) increasing P_2=1.6, 4, 8.3, 14, 20, 25, 29 and 32 mW from bottom to top and (b) the power dependence of $\Delta_a$when P_1=1.3 mW, and for (c) increasing P_1=0.24, 0.48, 0.58, 0.68, 0.83, 0.93, 1.1, 3.4 and 8 mW from bottom to top and (d) the power dependence of Δ_a when P_2=17 mW[68]

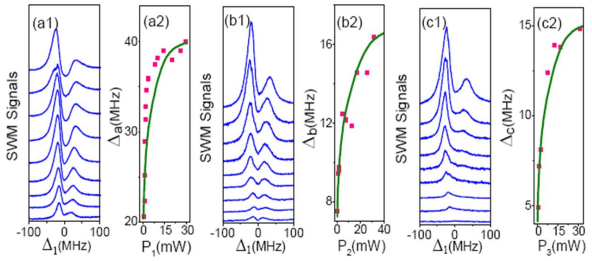

FIG. 18. (a1), (b1) and (c1) are the measured SWM1 self-dressing AT splitting signals versus Δ_1 for $\Delta_2 = -50$ MHz under different P_1, P_2 and P_3 powers, respectively. (a1) is increasing P_1= 0.30, 0.36, 0.43, 0.90, 1.37, 1.85, 2.32, 3.66, 5.33, 8.18, 10.3, 13.61, 15.46, 22.5, 24.2, 25.3, 28.8 and 29.5 mW from bottom to top. (b1) is increasing P_2 =0.3, 0.6, 0.9, 1.2, 1.5, 2.1, 4.5, 7.5, 12.5, 17.2, 25.5 and 31.4 mW from bottom to top. (c1) is increasing P_3= 1.8, 3.9, 6.3, 7.7, 11.4, 16.7, 22.2, 33.1 and 52.2 mW from bottom to top. (a2), (b2) and (c2) are the corresponding power dependences of (a1), (b1) and (c1), respectively. Here Δ_a, Δ_b and Δ_c are the increments of distance between the two A-T splitting peaks when P_1, P_2 and P_3 are increased, respectively, and the squares are the experimental results, while the solid lines in (a2, b2, c2) are the theoretical calculations. The fixed powers in (a1,2), (b1,2) and (c1,2) are (P_2= 32.0 mW & P_3 =55.0 mW), (P_1= 13.0 mW & P_3 =55.0 mW), and (P_1= 13.0 mW & P_2= 32.0 mW), respectively[69]

Δ_a and Δ_b get larger with increasing $\boldsymbol{E}_1$, there exists a turning point at P_1 =10 mW (Fig. 17 (d)), beyond which both AT splitting separations reach their respective saturation values at high probe power (Fig. 17 (d)). Figures 17 (e)∼(h) presents the FWM signal intensity versus the probe field detuning Δ_1 for different frequency detuning Δ_3 and coupling field power P_3. Since the probe $\boldsymbol{E}_1$ is weak, the primary AT splitting Δ_a mainly results from $\boldsymbol{E}_2$ and $\boldsymbol{E}_2^{'}$ (i.e. $\Delta_a = \lambda_+ - \lambda_- \approx 2G_3^b$). The secondary AT splitting Δ_c (i.e., $\Delta_c = \lambda_{++} - \lambda_{+-} \approx 2G_3$ in Fig. 17 (e), $\Delta_c = \lambda_{-+} - \lambda_{--} \approx 2G_3$ in Fig. 17 (g)) gets larger with increasing $\boldsymbol{E}_3$ (Figs. 17 (f) and (h)).

More interestingly, Eq. (15) for the dressed FWM with $G_3 = 0$ can be written as

$$\rho_{10}^{(3)} \approx G_a^{'}[1-|G_1|^2(1/d_2d_4+1/d_1\Gamma_0)+|G_1|^4/(\Gamma_0 d_1 d_2 d_4)] \quad (16)$$

where $G_a^{'} = G_a/\{[1 + |G_2^b|^2/(d_1d_2)]d_1^2d_2\}$. The first term of Eq. (16) represents a three-photon process in the probe and pump fields, the second term is the five-photon process which interferes destructively with the first term and is responsible for the AT splitting in Figs. 17 (d) and (h)) and the third term gives the seven-photon process, which has the same sign as the first term and hence tends to increase the FWM signal. In fact, the second term is dominant at lower probe power, while the third term is dominant at higher probe power. Physically, such saturation behavior in Figs. 17 (d) and (h) is induced by the balanced interactions between the destructive and constructive interferences of these multi-photon transition pathways.

Next, we briefly investigate the self- and externally-dressed AT splitting of the SWM processes within EIT windows in an atomic system. Such AT splitting demonstrates the interactions between two coexisting SWM processes.

For the SWM1 signal (due to the weak probe field), the expression can be simplified as: $\rho_{S1}^{(5)} = iG_{S1}/[(d_1 + G_2^2/d_2)d_2(d_1 + G_2^2/d_2 + G_3^2/d_3)d_3(d_1 + G_3^2/d_3)]$. Similarly, for the SWM2 signal, the expression is simplified as: $\rho_{S2}^{(5)} = iG_{S2}/[(d_1 + G_4^2/d_4)d_4(d_1 + G_3^2/d_3 + G_4^2/d_4)d_3(d_1 + G_3^2/d_3)]$, where $G_{S2} = G_1G_3^{'*}G_3G_4G_4^*$. There exist two ladder-type EIT windows, i.e., the $|0\rangle - |1\rangle - |2\rangle$ EIT1 window satisfying $\Delta_1 + \Delta_2 = 0$ (induced by the coupling field $\boldsymbol{E}_2$) and the $|0\rangle - |1\rangle - |4\rangle$ EIT2 window satisfying $\Delta_1 + \Delta_4 = 0$ (induced by the coupling field $\boldsymbol{E}_4$). The EIT1 and EIT2 windows contain the SWM1 signal ($\boldsymbol{E}_{S1}$) and the SWM2 signal ($\boldsymbol{E}_{S2}$), respectively.

When the external-dressing field $\boldsymbol{E}_4$ is blocked, we get the SWM1 signal within the EIT1 window (which is an inverted-Y system). Figure 18 (a1, b1, c1) presents the SWM1 signal intensity versus the probe field detuning Δ_1 for different field powers of P_1, P_2 and P_3 with the same frequency detuning of $\Delta_2 = -50$ MHz. Obviously, the SWM1 signal shows two peaks due to multi-dressing effects. With the power increases, the intensity of the SWM1 signals increases accordingly, while the left peak height is always greater than the height of the right peak.

Meanwhile, the increments of the AT splitting separations $\Delta_i = \lambda_+^{(1)} - \lambda_-^{(1)} \approx 2\sqrt{|G_j|^2 + |G_{i0}|^2}$ ($i = a, b, c$ corresponds to $j = 1, 2, 3$, respectively, and $|G_{a0}|^2 = |G_{20}^2| + |G_{30}|^2$, $|G_{b0}|^2 = |G_{10}|^2 + |G_{30}|^2$, $|G_{c0}|^2 = |G_{10}|^2 + |G_{20}|^2$), increase obviously with increased powers (Rabi frequencies) P_1 (G_1), P_2 (G_2) and P_3 (G_3), respectively and fixed P_2 & P_3 (G_{20} & G_{30}), P_1 & P_3 (G_{10} & G_{30}) and P_1 & P_2 (G_{10} & G_{20}), respectively. The two peaks of the double-peak SWM1 signal (Figs. 18 (a1), (b1) and (c1)) correspond, from left to right, to the primarily-dressed states $|+\rangle$ and $|-\rangle$, respectively. Moreover, the experimentally measured (peak separation) results in Figs. 18 (a1), (b1) and (c1) are in good agreement with our theoretical calculations (solid curves), as shown in Figs. 18 (a2), (b2) and (c2), respectively.

In summary, we have experimentally observed the AT splitting of high-order nonlinear optical processes in an EIT window in atomic vapor system. The AT splitting can be considered to be due to destructive interference between the three-photon and five-photon processes. Such controlled multi-channel splitting signals in nonlinear optical processes can find potential applications in optical communication and quantum information processing.

2. Enhancement and Suppression of FWM Processes

In the AT splitting, the spectrum of FWM is a combined result of enhancement and suppression due to the dressing effect, and the classical Lorentzian emission line-shape due to the scanning probe detuning. If the detuning of coupling filed is scanned, instead of the probe detuning, the enhancement and suppression due to the dressing effect can be extracted out from the background. Recently, destructive and constructive interferences in a two-level atomic system and competition via atomic coherence in a four-level atomic system with two co-existing FWM processes were studied. In the presence of additional coupling laser fields, more FWM processes can be generated to coexist, which can be selectively suppressed or enhanced via quantum interference. Also, AT splitting in triple-resonance spectroscopy was discussed in section III. C. 1 previously. In this section, we will focus on our experimental studies of enhancement and suppression between two FWM processes. The experimental data clearly show the evolutions of the enhancement and suppression, from pure enhancement to partial enhancement/suppression, and then to pure suppression at resonance, which are in good agreement with theoretically calculated results. There also exist interesting interplays between these two FWM processes due to induced atomic coherence in this system.

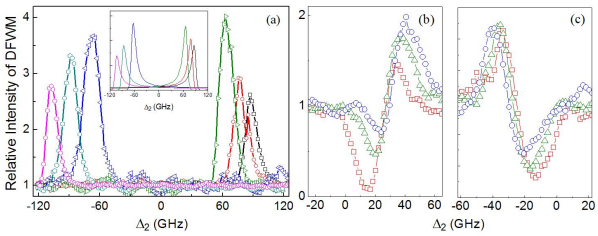

FIG. 19. The evolution of the dressed effects for different Δ_1 values: (a) $\Delta_1 = -101$ GHz (squares), -84.3 GHz (circles), -67 GHz (triangles), 71.3 GHz (reverse triangles), 88.6 GHz (pentagons), 105 GHz (hexagons) from right to left. Inset: theoretical plots corresponding to the experimental parameters. (b) $\Delta_1 = -$ 30.3GHz (Squares), -21.6 GHz (triangles) and -13 GHz (circles). (c) $\Delta_1 =$29.3 GHz (Squares), 38 GHz (triangles) and 42.2 GHz (circles)

We first set Δ_1 at one point and scan Δ_2. Evolution from suppression to enhancement is observed as shown in Fig. 19. The probe field is changed from high to low frequency side. As frequency detuning goes from $\Delta_1 < 0$ to zero, the DFWM signal $\boldsymbol{E}_{\rm f1}$ is enhanced gradually to the maximum value [right side of Fig. 19 (a)], which is an enhanced process. Then, it undergoes a partial enhancement/suppression [Fig. 19 (b)], until the FWM signal is purely suppressed at the resonant point. When Δ_1 changes to be positive, it shows a symmetric process [i.e., a partial suppression/enhancement in Fig. 19 (c), and a pure enhanced process in the left side of Fig. 19 (a)].

One way to explain these observed effects is by using the dressed-state picture. Let us first consider the case of large G_2 (e.g., 15.7 GHz). The dressing field couples the transition $|2\rangle$ to $|1\rangle$ and creates the dressed states $|G_2\pm\rangle$. Therefore, the DFWM signal $\boldsymbol{E}_{\rm f1}$ for a large one-photon detuning is extremely small when $G_2 = 0$, the strong dressing field can cause resonant excitation for one of the dressed states if the condition $\omega_1 + \omega_2 = \omega_{10} + (\omega_{21} \pm \Delta_{G_2})$ (i.e., $\Delta_1 + \Delta_2 \pm \Delta_{G_2} = 0$) is satisfied[14], where Δ_{G_2} is the splitting level relative to the original position of the state $|1\rangle$ by the dressing field $\boldsymbol{E}_2$ or $\boldsymbol{E}_2^{'}$ so that $\Delta_2 = (G_2^2 - \Delta_1^2)/\Delta_1$. For example, the DFWM signal $\boldsymbol{E}_{\rm f1}$ is strongly enhanced in the presence of dressing field when $\Delta_1 = -67$ GHz [Fig. 19 (a)], which is mainly due to the one-photon ($|0\rangle \rightarrow |G_2+\rangle$) resonance. Thus, Δ_1 for $\boldsymbol{E}_{\rm f1}$ is very large initially, so the dressed effect only gives the enhancement. As Δ_1 goes towards zero, the suppression effect gets into play gradually due to the dressed states $|G_2\pm\rangle$. In this case, when the frequency changes from high to low values it results in suppression for the DFWM signal first and then an enhancement. From the data, we can deduce the condition for the suppressed-dip to be $\omega_1 + \omega_2 \equiv \omega_{10} + \omega_{21}$, (i.e. $\Delta_1 + \Delta_2 = 0$). At

the $\Delta_1 = 0$ point (resonant case), only suppression effect exists. For the $\Delta_1 > 0$ part, it has a symmetric evolution between the enhancement and suppression effects, as shown in Fig. 19 (c).

In summary, we report our experimental results with theoretical analysis on the evolutions of the dressed effects of the DFWM and NDFWM processes. The experimental data show that the FWM signal can be enhanced by adding new coupling fields. In addition, we have measured the power dependences of enhanced and suppressed FWM signals. The experimental data are in good agreements with our theoretically calculated results. These studies provide detail physical mechanisms to control and optimize the efficiencies of the MWM processes in multi-level systems.

IV. SPATIALLY COHERENT CONTROL OF MWM VIA PBG

When multiple laser beams interact with multi-level atomic systems, interesting spatial effects for the probe beam, such as pattern formation, spatial displacement, and spatial soliton, can occur and be controlled by stronger coupling or pumping laser beams. In this section, the spatial dispersion properties of the probe and generated signal in FWM process beams will be presented, which can lead to spatial shift and splitting of these weak laser beams. Such beam displacement and splitting can be controlled by the adjustable coupling/pumping laser beams via enhanced cross-Kerr nonlinearity in the multi-level atomic systems near EIT resonance. Because such enhanced spatial dispersion behavior follows closely to the traditional linear and nonlinear dispersion properties in frequency domain for multi-level EIT systems. By controlling the spatial displacements of the weak probe and FWM beams with coupling/pumping beams, spatial optical switching and routing of one beam or multiple optical beams can be achieved.

The dressing fileds in the generation of dressed FWM can interfere with each other, and form spatial periodic dressed state, then periodic refractive index, which leads to the formation of electromagnetically induced grating (EIG) and electromagnetically induced lattice (EIL). Because of the periodic refractive index, EIG has photonic band gap (PBG). When probe beam is incident into the EIG, it will have strong Bragg reflection, and the generated reflection signal is the FWM signal. Therefore, FWM signal carries the modulation of PBG and solitons with periodic spatial profile, such as gap and dipole solitons, can form when the refractive index balances the diffraction. Moreover, if more fields are available in the experiment, a spatial vortex pattern can form and the FWM can be modulated to generate vortex soliton.

The protypes of spatial optical switch, router and multiplexier based on such spatial displacements and splitting of FWM have been investigated. The soliton of FWM has potential application in pattern formation, image storage and processing in optical communication.

A. Enhanced Kerr Nonlinearities

The Kerr effect is a special kind of nonlinear optical phenomenon occurring when intense light beams propagate in crystals, glasses, or gases. Its physical origin is a third-order nonlinear polarization generated in the medium. For self-Kerr nonlinearity, the intense light modifies its own propagation properties, while for the cross-Kerr nonlinearity the propagation properties of a light beam is modified by the interaction with another overlapping beam in a Kerr medium. Actually, the Kerr effect originates from an instantaneously occurring third-order nonlinear response, which can be described as a modification of the refractive index. The refractive index of many optical materials depends on the intensity of the light beam due to the special third-order nonlinear responses, which can be written as $n = n_0 + n_2 I$. Here, n_2 is the Kerr nonlinear index proportional to $\chi^{(3)}$. If higher-order (such as fifth) nonlinearity is considered, the nonlinear index n_2 will be influenced by the intensity of the light beam. With weak CW diode lasers in three-level systems sharp dispersion of n_0 can be induced due to EIT, which can slow down the optical pulse propagation. Also, n_2 of the three-level EIT system has been measured which is greatly enhanced comparing to its two-level subsystem. Since the Kerr nonlinear dispersion in such EIT medium has been shown to have an opposite sign (anomalous dispersion) from the linear dispersion (Fig. 20), and they change dramatically near the EIT resonance, the cavity transmission linewidth with such EIT medium can be greatly modified due to the modified group index $n_{\rm g} = (n_0 + n_2 I_{\rm p}) + \omega_{\mathbf{p}}(\partial n_0/\partial\omega_{\rm p} + I_{\rm p}\partial n_2/\partial\omega_{\rm p})$, where $I_{\rm p}$ is the probe beam intensity and $\omega_{\rm p}$ is the probe laser beam frequency. The linear and nonlinear dispersion terms (the derivatives) dominate in $n_{\rm g}$. Since the two derivatives have opposite signs, $n_{\rm g}$ can take either positive or negative values, depending on the frequency detuning and probe intensity.

The effects of the self- and cross-Kerr nonlinearities also induce phenomena of SPM and XPM which modulate spatial optical beams. Depending on the sign of the nonlinear refractive index, such intensity-dependent refractive index can produce either a converging or diverging wave front to change the transverse beam profile during beam propagation. With SPM a single beam modulates itself during its prop-

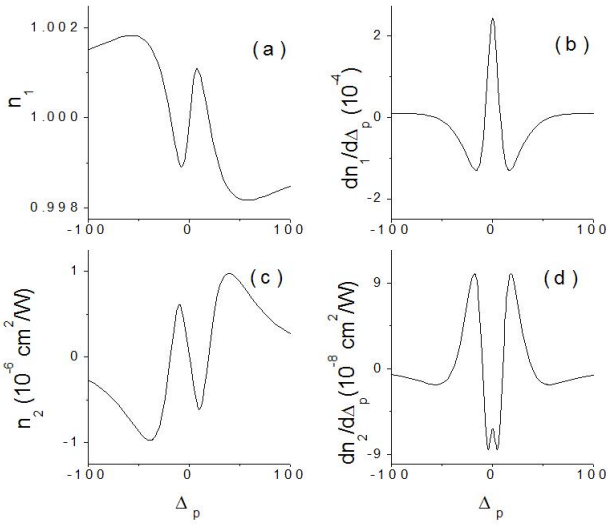

FIG. 20. (a) Linear and (c) nonlinear refractive indices and their derivatives (b) and (d), respectively, as a function of $\Delta_{\rm p}$

agation through medium. When two copropagating or counterpropagating beams modulate each other via nonlinear interaction, it is due to XPM. When $n_2 > 0$, the converging wave front counteracts against diffraction-induced spatial spreading, which can focus the optical beam to demonstrate the self-focused or cross-focused beam when the beam power exceeds a critical value. Similarly, when $n_2 < 0$ the diverging wave front increases the natural diverging this gives the self-defocused or cross-defocused beam. In 1990, Agrawal reported the phenomenon of induced focusing occurring in the self-defocusing nonlinear media as a result of XPM. When a weak optical beam copropagates with an intense pump beam, the XPM induced interaction between the two beams can focus the weak beam, even though the pump beams exhibits self-defocusing. Also, electromagnetically-induced focusing phenomenon was reported in the three-level atomic system. In the three-level EIT system the radial intensity profile of the strong pump laser can generate a modified spatial refractive index profile which is experienced by the weak probe laser as it tunes through the transparency window near resonance. It leads to spatial focusing and defocusing of the probe beam.

Equations (17) $\sim$ (19) are the Maxwell-Bloch equations under rotating-wave and slowly-vary-envelope approximations, which give the mathematical description of the SPM- and XPM-induced spatial interactions among the probe and two FWM beams.

$$\frac{\partial E_{\rm p}}{\partial z}+\frac{\partial E_{\rm p}}{c\partial t}-\frac{i\partial^2 E_{\rm p}}{2\partial t^2}-\frac{i\nabla_\perp^2 E_{\rm p}}{2k_{\rm p}}=\frac{ik_{\rm p}}{n_0}\left[n_1+n_2^{S1}|E_{\rm p}|^2+2n_2^{X1}|E_1^{'}|^2+2n_2^{X2}|E_2^{'}|^2\right]E_{\rm p} \tag{17}$$
$$+\eta_1 E_1(E_1^{'})^* E_{\rm F1}+\eta_2 E_2(E_2^{'})^* E_{\rm F2}$$
$$\frac{\partial E_{\rm F1}}{\partial z}+\frac{\partial E_{\rm F1}}{c\partial t}-\frac{i\partial^2 E_{\rm F1}}{2\partial t^2}-\frac{i\nabla_\perp^2 E_{\rm F1}}{2k_{\rm F1}}=\frac{ik_{\rm F1}}{n_0}\left[n_1+n_2^{S2}|E_{\rm F1}|^2+2n_2^{X3}|E_1^{'}|^2\right]E_{\rm F1} \tag{18}$$
$$+\eta_3 E_1(E_1^{'})^* E_{\rm p}+\eta_4 E_2(E_2^{'})^* E_{\rm F2}$$
$$\frac{\partial E_{\rm F2}}{\partial z}+\frac{\partial E_{\rm F2}}{c\partial t}-\frac{i\partial^2 E_{\rm F2}}{2\partial t^2}-\frac{i\nabla_\perp^2 E_{\rm F2}}{2k_{\rm F2}}=\frac{ik_{\rm F2}}{n_0}\left[n_1+n_2^{S3}|E_{\rm F2}|^2+2n_2^{X4}|E_2^{'}|^2\right]E_{\rm F2} \tag{19}$$
$$+\eta_5 E_1(E_1^{'})^* E_{\rm F1}+\eta_6 E_2(E_2^{'})^* E_{\rm p}$$

Here, on the left side of these equations, the first terms describe the beam propagation, the second terms give the dispersion ones, the third terms are for the second-order dispersion and the fourth terms describe the diffraction of the beams diverging propagation. On the right hand, the first terms are the linear response, the second terms are for the nonlinear self-Kerr effects, the third terms (the third and fourth terms for Eq. (17)) describe the nonlinear cross-Kerr effects, the fourth and fifth terms (the fifth and sixth terms for Eq. (17)) represent the phase-matched coherent FWM processes. z is the longitudinal coordinate in the propagation direction and $k_{\rm p}=k_{\rm F1}=\omega_1 n_0/c$. n_0 and n_1 are the linear refractive index at ω_1 in vacuum and medium, respectively. n_2^{S1} is the self-Kerr nonlinear coefficient of the field $\boldsymbol{E}_3$, n_2^{S2} is the self-Kerr nonlinear coefficient for the generated FWM field $\boldsymbol{E}_{\rm F1}$, and n_2^{S3} is the self-Kerr nonlinear coefficient for the generated FWM field $\boldsymbol{E}_{\rm F2}$. n_2^{X1} is the cross-Kerr nonlinear coefficient of the field $\boldsymbol{E}_3$ induced by the strong pump field $\boldsymbol{E}_1^{'}$, n_2^{X2} is the cross-Kerr nonlinear coefficient of the field $\boldsymbol{E}_3$ induced by the strong pump field $\boldsymbol{E}_2^{'}$, n_2^{X3} is the cross-Kerr nonlinear coefficient of the field $\boldsymbol{E}_{\rm F1}$ induced by the strong

pump field $\boldsymbol{E}_1^{'}$, n_2^{X4} is the cross-Kerr nonlinear coefficient of the field $\boldsymbol{E}_{\rm F2}$ induced by the strong pump field $\boldsymbol{E}_2^{'}$. In general the Kerr nonlinear coefficients can be defined as $n_2 = {\rm Re}\chi^{(3)}/(\varepsilon_0 c n_0)$, where the third-order nonlinear susceptibility is given by $\chi^{(3)} = D\rho_{10}^{(3)}$ with $D = N\mu_{\rm p}^2\mu_{i0}^2/(\hbar^3\varepsilon_0 G_{\rm p} G_i^2)$. $\mu_{\rm p}$ (μ_{i0}) is the dipole matrix element between the states coupled by the probe beam $\boldsymbol{E}_{\rm p}$ (between $|i\rangle$ and $|0\rangle$). η_i are the constants. $\rho_{10}^{(3)}$ can be determined from the density-matrix equations for the multi-level medium.

The strong pump beam distorts the phase profiles of the probe and FWM beams through XPM, which induces the spatial modifications of the probe and FWM beams, including spatial displacement and splitting, and produces spatial solitons. Thus, we can neglect the dispersion, linear term, and coherent FWM processes in the equations for simplicity. Actually, these simplified differential equations are still difficult to solve analytically. By assuming Gaussian profiles for the input fields, we can use a numerical approach (i.e. the split-step Fourier method) to solve Eqs. (17)∼(19). However, numerical solution of 2D equations requires considerable computing resource with both x and y directions. For simplicity, we only consider one dimension in the y-direction. For example, one can consider Eq. (18) and obtain

$$\frac{\partial E_{\rm F1}(z,y)}{\partial z} = \left[\frac{i}{2k_{\rm F1}}\frac{\partial}{\partial y^2} + \frac{ik_{\rm F1}}{n_0}(n_2^{S2}|E_{\rm F1}|^2 + 2n_2^{X3}|E_1^{'}|^2)\right] E_{\rm F1}(z,y) \tag{20}$$

The solution of this equation is approximately $\boldsymbol{E}_{\rm F1}(z+h,y) \approx \exp[ih\hat{D}]\exp[ih\hat{N}]\boldsymbol{E}_{\rm F1}(z,y)$. Here h is the step-length, $\hat{D} = (2k_{\rm F1})^{-1}\partial/\partial y^2$ is the diffraction factor and $\hat{N} = k_{\rm F1}(n_2^{S2}|\boldsymbol{E}_{\rm F1}|^2 + 2n_2^{X3}|\boldsymbol{E}_1^{'}|^2)/n_0$ is the SPM and XPM factor. Finally, we can use the split-step Fourier method to obtain the numerical solution. Furthermore, if we neglect the diffraction term and the small SPM contribution, Eqs. (17)∼(19) can be readily solved to obtain the XPM-induced phase shift ϕ_{NL} imposed on the probe and FWM beams by the pump. In this case, Eq. (20) reduces to

$$\frac{\partial E_{\rm F1}(z,y)}{\partial z} = \left(\frac{i2k_{\rm F1}}{n_0} n_2^{X3}|E_1^{'}|^2\right) E_{\rm F1}(z,y) \tag{21}$$

which gives $\boldsymbol{E}_{\rm F1}(z,y) = \boldsymbol{E}_{\rm F1}(0,y)\exp(i\phi_{NL})$ with $\phi_{NL}(z,y) = 2k_{\rm F1}n_2^{x3}|\boldsymbol{E}_1^{'}|^2 z/n_0$. The additional transverse propagation wave-vector is ${\rm d}k_y = \phi_{NL}^{'}$. Here, the strong field $\boldsymbol{E}^{'}$ has a Gaussian profile, like the solid line in Fig. 21 (a). In this case, when $n_2^{X3} > 0$, ϕ_{NL} has a positive Gaussian profile (see the thick solid line in Fig. 21 (a)) and ${\rm d}k_y$ is shown by the dash line in Fig. 21 (a). The arrows in Fig. 21 (a) represent the direction of ${\rm d}k_y$. The direction of ${\rm d}k_y$ is always towards the beam center of the pump field, and therefore, the weak $\boldsymbol{E}_{\rm p,F1,F2}$ fields (the thin solid lines in Fig. 21 (a)) are shifted to the pump field center. When $n_2^{X3} < 0$, ϕ_{NL} has a negative Gaussian profile (see the thick solid line in Fig. 21 (b)) and the direction of ${\rm d}k_y$ (the dash line in Fig. 21) is outward from the beam center of the pump field, thus $\boldsymbol{E}_{\rm p,F1,F2}$ are shifted away from the pump field (see Fig. 21 (b)).

Recently, spatial displacements of the probe and generated FWM beams have been observed in a three-level V-type, and two-level atomic systems near resonance. The observed spatial shift curves as a function of frequency detuning reflect the typical enhanced cross-Kerr nonlinear dispersion properties in the EIT systems. This dispersion-like spatial deflection is named as EISD. The spatial beam displacements can be controlled by the strong control laser beams and the atomic density. Such EISD can be used as a single way to measure the Kerr-nonlinear refractive indices for the multi-level atomic media. Also, it can be used for controllable all-optical spatial switching and routing of optical signals. The spot shifts of the FWM and probe laser beams can be used as the "on" and "off" states of the spatial all-optical switch. The extinction ratio for the on/off states, as well as the beam shift distances and directions, can be optimized by modulating frequency detuning, intensities, and temperature of the medium. At the same time, beam shifts in opposite directions have been realized simultaneously for different FWM

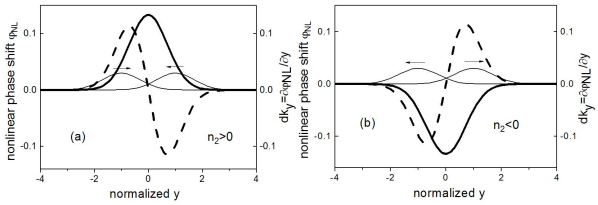

FIG. 21. Instantaneous nonlinear phase shift induced by a Gaussian beam in a (a) focusing and (b) defocusing nonlinear medium and the corresponding contribution to the one-dimensional component of the propagation vector

beams, which could be employed to construct switching/routing arrays. Then, spatial shifts and splitting of FWM signal beams induced by additional dressing laser beams were investigated which are caused by the enhanced cross-Kerr nonlinearity due to atomic coherence in the atomic system. The spatial separation and number of the split FWM beam can both be controlled by the intensity of the dressing beam, and by the modified Kerr nonlinearity and atomic density. Although spatial beam shifting and splitting have been reported previously, the current atomic systems have some advantages: (1) large beam shift and splitting can be achieved due to enhanced Kerr nonlinearity induced by atomic coherence; (2) the "dispersion" curve for the beam displacement has been measured for the probe beam and matched to the calculated cross-Kerr nonlinear index; (3) displacements and splitting of the FWM signal beams are experimentally demonstrated, which have never been done before; (4) specially-designed spatial beam configuration was used to achieve the unique phase-matching conditions for the FWM processes, and for the beam shifting and splitting at the same time; (5) the current multi-level systems have much better experimental controls with additional laser beams; (6) such studies can have important applications in spatial image storage, spatial entanglement, and spatial quantum correlation of laser beams.

A spatial soliton can be formed when the diffraction of a laser beam is compensated by the self-focusing or cross-Kerr effects in a Kerr nonlinear medium. In recent years, many new type spatial solitons, such as discrete solitons, gap solitons, surface gap solitons, and vortex solitons, were investigated (both theoretically and experimentally) in waveguide arrays, fiber Bragg gratings, Bose-Einstein condensates, and photorefractive crystals. In achieving such interesting spatial effects, large refractive index modulations are needed by either fixed periodic structures (such as waveguide arrays and fiber Bragg grating) or reconfigurable optical lattices by laser beams as in the photorefractive crystals. Gap soliton exists in band gaps of the linear spectra in various structures, and the forward and backward propagating waves both experience Bragg scattering and form the periodic structure, which are coupled nonlinearly. A vortex soliton appears as the self-trapping of a phase singularity and from which a screw-type phase distribution is generated with a singularity at the origin where the real and imaginary parts of the field amplitude are zero. Azimuthally modulated vortex solitons (azimuthons) have been theoretically considered in self-focusing nonlinear media. Transverse energy flow occurs between the intensity peaks (solitons) associated with the phase structure, which is a screw nonlinear function described by the factor $\exp(im\varphi)$, where φ is the azimuthal coordinate and the integer number m is defined as the topological charge. If a phase mask is used to introduce certain phase delay for half of the soliton beam, the soliton can split into two parts with opposite (π) phases between them, called dipole-mode vector soliton with a Hermite-Gaussian mode structure. The dipole-mode vector soliton is a vector soliton originated from trapping of a dipole-mode beam. In an optically-induced 2D photonic lattice, dipole-mode solitons can be created with either opposite phases or same phase between the two parts. Vector solitons with one nodeless fundamental component and another dipole-mode component can couple to each other and be trapped jointly in the photonic lattices. A radially symmetric vortex-mode soliton can decay into a radially asymmetric dipole-mode soliton that has a nonzero angular momentum, which can survive for a very long propagation distance. Spatial multi-component soliton has vectorial interaction, mutually self-trapping in a nonlinear medium, and their total intensity profile exhibits multiple humps.

The modulation effect of the vortex solitons is induced by the cross-Kerr nonlinear dispersion due to atomic coherence in the multi-level atomic system. These FWM vortex patterns are explained via the three-, four- and five-wave interference topologies. The complex amplitude vectors can be overlaid at the observation plane and give rise to the total complex amplitude vector (X_X, C_Y) of the interfering plane waves. The local structures of the optical vortices are given by the polarization ellipse relation

$$C_X^2/(T_X^2+T_Y^2)\sin^2(\beta+\alpha) + C_Y^2(T_X^2+T_Y^2)\cos^2(\beta+\alpha)=1 \tag{22}$$

where $\beta = \arctan(T_X/T_Y)$ and α is the ellipse orientation. The ellipse axes T_X, T_Y are related to the spatial configuration of the laser beams (including the incident beam directions, phase differences between beams etc.) and their intensities. Such novel spatial FWM gap soliton trains are induced in periodically modulated self-defocusing atomic medium by the cross-phase modulation, which can be reshaped under different experimental conditions, such as different atomic densities, nonlinear dispersions, and dressing fields. Effects due to the frequency detuning and intensity dependences of the refractive index are considered in addition to its 1D (axis ξ) periodic variation by using $n(\Delta, I, \xi) = n_1(\Delta) + n_2(\Delta)I + \delta n(\xi)$, where I is the dressing field intensity. $\delta n = n_2\cos(2\pi\xi/\Lambda)$ accounts for the periodic index variation inside the grating. The grating period is given by $\Lambda = \lambda/\theta$, where θ is the angle between the two pump beams. The formation and steering of the steady dipole solitons and their dynamical (energy transfer) effects have

been analyzed. The dipole-mode solitons of two FWM processes have horizontal and vertical orientations, respectively, which can coexist in the same atomic system, and their characteristics can be compared directly. In detail, we consider the incoherent superposition of two dipole components, u_2 and u_3, as a generalization of a two-component dipole-model soliton $\{u_1, V\}$. This two-component come from a three-component solution $\{u_1, u_2, u_3\}$. The transformation of the dipole components is $V \rightarrow \{u_2, u_3\}$, where $u_2 = V\cos\alpha$ and $u_3 = V\sin\alpha$ (α is a transformation parameter). Such a straightforward generalization is indeed possible for a N-component system.

As we have demonstrated, the multi-level atomic systems have well-controlled linear, as well as nonlinear, absorption and dispersion properties, which are essential in generating such interesting spatial gap, vortex and multi-component dipole solitons in atomic meida. Without the enhanced Kerr nonlinearities due to atomic coherence, it will be hard to reach the needed index contrast for observing these novel spatial soliton phenomena. With several well-controlled experimental parameters, one can drive the Kerr medium to different parameter regions to investigate richer spatial soliton phenomena (such as formation and dynamics), better explore parametric spaces, and compare with theoretical predictions. Observing such solitons and studying their dynamics in FWM is not a simple extension of the previous results, but a significant breakthrough to explore different nonlinear regions and mechanism for forming such spatial dipole solitons and their evolutions. In solid-state materials, tenable parametric spaces are limited, so certain theoretically predicted phenomena are not reachable in the experiments. However, in the multi-level atomic systems, the tenable regions for parameters are broadened, which can be used to explore interesting phenomena, such as transition from one type of spatial soliton to another and energy transfer between different dipole modes. Also, previous spatial solitons in solid materials were all done in the probe beam, not for FWM beams as in the multi-level atomic media, where Kerr-nonlinear FWM processes are greatly enhanced and become more efficient. The tenable parameters, such as atomic density, coupling/pumping field intensities, and frequency detunings can be easily and independently controlled experimentally, which are important in reaching different regions of the system. Due to the nature of induced atomic coherence in the system, the enhanced Kerr indices change dramatically with experimental parameters and can reach high values. Combining with the use of pulsed laser beams with high beam intensities, the refractive index contrast $\Delta n = n_2 I$ in the multi-level atomic system reaches high value, so those interesting novel solitons can be observed. Also, since the high Kerr index is induced by the strong dressing/pumping laser beams, it is the cross-Kerr nonlinearity that plays essential role in controlling these novel solitons, not the self-Kerr coefficients as in the cases for photon-refractive materials. The basic behaviors and mechanics are different between the multi-level atomic systems and photorefractive crystals in observing these novel solitons. Such controllable spatial dispersion properties and spatial solitons can find useful applications in designing new devices for spatial all-optical switching and logic gate for optical communications and all-optical signal processing.

B. Photonic Band Gap

1. Periodic Energy Level

In experiment, two pump beams with the same frequency are often used, and act as dressing fields if the powers are strong sufficiently as shown in Fig. 22 between them. In the spatial interaction region, $\boldsymbol{E}_2$ and $\boldsymbol{E}_2^{'}$ will interfere with each other and create a periodic intensity distribution, which leads to periodic Rabi frequency amplitude $|G_{2t}(x)|^2 = G_{20}^2 + G_{20}^{'2} + 2G_{20}G_{20}^{'}\cos[2(k_2\sin\theta_1)x]$. Therefore, the dressing effect changes periodically. Influenced by $|G_{2t}(x)|^2$, the naked state $|1\rangle$ will be splitter into two dressing states denoted as $|G_{2t}(x)+\rangle$ and $|G_{2t}(x)-\rangle$, as shown in Fig. 22 (a), locating in the two sides of $|1\rangle$, with their eigen-frequencies offset from that of $|1\rangle$ determined by the pump detuning Δ_2 and Rabi frequency amplitude $G_{2t}(x)$ as $\lambda_{G_t(x)\pm} = \Delta_2/2 \pm \sqrt{\Delta_2^2/4 + |G_{2t}(x)|^2}$. Moreover, we notice that the split energy levels $|G_{2t}(x)+\rangle$ and $|G_{2t}(x)-\rangle$ are periodic along x direction because of the periodic Rabi frequency amplitude $|G_{2t}(x)|^2$.

The doubly dressed mode with the dressing fields $\boldsymbol{E}_3$, $\boldsymbol{E}_3^{'}$, $\boldsymbol{E}_2$ and $\boldsymbol{E}_2^{'}$, shown in Fig. 22, also can lead to the spatial 2D dressed energy states. First, the interference between the dressing fields $\boldsymbol{E}_3$ and $\boldsymbol{E}_3^{'}$ leads to periodic dressing effect, and therefore split the naked state into two dressing states denoted as $|G_{3t}(y)+\rangle$ and $|G_{3t}(y)-\rangle$, with periodic varying eigenfrequencies $\lambda_{G_{3t(y)\pm}} = -\Delta_3/2 \pm \sqrt{\Delta_3^2/4 + |G_{3t}(y)|^2}$. Next, the secondary dressing fields $\boldsymbol{E}_2$ and $\boldsymbol{E}_2^{'}$ also have dressing effect and the first-order dressing state $|G_{3t}(y)+\rangle$ ($|G_{3t}(y)-\rangle$) will be split into two second-order dressing states $|G_{3t}(y) + G_{2t}(x)+\rangle$ and $|G_{3t}(y) + G_{2t}(x)-\rangle$ ($|G_{3t}(y) - G_{2t}(x)+\rangle$ and $|G_{3t}(y) - G_{2t}(x)-\rangle$), given that $\boldsymbol{E}_2$ and $\boldsymbol{E}_2^{'}$ near the resonance with $|G_{3t}(y)+\rangle$ ($|G_{3t}(y)-\rangle$). Obviously, the frequencies of the two second-order dressing states $|G_{3t}(y) + G_{2t}(x)\pm\rangle$ and $|G_{3t}(y) - G_{2t}(x)\pm\rangle$ are periodical, as shown in Fig. 22 (b). Such spatial periodic energy leves can lead to

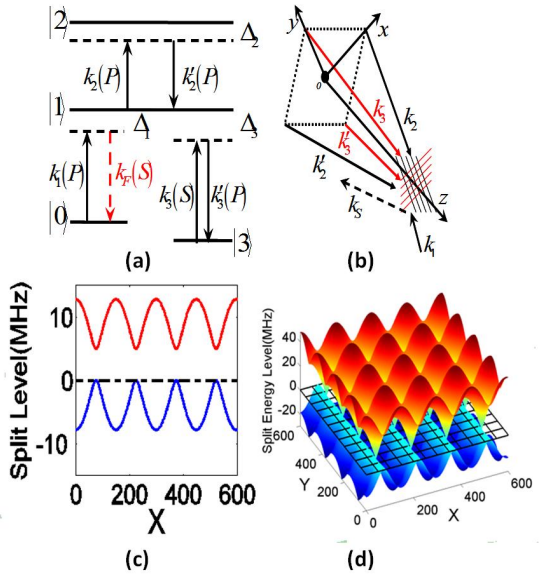

FIG. 22. The Schematic of the R-Y type atomic level system to produce MWM signals: (a) The doubly-dressed FWM. (b) The geometric configuration to generate SWM signal; k_2 and $k_2^{'}$ form a SW (black grating) along x, k_3 and $k_3^{'}$ form a SW (red grating) along y. (c) Single-dressing FWM enhancement effect. (d) Doubly dressed FWM enhancement effect

periodic enhancement or suppression of Kerr effect, and furthermore spatial periodic nonlinear refractive index, i.e., generate the EIG which has PBG, and the probe beam with frequency falling within this PBG will be reflected strongly to generate the FWM signal. So the FWM can be modulated by the EIG to have spatial periodic profile.

2. Method to Calculate PBG

Generally speaking, there are two methods available to calculate the PBG which stems from periodic laser-atom interaction system, namely, the methods of plane wave expansion and transfer matrix. In transfer matrix method[1], the EIG or EIL can be divided into many layers, and the refractive index of each layer is supposed to be constant. The relationship between the incident and outgoing light field of each layer is connected by a transfer matrix of the layer itself. Thus the transfer matrix of the EIG or EIL in the medium can be calculated by the product of each layer's. Furthermore, considering the Bloch's theorem, the PBG can be obtained numerically by solving the equation $m\pi/a+ik^{'} = \cos^{-1}\{\mathrm{Tr}[T_\Lambda(\Delta)]\}/\Lambda$, the left hand sides of which means that the real part of the Bloch wavevector is around the edge of the Brillouin region, the imaginary part is nonzero, a is the EIG period, and the incident field (probe field) detuning Δ-dependent T_Λ is the transfer matrix of one period in the EIGs. For one period, the total transfer matrix can be expressed by $T_\Lambda(\Delta) = \sum_{j=1}^{N} T_j(\Delta)$, where T_j is the transfer matrix of the j-th layer when we divide the whole period into N layers, and its dependence on the probe field detuning is obvious.

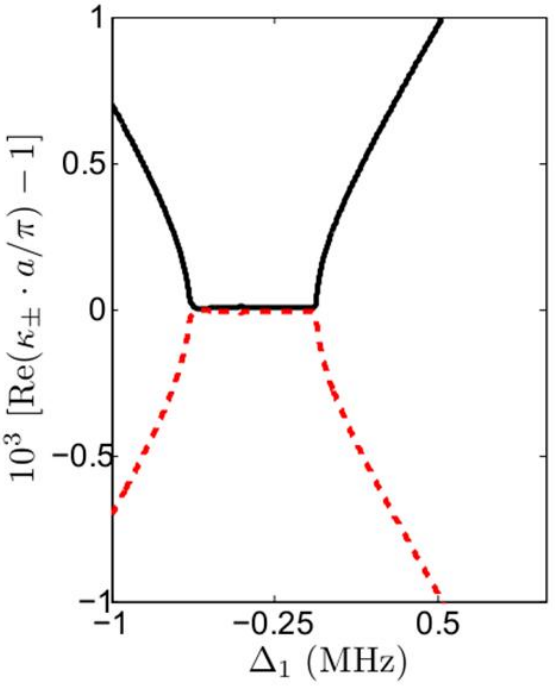

FIG. 23. The PBG calculated by the plane wave expansion method

Here, we additionally discuss the plane wave expansion method to calculate the PBG. The spatially modulated total linear and nonlinear refractive index is given by $n(\zeta) = n_0 + \delta n_1 \cos(2k_2\zeta) + \delta n_2 \cos(4k_2\zeta)$, where n_0 is the spatially uniform refractive index; δn_1 and δn_2 are the coefficients for spatially varying terms for the modulated index. By expanding the electrical field of the incident field into Fourier series multiplying the Bloch wave, and the spatially periodical index into Fourier series, then substituting this two expressions into the Maxwell equation, next solving the homogeneous equations, we can obtain

$$\kappa_\pm = k_i \pm \sqrt{\{k_\mathrm{p}^2[1+\chi_1+(\chi_2^2-\chi_3^2)\chi_2'] - k_i^2\}^2 - k_\mathrm{p}^4[\chi_2\chi_3\chi_2' + (\chi_2^2+2\chi_2\chi_3)\chi_3']^2}/2k_i,$$

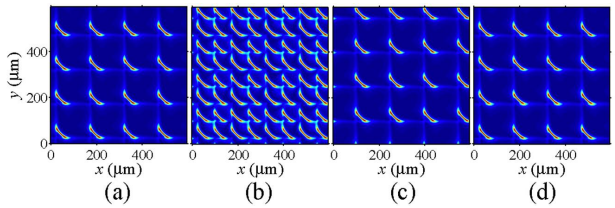

FIG. 24. The three panels are the cut plots of the Talbot effect at the initial place (a), the quarter Talbot length (b) and the Talbot plane (c)

which is called dispersion relation and reveals the relation between the Bloch wave-vectors $\kappa_{\pm}$ and the probe field Δ_1. Here, χ_m & $\chi_m^{'}$ $(m = 1, 2, 3)$ are the Fourier coefficients of the susceptibility; k_i is the wave vector component projected on the EIG periodic orientation of the probe field. A region of Δ_1 can be found satisfying $\mathrm{Re}(k_{\pm}a_i/\pi - 1) = 0$, which is right the PBG. As an instance, Fig. 23 shows the PBG calculated by the plane expansion method, in which the flat region represents the PBG.

3. Nonlinear Talbot Effect

The Talbot effect[2~6], first observed by H. F. Talbot in 1836, is a near-field diffraction phenomenon in which the light field spatially imprinted with periodic structure can have self-imaging at certain periodic imaging planes (the so-called Talbot plane). Such self-imaging effect holds a range of applications from image preprocessing and synthesis to optical computing[7]. In this following paragraph, we will give an introduction on how to generate controllable Talbot self-imaging with FWM and SWM signals.

Since dressing effect can modify the FWM and SWM signals, we can construct spatial periodic dressing effect to modify the usual spatial uniform MWM signals into spatial periodically dressed signals, with spatial periodic intensity distribution in the transverse dimension. The periodic pattern of the MWM signals can be flexibly controlled by adjusting the atomic coherence.

The Talbot effect with EIG[8] in higher nonlinear optical process has been studied. Specifically, the 1D and 2D periodic dressing effects are determined by the spatial periodic Rabi frequency $|G_{2t}(x)|^2$ and $|G_{2t}(x)|^2$ & $|G_{3t}(y)|^2$, respectively. Taking the 2-D case for instance, we can obtain the dressing states $|G_{3t}(y) + |G_{2t}(x)\pm\rangle$ and $|G_{3t}(y) - G_{2t}(x)\pm\rangle$ with 2-D periodic varying frequencies $\lambda_{G_{3t}(y)+G_{2t}(x)\pm}$ and $\lambda_{G_{3t}(y)-G_{2t}(x)\pm}$, as shown in Fig. 24 (b). Then the periodic enhancement condition, suppression condition can be obtained, and the FWM is modulated to have spatial periodic intensity distribution.

Now, we consider the propagation of the periodic FWM (SWM) signals. For simplicity, we define that the signal output plane as $z = 0$, adopt the paraxial approximation. Therefore, the propagation of the MWM signals can be regarded as a Fresnel diffraction process. In the perspective of Fourier optics, the transfer function of a Fresnel diffraction system with z as the propagation axis can be expressed as $H_{\mathrm{F}}(\xi) = \exp(ik_{z_0}z)\exp(-i\pi\lambda z\xi^2)$, where ξ is the spatial frequency and k_{z_0} is the input signal wave-vector projected on the z axis. It is obvious that a signal with multi-ξ components can be distorted in the propagation because a ξ-quadratic phase is introduced to it in the diffraction. However, for the periodic MWM signal described above, the self-imaging without distortion at certain propagation lengths can be demonstrated. The periodical electrical field distribution of the MWM signal $g_0(x, y)$ can be expanded into 2D Fourier series as $g_0(x, y) = \Sigma_{m,n=-\infty}^{\infty} c_{m,n}\exp[i2\pi(nx/d_x + my/d_y)]$ and in spatial frequency domain can be further written as $G_0(\xi, \eta) = \Sigma_{m,n=-\infty}^{\infty} c_{m,n}\delta(\xi - n/d_x) \cdot \delta(\eta - m/d_y)$, where $c_{m,n}$ is the Fourier coefficient. So, after the Fresnel diffraction, multiplying the MWM signal and the transfer function in spatial frequency domain, we can obtain the MWM signal at a z distance as: $G(\xi, \eta) = \sum_{m,n=-\infty}^{\infty} c_{m,n}\delta(\xi - n/d_x) \cdot \delta(\eta - m/d_y)\exp(ik_{z_0}z)\exp\{i\pi\lambda_1 z[(n/d_x)^2 + (m/d_y)^2]\}$, where k_{z_0} is the projection of the MWM signal wave vector on z the axis. So after inverse Fourier transformation, we can get the signal field $g(x) = g_0(x)\exp(ik_{z_0}z)$ In light of the fact that $|g(x)|^2 = |g_0(x)|^2$, we say at $z = 2qd_x^2/\lambda_1$ we can see the self-image of the MWM signals, and $z_{\mathrm{T}} = z|_{q=1}$ is defined as the Talbot length.

4. Third- and Fifth-Order Nonlinearities

In nonlinear optics[9,10], the susceptibility χ connects with the refractive index of the medium by the relation $n = \sqrt{1 + \mathrm{Re}(\chi)}$. Taking into account higher-order terms one can represent the refractive index as power-law Kerr-type nonlinearity, $n = n_1 + n_2 I + n_4 I^2 + \cdots$ with the intensity $I = \varepsilon_0 c|E|^2/2$. Obviously, if nonlinear coefficients n_2 and n_4 have the same signs, the corresponding models exhibit simply increasing strength of nonlinear self-action, self-focusing for $n_2 > 0$ and $n_4 > 0$ or self-defocusing for $n_2 < 0$ and $n_4 < 0$. More interesting situation occurs if the two nonlinear contributions have opposite signs, i.e., $n_2 n_4 < 0$ and this case is usually called the "competing" cubic-quintic (CQ) nonlinearity, which is widely used in solitonic science to seek stable higher-order soliton solutions. Let n_4 be a self-focusing type,

i.e., $n_4 > 0$. Then, for any sign of Kerr contribution n_2, there will be a threshold power of light beam $\boldsymbol{E}$, above which higher-order self-focusing will predominate both the linear diffraction and n_2 contribution. In this case the beam will collapse, similar to the pure Kerr case with $n_2 > 0$ and $n_4 = 0$. However, if $n_4 < 0$, then the collapse can be suppressed, for the light beam with high enough intensity experience effectively self-defocusing environment, i.e., $\mathrm{d}n/\mathrm{d}I < 0$. Here the threshold intensity is given by $I_{\mathrm{th}} = -n_2/2n_4$. That is the reason why CQ nonlinearity can be a charming research focus in the past decades.

As one example, even though higher-order solitons cannot stably exist in a Kerr medium, they have been numerically confirmed in a system with CQ nonlinearity. Experimentally, a CQ nonlinear dielectric response with positive cubic and negative quintic contributions has been observed in chalcogenide glasses, and in organic materials. However, in all these cases the quintic nonlinearity is accompanied by significant higher-order multiphoton processes such as two-photon absorption, therefore the validity of the CQ models to light propagation in these materials requires additional explorations. If both the third-order and fifth-order nonlinearities can be enhanced with EIT, and at the same time the absorption can be effectively suppressed, the formation of a higher order stability soliton will be ensured.

C. EISD and Splitting of FWM

1. Spatial Dispersion of FWM Beams

Spatial displacements of the probe and generated FWM beams are observed in a three-level V-type, as well as a two-level, atomic system near resonance. The observed spatial dispersion curves reflect the typical dispersion properties in the EIT systems and are the results of the cross-Kerr nonlinear coefficients enhanced by the induced atomic coherence in the multi-level systems. The spatial beam displacements of the weak probe and the FWM signal beams are controlled by the strong control laser beam and the atomic density. Studying such controlled spatial beam shifts can be important in image storage and in generating spatially correlated (entangled) laser beams in multi-level EIT systems. In this section, we show that by arranging the laser beams in a certain spatial configuration, such sharp dispersive features in frequency domain for the probe beam can be converted into spatial beam displacement controlled by the strong coupling laser beam. For a three-level V-type system, as shown in Fig. 25 (a), the control (coupling) beam $\boldsymbol{E}_2$ in one transition can spatially deflect the probe beam $\boldsymbol{E}_{\mathrm{p}}$ in another transition when these two laser beams propagate through the atomic medium with a small angle. As the probe frequency is detuned, the spatial deflection shows a dispersion-like change in its displacement, which exactly mimics the dispersion curve as observed for the Kerr-nonlinear index of refraction in the EIT system. Also, when two additional pump laser beams ($\boldsymbol{E}_1$ and $\boldsymbol{E}_1^{'}$) are applied to the probe transition, as shown in Fig. 25 (b), to generate a FWM signal $\boldsymbol{E}_{\mathrm{F1}}$, this FWM signal can also be spatially displaced by $\boldsymbol{E}_2$. Again, a dispersion-like spatial deflection curve for the FWM signal is seen with respect to the probe frequency detuning. Such EISD can be used for spatial switching and routing, and as an easy way to measure the Kerr-nonlinear indices of refraction for the multi-level atomic media. When the control beam $\boldsymbol{E}_2$ is tuned to the same transition as the probe and pump beams, as shown in Fig. 25 (c), it becomes an effective two-level system. Efficient deflection of $\boldsymbol{E}_{\mathrm{F1}}$ by $\boldsymbol{E}_2$ in such two-level atomic system has been also observed and compared with the three-level V-type system.

There are several features in this work that are distinctly different and advantageous over the previously studied spatial shifts of laser beams in atomic systems. First, the EISD of both the probe beam and the generated FWM beam can be directly observed and controlled by another strong (control) laser beam. Second, the cross-Kerr nonlinear index n_2 can be directly measured by such simple EISD technique. Third, enhanced cross-Kerr nonlinearity in spatial domain can be achieved by increasing atomic density (cell temperature) or the power of the strong control beam. Also, the effects of different dressing schemes on spatial deflection of the FWM beam have been carefully considered and compared.

Under our experimental conditions, the sodium vapor is an EIT-enhanced Kerr medium for the propagating laser beams. The laser beam $\boldsymbol{E}_2$ (or $\boldsymbol{E}_1$) is approximately 10^2 times stronger than the beam $\boldsymbol{E}_1^{'}$, and 10^4 times stronger than the weak probe beam $\boldsymbol{E}_{\mathrm{p}}$, so $\boldsymbol{E}_1$ and $\boldsymbol{E}_2$ beams can control the weaker $\boldsymbol{E}_{\mathrm{p}}$ and $\boldsymbol{E}_{\mathrm{F1}}$ beams. At the same time, the field $\boldsymbol{E}_1^{'}$ can also slightly affect the displacement of the $\boldsymbol{E}_{\mathrm{F1}}$ beam. The mathematical description of the propagation properties of the weak beams $\boldsymbol{E}_{\mathrm{p}}$ and $\boldsymbol{E}_{\mathrm{F1}}$ due to self- and cross-Kerr nonlinearities of the control and pump beams can be obtained through numerically solving the following coupled equations:

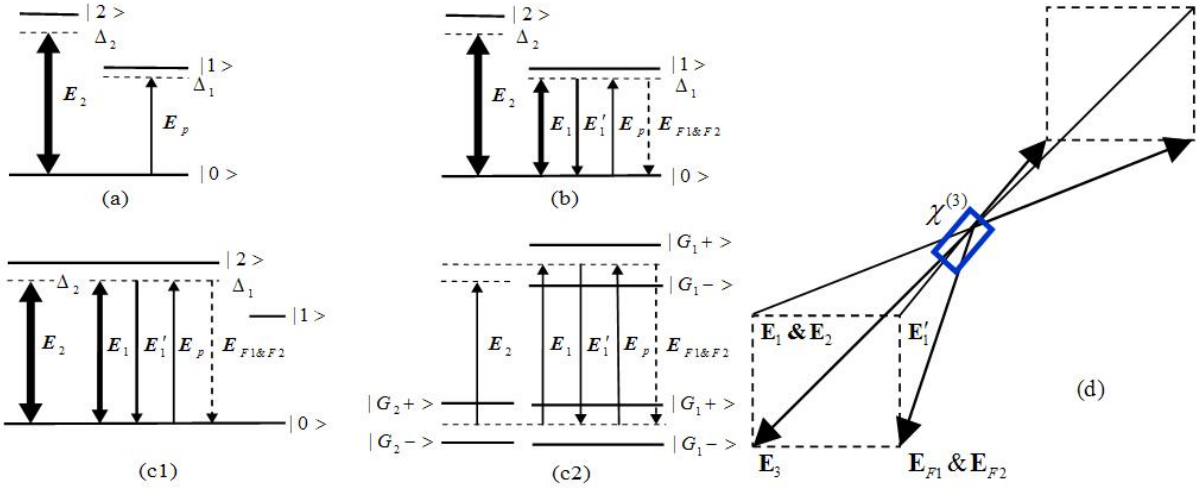

FIG. 25. (a) Three-level V-type EIT system. (b) Three-level V-type system with FWM signal $\boldsymbol{E}_{\rm F1}$ generated by the pump beams ($\boldsymbol{E}_1$, $\boldsymbol{E}_1^{'}$) and the probe beam ($\boldsymbol{E}_{\rm p}$) in the transition $|0\rangle - |1\rangle$. The FWM process can be modified by the control beam $\boldsymbol{E}_2$. (c1) Two-level system with four laser beams tuned to the same transition. (c2) Dressed-state picture corresponding to the two-level system in (c1). (d) Spatial beam geometry used in the experiments

$$\frac{\partial E_{\rm p}}{\partial z} - \frac{i\nabla_{\perp}^2 E_{\rm p}}{2k_{\rm p}} = \frac{ik_{\rm p}}{n_0}(n_2^{S1}|E_{\rm p}|^2 + 2n_2^{X1}|E_1|^2 + 2n_2^{X2}|E_2|^2)E_{\rm p} \tag{23-1}$$

$$\frac{\partial E_{\rm F1}}{\partial z} - \frac{i\nabla_{\perp}^2 E_{\rm F1}}{2k_{\rm F1}} = \frac{ik_{\rm F1}}{n_0}[n_2^{S2}|E_{\rm F1}|^2 + 2n_2^{X3}|E_1|^2 + 2n_2^{X4}|E_2|^2 + 2n_2^{X5}|E_1^{'}|^2]E_{\rm F1} \tag{23-2}$$

where z is the longitudinal coordinate in the propagation direction, $k_{\rm p} = k_{\rm F1} = \omega_1 n_0/c$, n_0 is the linear refractive index at ω_1, $n_2^{S1,S2}$ are the self-Kerr nonlinear coefficients of the fields $\boldsymbol{E}_{\rm p}$ and $\boldsymbol{E}_{\rm F1}$, and n_2^{X1-X5} are the cross-Kerr nonlinear coefficients due to the fields $\boldsymbol{E}_{1,2}$ and $\boldsymbol{E}_1^{'}$, respectively. These nonlinear Kerr coefficients can be controlled by the parameters of the relevant laser fields, such as field detuning and power. Since high-power pulsed dye lasers are used in the experiment, Doppler effect and the power broadening effect are considered in the calculation according to Eq. (23). By assuming Gaussian profiles for the input fields, Eqs. (23-1) and (23-2) are solved by using the split-step Fourier method.

Figure 26 shows spatial displacements of $\boldsymbol{E}_{\rm p}$ and $\boldsymbol{E}_{\rm F1}$, respectively, versus frequency detuning Δ_1 ($\Delta_1 = \Omega_1 - \omega_1$ for the three-level system or $\Omega_2 - \omega_1$ for the two-level system) with a fixed control beam ($\Delta_2 = \Omega_2 - \omega_2 = 0$). When the pump beams $\boldsymbol{E}_1$ and $\boldsymbol{E}_1^{'}$ are blocked (Fig. 25 (a)), it is the simple three-level V-type EIT system. For the fixed $\boldsymbol{E}_2$, the measured probe beam displacements show a spatial dispersion-like displacement curve as depicted in Fig. 26 (a) (the triangle points). The data points can be fitted well with the calculated n_2 versus Δ_1. The inset in Fig. 26 (a) shows the images of the measured probe beam spots versus Δ_1 in the two-level system. In the $\Delta_1 < 0$ region, the smaller beam spots are an indication of self-focusing effect for the probe beam due to positive self-Kerr nonlinear index, while the larger beam spots in $\Delta_1 > 0$ region are due to self-defocusing because of the sign change in the self-Kerr nonlinear coefficient. When $\boldsymbol{E}_{\rm p}$ is tuned to the transition $|0\rangle - |2\rangle$, the system becomes an effective two-level one. Similarly, with $\boldsymbol{E}_2$ fixed, the spatial displacements (black squares) also show the same dispersion-like curve, as shown in Fig. 26 (a). Again the solid (black) line is the calculated cross-Kerr nonlinear coefficients as a function of Δ_1, which fits perfectly well with the measured EISD. When the pump beams ($\boldsymbol{E}_1$ and $\boldsymbol{E}_1^{'}$) are on (Fig. 25 (b)), an efficient FWM signal $\boldsymbol{E}_{\rm F1}$ is generated by the pump beams together with the probe beam, which propagates in a different direction as shown in Fig. 25 (d). With a fixed $\boldsymbol{E}_2$, the generated $\boldsymbol{E}_{\rm F1}$ (in either the three-level or the two-level system) is deflected differently when the frequency de-

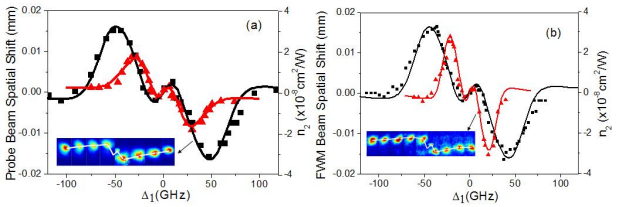

FIG. 26. (a) EISD shift of the beam $\boldsymbol{E}_{\rm p}$ and the fitted cross-Kerr nonlinear coefficient n_2 versus Δ_1 at 230°C in the two-level system (black squares) and the three-level system (red triangles), respectively. Inset: EISD spots of $\boldsymbol{E}_{\rm p}$ versus Δ_1 in the two-level system. (b) EISD shift of the beam $\boldsymbol{E}_{\rm F1}$ and the fitted cross-Kerr nonlinear coefficient versus Δ_1 at 230°C in the two-level system (black squares) and the three-level system (red triangles), respectively. Inset: EISD spots of $\boldsymbol{E}_{\rm F1}$ versus Δ_1 in the three level V-type system. The parameters are $G_{\rm p} = 0.2$ GHz, $G_1 = G_1^{'}$ =1.1 GHz and G_2 =9.7 GHz[29]

tuning of the probe beam (Δ_1) is scanned, as shown in Fig. 26 (b). The dispersion-like curves are narrower than the probe beam deflections, but the general behaviors are very similar to the ones as in Fig. 26 (a). The spatial deflection curves are well fitted with the calculated cross-Kerr nonlinear indices of refraction for the three-level V-type and two-level systems (solid curves), respectively. The inset in Fig. 26 (b) shows the images of the measured FWM beam spots versus Δ_1 in the three-level system.

The observed spatial displacements of the probe ($\boldsymbol{E}_{\rm p}$) and FWM ($\boldsymbol{E}_{\rm F1}$) beams are caused by the noncolinear propagations of the laser beams and the enhanced cross-Kerr nonlinear indices of refraction due to the strong laser beams $\boldsymbol{E}_2$ and $\boldsymbol{E}_1$. For simplicity, let's only consider the strong control beam $\boldsymbol{E}_2$. During its propagation through the vapor cell, the wing of $\boldsymbol{E}_2$ interacts with the intensity profile of either $\boldsymbol{E}_{\rm p}$ or $\boldsymbol{E}_{\rm F1}$, and distorts its phase profile to induce an optical waveguide through XPM. The nonlinear phase shift can be written as $\phi_{NL} = 2k_{\rm F1}n_2|A_2|^2z/n_0$ and the additional transverse propagation wave-vector is $\delta k_\perp = \phi_{NL}^{'}$. In this case, when $n_2 > 0$, the direction of $\delta k_\perp$ is to the beam center of $\boldsymbol{E}_2$, and, therefore, $\boldsymbol{E}_{\rm p,F1}$ is deflected closer to $\boldsymbol{E}_2$; when $n_2 < 0$, the direction of $\delta k_\perp$ is outward from the beam center of $\boldsymbol{E}_2$, thus $\boldsymbol{E}_{\rm p,F1}$ is deflected away from $\boldsymbol{E}_2$. According to the expression for ϕ_{NL}, the amount of spatial shift is proportional to the cross-Kerr nonlinear coefficient, the field intensity and the propagation distance. Hence, the spatial displacements of the probe and FWM beams results from the cross-Kerr nonlinear coefficient induced by the strong control field, and therefore can be controlled by it.

The spatial displacements of the probe and FWM beams are mainly determined and controlled by the large cross-Kerr nonlinear coefficients of the strong laser fields. However, the cross-Kerr effects induced by the relatively weaker pump beam(s) can also exist. Since each of the pump and probe beams can be spatially displaced by the strong control beam (and by each other), the final spatial displacement of the generated FWM beam can be affected by such secondary displacement effects. In the above discussion and calculations, we have only considered the leading contributions from the strongest fields, which explained the observed spatial displacements quite well. Also, when $\boldsymbol{E}_{\rm p}$ and $\boldsymbol{E}_{\rm F1}$ get stronger (with higher probe and more efficient FWM process), incoherently coupled soliton pairs can be formed by $\boldsymbol{E}_{\rm p}$ and $\boldsymbol{E}_{\rm F1}$ due to the interplays between the diffraction effect and self-Kerr nonlinear effect. Under such conditions, we can obtain the solutions of $A_{\rm p,F1}(x) = A_0{\rm sech}(A_0x)$ for the bright-bright soliton pair in the self-focusing EIT media and of $A_{\rm p,F1}(x) = A_0[1 - {\rm sech}^2(A_0x)]^{1/2}$ for the dark-dark soliton pair in self-defocusing EIT media. Here A_0 is the initial envelope amplitude. The enhanced self-Kerr and cross-Kerr nonlinear coefficients due to induced atomic coherence or EISD enable the formations of such spatial soliton pairs with much lower input laser powers, which can be very important for their applications in optical communications.

2. Spatial Split of FWM Images

In the previous section, due to the enhanced cross-Kerr nonlinear effects, the EISD shifts for the proble as well as the FWM beams can be experimentally observed. The observed spatial displacements are fitted to the calculated cross-Kerr nonlinear coefficients in the systems, which provide a new and easier way to determined various cross-Kerr nonlinear coefficients in the multi-level atomic systems. In this section, we will present how to achieve spatial splitting by enhanced cross-Kerr nonlinear effects, the detailed experimental setups and configuration are similar to the case of spatial shift experiment in Fig. 25. More information can be found in Ref. [11].

As shown in the insets of Figs. 27 (a) and (b) (lower panels), the probe and FWM signal ($\boldsymbol{E}_{\rm F1}$) beams are displaced and split as the frequency detuning Δ_1 of the probe beam is scanned through resonance. The displacements of the probe and FWM beams follow the shape of nonlinear dispersion. Here, we only concentrate on the beam splitting effect. Figure 27 (a) gives the splitting distance of the probe beam for different Δ_1. The solid curve is a fit to the cross-Kerr nonlinear index n_2 for the probe beam. The splitting distance of $\boldsymbol{E}_{\rm F1}$ is given in Fig. 27 (b) as a function of Δ_1, which is also fitted to n_2, as will be discussed later.

The Kerr nonlinear index is always zero at the exact

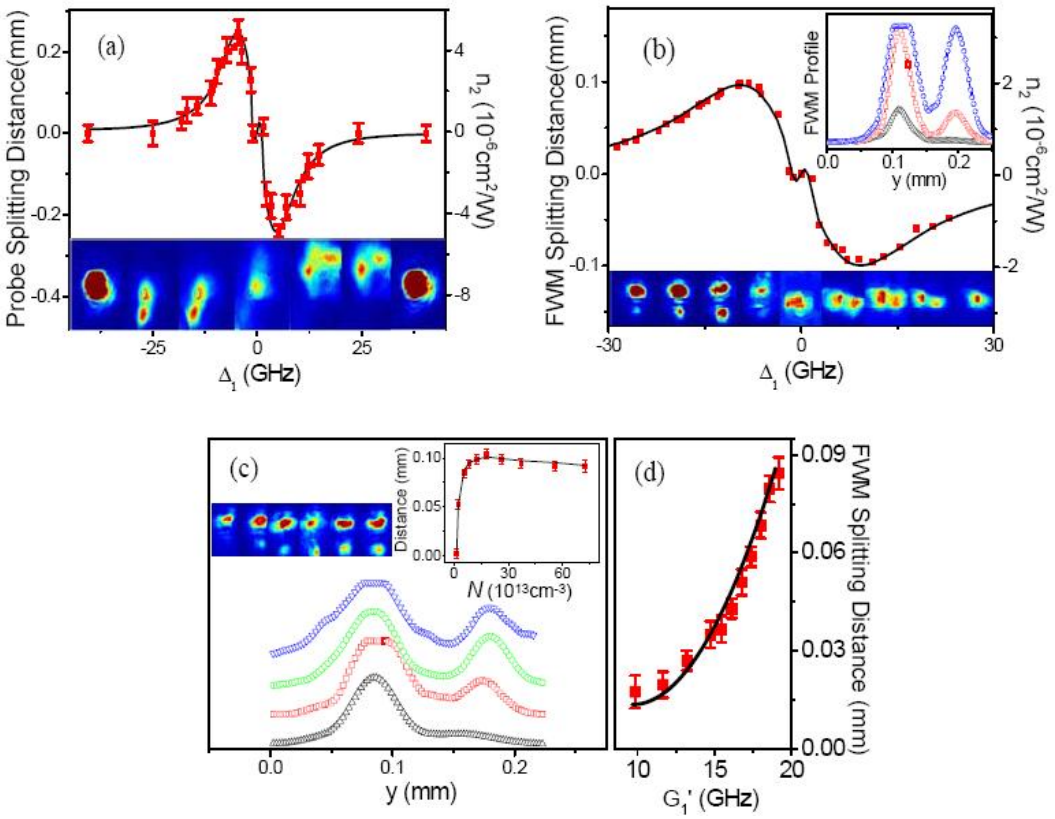

FIG. 27. (a) Measured probe beam splitting versus Δ_1 (square) and the fitted n_2 curve (solid) with $G_1^{'}$ =20.6 GHz at 250°C. Inset: spots of the probe beam versus Δ_1. (b) Measured $\boldsymbol{E}_{\rm F1}$ beam splitting versus Δ_1 (square) and the fitted n_2 curve (solid) with $G_1^{'}$ =20.6 GHz at 265°C. Inset: $\boldsymbol{E}_{\rm F1}$ beam profiles with $\Delta_1 = -30$ GHz (triangle), $\Delta_1 = -22$ GHz (square), $\Delta_1 = -17$ GHz (circle) in top right corner; and spots of the $\boldsymbol{E}_{\rm F1}$ beam versus Δ_1 in bottom. (c) $\boldsymbol{E}_{\rm F1}$ beam profiles at 230°C (triangle), 240°C (square), 260°C (circle) and 280°C (reverse triangle), respectively, with $G_1^{'}$=20.6 GHz at $\Delta_1 = -10$ GHz . Inset: $\boldsymbol{E}_{\rm F1}$ beam splitting versus atomic density N. Spots of $\boldsymbol{E}_{\rm F1}$ beam versus N. (d) $\boldsymbol{E}_{\rm F1}$ beam splitting versus $G_1^{'}$ with $\Delta_1 = -10$ GHz at 265°C. The other parameters are $\Delta_2 = 0$, $G_2 = 0$, G_1 =1.5 GHz , and $G_2^{'}$ =10.8 GHz[30]

resonant condition. The temperature dependence of the FWM beam splitting distance is given in Fig. 27 (c), which shows a quick increase as temperature rises and then a slow decrease as the temperature further increases. Double-beam profiles are clearly shown in the figure. The intensity dependence of the FWM beam shift as a function of the pump beam ($\boldsymbol{E}_1^{'}$) intensity is depicted in Fig. 27 (d), which gives a continued increase as $G_1^{'}$ gets larger. It is interesting to notice that when $\Delta_1 < 0$ the beam splitting occurs in the y (vertical) direction, but split in the x (horizontal) direction when $\Delta_1 > 0$ as shown in Figs. 27 (a) and (b), respectively. This phenomenon can be explained by the relative positions between the weak beams and the strong dressing (controlling) beams. For the weak probe beam $\boldsymbol{E}_3$ (Fig. 27 (a)), in the $\Delta_1 < 0$ region, the beam shift in the y direction results from the attraction ($n_2 > 0$) of the strong $\boldsymbol{E}_2^{'}$ beam. This makes it get closer to $\boldsymbol{E}_2^{'}$, which also splits the probe beam in y direction. In the $\Delta_1 > 0$ region, the probe beam shifts to the down-right direction due to the repulsion ($n_2 < 0$) of $\boldsymbol{E}_2^{'}$ (which is slightly misaligned to the left side) and gets closer to $\boldsymbol{E}_1^{'}$, which can split the probe beam in x direction. Also, for the weak FWM beam $\boldsymbol{E}_{\rm F1}$ (Fig. 27 (b)), in the $\Delta_1 < 0$ region, it shifts above $\boldsymbol{E}_1^{'}$ in the y direction induced by $\boldsymbol{E}_2^{'}$, and such $\boldsymbol{E}_1^{'}$ beam can split $\boldsymbol{E}_{\rm F1}$ in y direction. While in the $\Delta_1 > 0$ region, the FWM $\boldsymbol{E}_{\rm F1}$ beam shifts in the down-right direction due to the repulsion ($n_2 < 0$) of $\boldsymbol{E}_2^{'}$ and therefore, splits in x direction induced by $\boldsymbol{E}_1^{'}$.

Figure 28 depicts the beam profiles of the FWM beam $\boldsymbol{E}_{\rm F2}$ as a function of various parameters. Figure 28 (a) presents $\boldsymbol{E}_{\rm F2}$ profiles for different probe frequency detuning Δ_1. As one can see that the beam breaks up into two beams at certain value of Δ_1. For $\Delta_1 < 0$ the atomic system is a focusing medium due to self-Kerr nonlinearity. The insets in Fig. 28 show

the spatial beam images.

To understand the observed beam splitting of the probe and FWM beams, we need to consider various SPM and XPM processes. The spatial beam breaking is mainly due to the overlap between the weak probe and/or FWM beams and the strong coupling or pump beams. Due to XPM, the nonlinear phase can have more than one minimum when the cross-Kerr index n_2 increases, which generates several intensity minima in the profiles of the FWM beams. The propagation equations for the probe and FWM beams with only the most relevant coupling/pump beams for beam splitting are

$$\frac{\partial E_3}{\partial z} - \frac{i\nabla_\perp^2 E_3}{2k_3} = \frac{ik_3}{n_1}\left[n_2^{S1}|E_3|^2 + 2n_2^{X1}|E_1^{'}|^2 + 2n_2^{X2}|E_2^{'}|^2\right]E_3 \tag{24-1}$$

$$\frac{\partial E_{\rm F1}}{\partial z} - \frac{i\nabla_\perp^2 E_{\rm F1}}{2k_{\rm F1}} = \frac{ik_{\rm F1}}{n_1}\left[n_2^{S2}|E_{\rm F1}|^2 + 2n_2^{X3}|E_1^{'}|^2\right]E_{\rm F1} \tag{24-2}$$

$$\frac{\partial E_{\rm F2}}{\partial z} - \frac{i\nabla_\perp^2 E_{\rm F2}}{2k_{\rm F2}} = \frac{ik_{\rm F2}}{n_1}\left[n_2^{S3}|E_{\rm F2}|^2 + 2n_2^{X4}|E_2^{'}|^2\right]E_{\rm F2} \tag{24-3}$$

Here, z is the longitudinal coordinate; $k_3 = k_{\rm F1} = k_{\rm F2} = \omega_1 n_1/c$; n_1 is the linear refractive index; n_2^{S1-S3} are the self-Kerr coefficients of $\boldsymbol{E_{3,F1,2}}$; n_2^{X1-X4} are the cross-Kerr coefficients of $\boldsymbol{E_{3,F1,2}}$ induced by $\boldsymbol{E_{1,2}}$ and $\boldsymbol{E_{1,2}^{'}}$. Equations (24) can be solved by using the commonly employed split-step Fourier method.

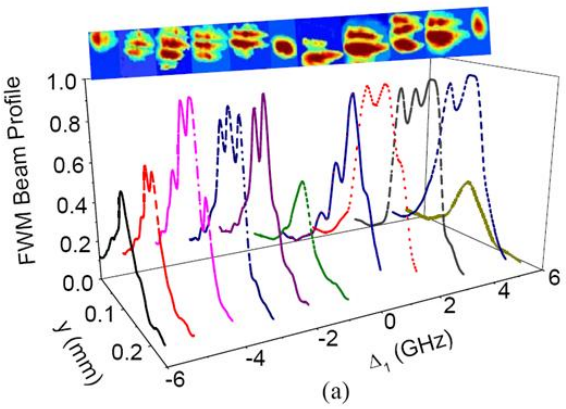

FIG. 28. (a) $\boldsymbol{E}_{\rm F2}$ beam profiles versus Δ_1 at 250°C. The other parameters are $G_1 = G_1^{'} = 0$, G_2 =1.9 GHz and $G_2^{'}$ =20.8 GHz. The solid lines are the experimental results and the dotted lines are the calculated $\boldsymbol{E}_{\rm F2}$ beam profiles

The Kerr nonlinear coefficient is negative for a self-defocusing medium and positive for a self-focusing one, which is given by $n_2 \approx {\rm Re}\rho_{10}^{(3)}/(\varepsilon_0 c n_0)$. One can solve the coupled density-matrix equations to obtain $\rho_{10}^{(3)}$, i.e., $\rho_a^{(3)} = -iG_{\rm F1}G_1^{'2}/[d_1\Gamma_1(d_1 + G_1^{'2}/\Gamma_0 + G_1^{'2}/\Gamma_1)]$ for n_2^{X3} (induced by the strong $\boldsymbol{E}_1^{'}$ field), $\rho_b^{(3)} = -iG_{\rm F2}G_2^{'2}/[d_1 d_2(d_1 + G_2^{'2}/d_2)]$ for n_2^{X4} (induced by $\boldsymbol{E}_2^{'}$) and $\rho_c^{(3)} = -iG_3G_{1,2}^{'2}/(d_1 d_2 d_3)$ for $n_2^{X1,2}$ (induced by both $\boldsymbol{E}_1^{'}$ and $\boldsymbol{E}_2^{'}$ fields) with $d_2 = \Gamma_1 + i(\Delta_1 - \Delta_2)$, $d_3 = d_1 + G_1^{'2}/\Gamma_1 + G_2^{'2}/(d_2 + G_1^{'2}/d_4)$, $d_4 = \Gamma_1 - i\Delta_2$. Here, $G_{\rm F1,F2}$ are the Rabi frequencies of $\boldsymbol{E}_{\rm F1,F2}$ and Δ_1 (Δ_2) is the detuning of the fields $\boldsymbol{E}_{1,3}$ and $\boldsymbol{E}_1^{'}$ ($\boldsymbol{E}_2$ and $\boldsymbol{E}_2^{'}$). In addition, these three weak beams can be spatially shifted by the other coupling/pump beams.

The solid curves in Fig. 27 (a) and (b) are the calculated cross-Kerr nonlinear coefficients, which show well to the measured data. So the measurements of spatial splitting can be used to determine the cross-Kerr nonlinear index. With fixed experimental parameters (such as atomic density, frequency detuning, spot sizes, and atomic decay rates), the measured beam profiles are fitted to the calculated results (from the propagation equations) with adjustable signal amplitudes and constant background, which show excellent agreements, as shown in Fig. 28. Such direct comparisons indicate the validity of Eqs. (24) in describing the spatial splitting of the FWM beams by other laser beams.

D. Stable Spatial FWM Solitons

1. FWM Dipole Soliton in Laser-Induced Atomic Gratings

As mentioned in the previous section, in the self-defocused nonlinear medium ($\Delta_1 > 0$), the XPM due to the presence of another laser beam can induce a focusing effect, which can be used to generate spatial solitons and other interesting nonlinear effects in the media. In this section, we show that charged dipole-

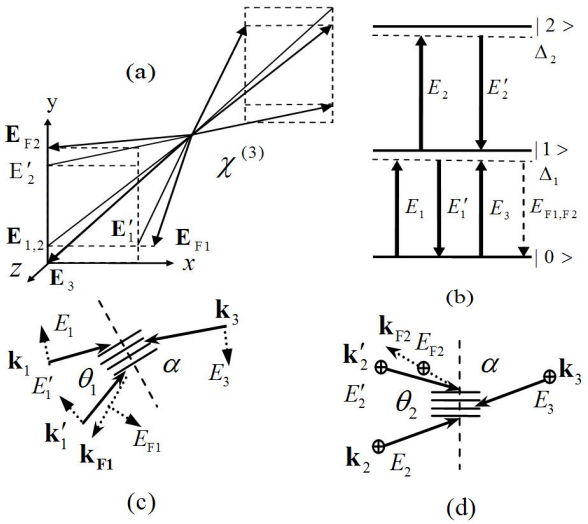

FIG. 29. spatial beam geometry used in the experiment. (b) Two FWM processes $\boldsymbol{E}_{\rm F1}$ and $\boldsymbol{E}_{\rm F2}$, with five beams $\boldsymbol{E}_1$, $\boldsymbol{E}_1^{'}$, $\boldsymbol{E}_2$, $\boldsymbol{E}_2^{'}$, and $\boldsymbol{E}_3$ on, in a cascade three-level atomic system. $\boldsymbol{E}_{\rm F1}$ (TM polarization) in (c) and $\boldsymbol{E}_{\rm F2}$ (TE polarization) in (d) are mainly steered by the horizontally- and vertically-aligned EIG1 and EIG2, respectively

mode solitons can be created in the FWM beams generated inside a multi-level atomic medium, in which the self-Kerr and cross-Kerr nonlinearities are greatly enhanced by laser-induced atomic coherences. The key to observe such novel dipole-mode solitons is to create a high enough index contrast (via Kerr nonlinearity $n_2 I$) in the atomic medium by laser-induced index gratings. Two component dipole-mode solitons are generated in two coexisting FWM signal beams in a three-level atomic system. The easy controls of experimental parameters in the multi-level atoms make the current system ideal to investigate the formations of multi-component spatial solitons and their nonlinear dynamics. One of the advantages of such spatial solitons is that the wave-guiding effect is induced by focusing due to the cross-Kerr nonlinearity of the FWM beam, not self-focusing which normally suffers catastrophic absorption.

Let us consider the EIG under the geometrical configuration as Fig. 29 (a) and energy level system as Fig. 29 (b). EIG can form when the weak probe beam $\boldsymbol{E}_3$, coupled to one atomic transition, interacts with two strong non-collinear beams (either beams $\boldsymbol{E}_1$ and $\boldsymbol{E}_1^{'}$ in Fig. 29 (c), or $\boldsymbol{E}_2$ and $\boldsymbol{E}_2^{'}$ in Fig. 29 (d)), that is coupled to the same or different atomic transition in an atomic medium. The beams $\boldsymbol{E}_1$ and $\boldsymbol{E}_1^{'}$ (or beams $\boldsymbol{E}_2$ and $\boldsymbol{E}_2^{'}$) induce their own grating EIG1 (or EIG2). Such periodic refractive-index changes create two photonic band gaps, which prohibit the probe propagation and give rise to the highly-efficient omnidirectional reflections. Thus, the FWM signals ($\boldsymbol{E}_{\rm F1}$ and $\boldsymbol{E}_{\rm F2}$) are the results of the electromagnetically-induced diffraction (EID) of the probe beam $\boldsymbol{E}_3$ by the induced EIG1 and EIG2, respectively. The fringe spacing of EIG1 and EIG2 are determined by $\alpha_i = \lambda_i/\theta_i$ $(i = 1, 2)$. The dipole-like patterns of $\boldsymbol{E}_{\rm F1}$ and $\boldsymbol{E}_{\rm F2}$ are created by the horizontally- and vertically-aligned EIG1 and EIG2, respectively. Furthermore, the generated FWMs and probe field can form a vector soliton.

A radially asymmetric dipole-mode vector soliton includes one nodeless component (the probe beam $\boldsymbol{E}_3$) and two dipole-like components with spatial structures of Hermite-Gaussian modes ($\rm HG_{10}$ for $\boldsymbol{E}_{\rm F1}$ and $\rm HG_{01}$ for $\boldsymbol{E}_{\rm F2}$). We mainly study two coupled FWM beams $\boldsymbol{E}_{\rm F1}$ and $\boldsymbol{E}_{\rm F2}$ (with the same frequency), which have perpendicularly oriented dipole components, propagating along z direction and diffusing along one transverse direction. We assume $\boldsymbol{E}_{\rm F1} = A_{\rm F1}(\zeta)\exp(ik_{\rm F1}z)$, $\boldsymbol{E}_{\rm F2} = A_{\rm F2}(\zeta)\exp(ik_{\rm F2}z)$ and $\boldsymbol{E}_{\rm tot} = \boldsymbol{E}_{\rm F1} + \boldsymbol{E}_{\rm F2}$. These two coupled FWM fields satisfy the evolution equations in the Kerr medium as:

$$\frac{\partial E_{\rm F1}}{\partial z} - \frac{i\nabla_\perp^2 E_{\rm F1}}{2k_{\rm F1}} = \frac{ik_{\rm F1}}{n_1}(n_2^{S1}|E_{\rm F1}|^2 + 2n_2^{X1}|E_1|^2 + 2n_2^{X2}|E_1^{'}|^2 + 2n_2^{X3}|E_2^{'}|^2)E_{\rm F1} + \eta_1 E_1 (E_1^{'})^* E_{\rm F2} \tag{25-1}$$

$$\frac{\partial E_{\rm F2}}{\partial z} - \frac{i\nabla_\perp^2 E_{\rm F2}}{2k_{\rm F2}} = \frac{ik_{\rm F2}}{n_1}(n_2^{S2}|E_{\rm F2}|^2 + 2n_2^{X4}|E_2|^2 + 2n_2^{X5}|E_2^{'}|^2 + 2n_2^{X6}|E_1^{'}|^2)E_{\rm F2} + \eta_2 E_2 (E_2^{'})^* E_{\rm F1} \tag{25-2}$$

Two-component dipole-mode solitons are natural results from such energy-dependent nonlinear propagation equations. $n_2^{S1,S2}$ are self-Kerr nonlinear coefficients of $\boldsymbol{E}_{\rm F1}$ and $\boldsymbol{E}_{\rm F2}$, and n_2^{X1-X6} are cross-Kerr nonlinear coefficients of $\boldsymbol{E}_{1,2}$ and $\boldsymbol{E}_{1,2}^{'}$ to $\boldsymbol{E}_{\rm F1}$ and $\boldsymbol{E}_{\rm F2}$, respectively. As mentioned above, these nonlinear coefficient can be also obtained according to the density matrix equation, and the density matrix elements have the form $\rho_{10}^{(3)} \propto 1/\prod_{i=1}^{3}[a_i + G_j^2\cos^2(k_2\zeta)]$, in which the periodic term is derived from the formation of EIG. The coefficients in the last terms in Eqs. (25-1) and (25-2) are $\eta_1 = \xi\mu_{10}^5 F_a$ and $\eta_2 = \xi\mu_{21}^5 F_b$ with $\xi = i4\pi\omega_1 N/ch^4$, where F_a and F_a relate to the Rabi frequencies of the involved fields, the frequency detuning Δ_1 (Δ_2) for $\boldsymbol{E}_{1,3,\rm F1,F2}$ and $\boldsymbol{E}_1^{'}$ ($\boldsymbol{E}_2$ and $\boldsymbol{E}_2^{'}$), and the relaxation rates of the system.

The resulting superposition of the two perpendicular dipole-soliton components, $\boldsymbol{E}_{\rm F1}$ and $\boldsymbol{E}_{\rm F2}$, is a generalization from a two-component dipole-mode soliton ($\boldsymbol{E}_3$, $\boldsymbol{E}_{\rm F}$) to a three-component one ($\boldsymbol{E}_3$, $\boldsymbol{E}_{\rm F1}$, $\boldsymbol{E}_{\rm F2}$). The total intensity ($I = |\boldsymbol{E}_3|^2 + |\boldsymbol{E}_{\rm F1}|^2 + |\boldsymbol{E}_{\rm F2}|^2$) is

quasi-stable in propagation after a long enough propagation distance (or high enough atomic density). The three components of the vector soliton carry topological charges 0, +1, −1, respectively, and the total angular momentum is zero ($m_{\rm F1}+m_{\rm F2}+m_3=0$), which makes the solution stable, where $m_{3,\rm F1,F2}$ are topological charges of $\boldsymbol{E}_{3,\rm F1,F2}$.

The in-phase dipole modes of $\boldsymbol{E}_{\rm F1}$ and $\boldsymbol{E}_{\rm F2}$ are created (or split) by the horizontally- and vertically-aligned EIG1 and EIG2, respectively. Thus, the two-component dipole-mode soliton solutions of $\boldsymbol{E}_{\rm F1}$ and $\boldsymbol{E}_{\rm F2}$ can be written as

$$E_{\rm F1} = u_1 \mathrm{sech}[u_1(k_{\rm F1}n_2^{S1}/n_0)^{1/2}(r-r_1)]\cos(M\varphi/2)\cdot \exp(im_{\rm F1}\varphi + i\phi_1)\exp(ik_{\rm F1}z)$$

and

$$E_{\rm F2} = u_2 \mathrm{sech}[u_2(k_{\rm F2}n_2^{S2}/n_0)^{1/2}(r-r_2)]\cos(M\varphi/2)\cdot \exp(im_{\rm F2}\varphi + i\phi_2)\exp(ik_{\rm F2}z),$$

where $u_{1,2}$ are soliton amplitudes; $r_{1,2}$ are initial peak positions; M is the number of intensity peaks; $\phi_{1,2}$ are nonlinear phase shifts ($\phi_{1,2}=2k_{1,2}n_2I_{2,1}\mathrm{e}^{-r^2/2}/n_1$). Such solutions possess the dipole-soliton characteristics, and two humps form the two poles of the dipole soliton, which are trapped jointly in the neighbour photonic fringes.

The generated FWM ($\boldsymbol{E}_{\rm F2}$) beam can be significantly influenced by the dressing beams $G_1^{'}$, G_1 or $G_1^{'}$ & G_1 in the cascade three-level system (Fig. 30). We present the vertical dipole-mode solitons of $\boldsymbol{E}_{\rm F2}$ with different dressing configurations. The $\boldsymbol{E}_{\rm F2}$ beam splits into two coherent spots (i.e., dipole pattern, as shown in Fig. 30) due to the modulated transverse nonlinear phase shift ϕ_2 induced by the vertically-aligned EIG2. At low nonlinear dispersion $|n_2|$, $\boldsymbol{E}_{\rm F2}$ only experiences the linear diffraction. With maximum $|n_2|$ at $|\Delta_1|$ =16.5 GHz (Fig. 30 (b)), vertically-oriented dipole soliton is generated due to the balanced interaction between the spatial diffraction and the cross-Kerr nonlinearity. In the self-focusing region of the atomic medium (from $\Delta_1=-30$ GHz to $\Delta_1=-10$ GHz), there exists energy exchange between the two parts of the $\boldsymbol{E}_{\rm F2}$ dipole mode. At resonance or large frequency detuning, the dipole-mode soliton of $\boldsymbol{E}_{\rm F2}$ decays into a nodeless fundamental one. Under the case of enhanced FWM due to dressing (satisfying $\Delta_1+\Delta_2=|G_1+G_1^{'}|^2/\Delta_2$) in Fig. 30 (a), $\boldsymbol{E}_{\rm F2}$ with both $G_1^{'}$ and G_1 dressing is stronger than with $G_1^{'}$ or G_1 dressing separately, or without dressing fields. For stronger $G_1^{'}$, the dressing effect of $G_1^{'}$ is larger than that of G_1. In the enhancement case with Δ_1 =16.5 GHz , the nonlinear refractive index is $n_2=-9\times10^{-7}$ cm^2/W for $\boldsymbol{E}_{\rm F2}$, which is much larger than $n_2=-2\times10^{-8}$ cm^2/W in the suppressed case with Δ_1 =4.5 GHz (satisfying $\Delta_1+\Delta_2\approx0$). The

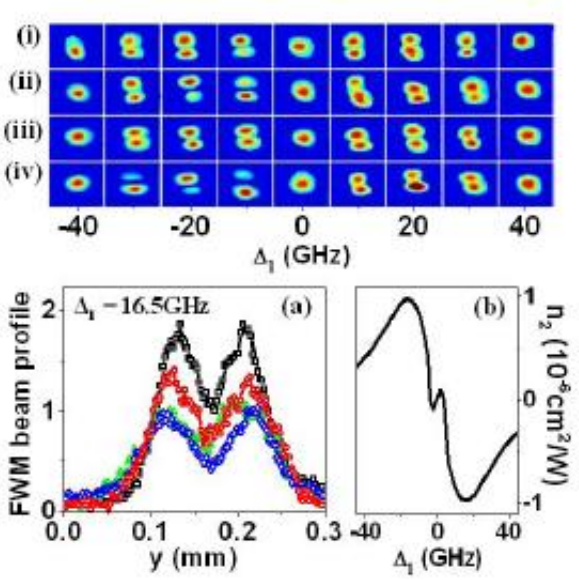

FIG. 30. Images at different Δ_1 (i-iv) and beam profiles at Δ_1 =16.5 GHz (a) of dipole-soliton $\boldsymbol{E}_{\rm F2}$ in the cascade three-level system with $G_2^{'}=G_2$ =20 GHz , $G_1^{'}$ =55 GHz and G_1 =45 GHz ((i) and squares), $G_1^{'}$ =55G Hz and G_1 =0 ((ii) and circles), $G_1^{'}$ =0 and G_1 = 45 GHz ((iii) and triangles), and without dressing fields ((iv) and diamonds). (b) Nonlinear refractive index n_2 of $\boldsymbol{E}_{\rm F2}$ with $G_1^{'}$ and G_1 dressings[58]

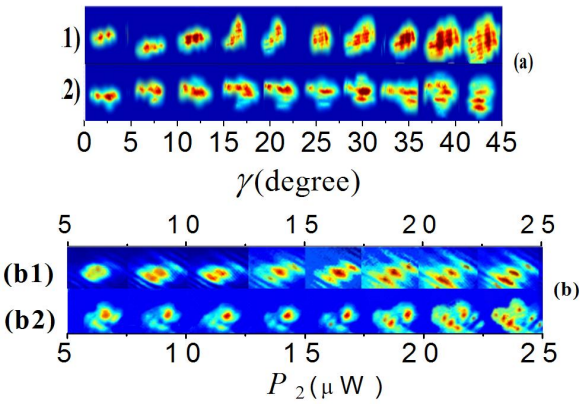

FIG. 31. Omnidirectional Bragg reflections of $\boldsymbol{E}_{\rm F1}$ and $\boldsymbol{E}_{\rm F2}$ beams versus α (a), and $\boldsymbol{E}_{\rm F2}$ beam versus θ_2 (b), the solid curves are calculated results of Bloch wave-vectors $\Re(k_\pm)$. The parameters are $\Delta_1=-15$ GHz , $\Delta_2=-4.5$ GHz, $G_1^{'}=G_1=G_2^{'}=G_2$=20 GHz , and G_3 =0.5 GHz

cross-Kerr nonlinearity in the enhancement case can well compensate the diffraction in the propagation, while it is too weak to balance the diffraction without the enhancement.

Since FWM signal can be modulated by the EIG, the analysis of the PBG of EIG is essential. The spatially modulated total linear and nonlinear refractive index is given by $n(\zeta)=n_0+\delta n_1\cos(2k_2\zeta)+$

$\delta n_2 \cos(4k_2\zeta)$, where n_0 is the spatially uniform refractive index; δn_1 and δn_2 n are the coefficients for spatially varying terms for the modulated index. The width of the band gap is given by $\Delta_{\rm gap} = 2\omega_0(\delta n_1 + \delta n_2)/\pi n_0$, where ω_0 is the center frequency of the forbidden band. Moreover, by coupled mode techniques with Bloch's theorem, we can also get the equation displayed in Part IV. B. 2 (on page 112), with $k_{\rm p} = k_3 \cos\alpha$, and obtain the dispersion curves of $\mathrm{Re}(\kappa_\pm a_i/\pi - 1)$ versus Δ_i ($i = 1, 2$ are for $\boldsymbol{E}_{\rm F1}$ and $\boldsymbol{E}_{\rm F2}$, respectively), as shown in Fig. 31 (a). Here, $\kappa_\pm$ are the Bloch wave-vectors near the Brillouin zone edge, and χ_m & $\chi_m^{'}$ ($m = 1, 2, 3$) are the susceptibility components. Also, with increasing incident angle α of the probe beam $\boldsymbol{E}_3$ from 89.85° to 90°, as shown in Figs. 29 (c) and (d), there exist a series of forbidden bands (the region with $\mathrm{Re}(\kappa_\pm a_i/\pi - 1) \approx 0$ in Fig. 31 (a), with right side for the TE-polarized $\boldsymbol{E}_{\rm F2}$ cases and left side for the TM-polarized $\boldsymbol{E}_{\rm F1}$ cases, respectively) for such induced periodic medium, which result from the strong omnidirectional Bragg reflections. It is obvious that the dipole-mode $\boldsymbol{E}_{\rm F1}$ and $\boldsymbol{E}_{\rm F2}$ soliton beams become weaker (as the stop bands start to disappear from 89.95° to 90° for the incident angle). When the band gap completely disappears at 89.975° (with no zero values for the real dispersion, as shown in the far right and far left dispersion curves)), the residual intensity comes from the FWM signal without the Bragg reflection. In Fig. 31 (b), when the angle θ_2 between the beams $\boldsymbol{E}_2$ and $\boldsymbol{E}_2^{'}$ decreases, the number of spots for the $\boldsymbol{E}_{\rm F2}$ beam changes from eight into two (dipole-mode). The energy has been transferred from those eight spots (at $\theta_2 = 0.5°$) to the dipole-mode spots (at $\theta_2 = 0.2°$). Such dipole soliton is trapped jointly in the neighboring photonic fringes. Since $a_2 = \lambda_2/\theta_2$ the fringe spacing of EIG2 will become larger versus decreasing θ_2.

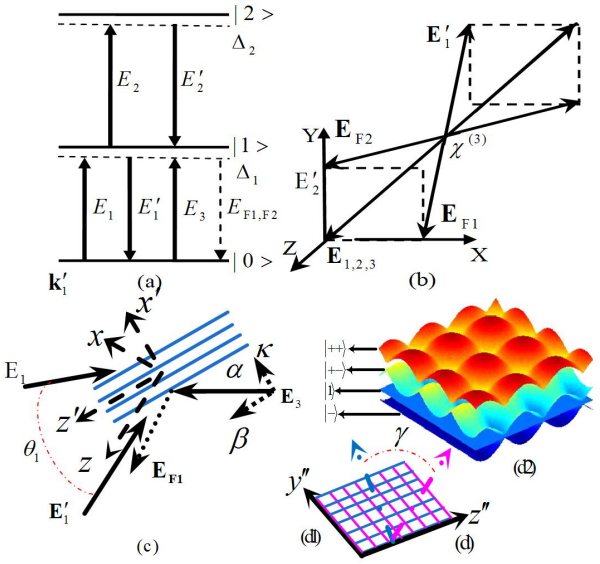

FIG. 32. (a) The ladder-type three-level atomic system (b) The first spatial beam geometric configuration used in the experiment for the investigation of 1-D surface soliton. (c) Generation of FWM1 via Bragg scattering of the probe beam on the EIG1 created by $\boldsymbol{E}_1$ and $\boldsymbol{E}_1^{'}$. (d1) The illustration of the EIL composed of EIG1 and EIG2. (d2) The lattice state

2. Surface Solitons of FWM in EIL

The formation of 1D dipole-mode solitons with FWM beams is introduced in section 1. These composite spatial solitons with orthogonally-oriented dipole components are stable as they propagate inside the atomic medium. In this section, we will discuss the formations of 1D and 2D surface solitons in the EIGs and EIL. Compared with the surface solitons created in the photorefractive crystals and other systems, the ones formed in the atomic medium can be easily controlled by many experimental parameters, such as the probe detuning, the pump powers, and the incident angles of the relevant beams, since the indices in the generated gratings and lattice can be changed by altering the periodically-modulated atomic coherence and nonlinearities[12]. We also investigate the soliton dynamics under the competition between the generation of surface solitons due to the nonlinear localization and the Bragg reflection due to PBG. With the flexible controls in the experimental parameters, we can easily explore various parameter spaces and observe interesting phenomena in forming the 2D surface solitons. These studies will be useful for understanding the fundamental mechanisms in soliton formation and dynamics, and can open new ways to control the diffraction of optical beams and develop new schemes for spatial optical switching[13], pattern formation[14] in optical communication and all-optical image processing.

The spatial periodic modulation of surface soliton is originated from the EIL. In Fig. 32 (b), the two strong pumping beams $\boldsymbol{k}_1$ and $\boldsymbol{k}_1^{'}$ ($\boldsymbol{k}_2$ and $\boldsymbol{k}_2^{'}$) interfere with each other to induce a horizontally aligned grating in X-Z (Y-Z) plane with a period $\Lambda_1 = \lambda_1/2\sin(\theta_1/2)$ ($\Lambda_2 = \lambda_2/2\sin(\theta_2/2)$)[12]. With these gratings, the incident beam can have intense Bragg reflection. The generated FWM signals $\boldsymbol{E}_{\rm F1}$ (TM polarization with respect to EIG1) and $\boldsymbol{E}_{\rm F2}$ (TE polarization with respect to EIG2) are the Bragg reflected signals of the probe beam $\boldsymbol{E}_3$ (launched obliquely into the gratings EIG1 and EIG2), respectively[15]. For instance, as shown in Fig. 32 (c), the incident probe beam has an angle α with respect to the tangential di-

rection of EIG1, which can be decomposed into two components[16]. One component propagates tangentially to the interface between the EIGs and the uniform medium and its propagation characteristics can be represented by the surface wave propagation constant β. The other component propagates in the direction normal to EIGs, which can be characterized by the Bloch wave vector κ. Similar to the Snell's law, the $\boldsymbol{E}_{\rm F1}$ beam (as the Bragg reflected probe beam), is symmetric to the incident probe beam with respect to the normal direction of EIG1, and therefore it is also the syntheses of the tangential surface wave component and the normal Bragg reflected component. The surface-wave component of the probe beam propagates along the $z^{'}$ direction in Fig. 32 (c), parallel to the interface between the EIGs and the uniform medium, while FWM1 propagates along the z axis in Fig. 32 (c). The coordinate's rotation transformation components between these two frames are $\xi^{'} = \xi\cos(\theta_i/2) - z\sin(\theta_i/2)$ and $z^{'} = \xi\sin(\theta_i/2) + z\cos(\theta_i/2)$, where $i = 1$ & $\xi = x$ are for EIG1 and $i = 2$ & $\xi = y$ for EIG2, respectively. Since θ_i is very small, the surface-wave component is the dominant one in the generated FWM signals $\boldsymbol{E}_{\rm F1}$ and $\boldsymbol{E}_{\rm F2}$.

To force the incident probe beam to excite the surface mode and form the surface soliton, we should adjust the Bloch wave vector κ to fall into the forbidden band, so the normal Bragg reflected component is attenuated. When the laser beam propagates at the edge of the EIG and homogeneous medium, the FWM signals can be expressed as: $\boldsymbol{E}^S_{\rm F1,2}(\xi^{'}) = E_\kappa(\xi^{'})\exp[i(\kappa\xi^{'} + \beta z)]$ for $\xi^{'} > 1$ and $\boldsymbol{E}^S_{\rm F1,2}(\xi^{'}) = \alpha\exp(i\beta z + q_\alpha\xi^{'})$ for $\xi^{'} \le 1$, where $\xi^{'}$ represents $x^{'}$ or $y^{'}$, and $\xi^{'} = 1$ defines the boundary of the EIG and homogeneous media. Here, in the forbidden band, there must exist $\kappa = m\pi/\Lambda_i + i\kappa^{'}$ with m being positive integer, in which the nonzero imaginary part $\kappa^{'}$ is the attenuation coefficient along the $\xi^{'}$-axis in the EIGs for the normal Bragg reflected component. Another parameter, $q_\alpha = \sqrt{\beta^2 - [(\omega_i/c)n_\alpha]^2}$ is the attenuation coefficient along the transverse axis in the homogeneous medium, in which n_α is the refractive index ($n_\alpha = n_1 + n_2 I$ with $n_1 \approx 1$). Propagation constant β of the surface wave component can be obtained by solving the equation $m\pi/\Lambda_i + i\kappa^{'} = \cos^{-1}\{{\rm Tr}[T_\Lambda(\beta, \Delta_i)]\}/\Lambda_i$ in the forbidden band, which is derived by the transfer-matrix method and Bloch theorem in medium with periodically modulated refractive index[17], and T_Λ is the transfer matrix of one period in the EIGs. In the Kerr medium, the periodic susceptibility can be expressed by $\chi(\xi) \approx \chi^{(1)}(\xi) + \chi^{(3)}(\xi)|E_2|^2\sin^2(\theta_i/2)$. For one period, the transfer matrix can be expressed by $T_\Lambda(\Delta_1, \beta) = \prod_{j=1}^{N} T_j(\Delta_1, \beta) = [T_{\Lambda 1}(\Delta_1, \beta)T_{\Lambda 2}(\Delta_1, \beta)]^T$, $T_{\Lambda 1}(\Delta_1, \beta) = [T_{\Lambda 11}(\Delta_1, \beta)T_{\Lambda_{12}}(\Delta_1, \beta)]$, and $T_{\Lambda 2}(\Delta_1, \beta) = [T_{\Lambda 21}(\Delta_1, \beta)T_{\Lambda_{22}}(\Delta_1, \beta)]$, where T_j is the transfer matrix of the j-th layer when we divide the whole period into N layers, and the dependencies on the frequency (Δ_1) and propagation constant β are obvious.

The two EIGs are in different planes, so the interaction region between them is small and they can be considered to be isolated. The experimental results presented are obtained under such condition. The experimental configuration can also be changed to have a second configuration in which EIG1 and EIG2 are both in the Y-Z plane and the orientations of them are deviated from Z axis by 22.5°, anticlockwise and clockwise respectively, defined as $y^{''}$ and $z^{''}$. In this case, the two EIGs have considerable overlapping area to construct a 2D EIL with a 2D periodic refractive index due to periodically modulated atomic coherence. Specifically, the level splitting due to the dressing by the strong pump beams can significantly affect the susceptibility and further modify the refractive index[18]. At the position where the antinodes of the standing wave created by fields $\boldsymbol{E}_1$ and $\boldsymbol{E}_1^{'}$ come across that of the standing wave created by $\boldsymbol{E}_2$ and $\boldsymbol{E}_2^{'}$, the naked level $|1\rangle$ will be split into three dressed levels $|++\rangle$, $|+-\rangle$ and $|-\rangle$ after being doubly dressed by $\boldsymbol{E}_1$ & $\boldsymbol{E}_1^{'}$ and $\boldsymbol{E}_2$ & $\boldsymbol{E}_2^{'}$, as shown in Fig. 32 (d1), so the refractive index is strongly modified by these two field pairs[12]. In contrast, at the position where the nodes of the two standing waves overlap, level $|1\rangle$ is not dressed and the index will not be modified. When the antinodes of one standing wave encounter the nodes of the another standing wave, level $|1\rangle$ will be split into two dressed levels $|+\rangle$ and $|-\rangle$ and the index will be modified only by a single field pair. The spatial periodical distribution of these three cases can lead to a lattice state as shown in Fig. 32 (d2) and further distinguished 2D periodic index modulation as illustrated in Fig. 32 (d1). The sensitivity of such index modulation to the detuning of the probe field and powers of the dressing fields leads to the tunability for the soliton formation by multi-parameters.

The propagations of FWM1 and FWM2 under either 1D or 2D modulations and diffraction can be expressed by

$$\frac{\partial E_{\rm F1}}{\partial z} - \frac{i\nabla_T^2 E_{\rm F1}}{2k_{\rm F1}} = \frac{ik_{\rm F1}}{n_1}\left\{n_2^{S1}|E_{\rm F1}|^2 + 2\left[n_2^{X1}|E_1^{'}|^2[\varsigma\mu(z^{''}) + (1-\varsigma)\mu(x^{'}) + \varsigma n_2^{X2}|E_2^{'}|^2\mu(y^{''})\right]\right\}E_{\rm F1} \quad (26\text{-}1)$$

$$\frac{\partial E_{\rm F2}}{\partial z}-\frac{i\nabla_T^2 E_{\rm F2}}{2k_{\rm F2}}=\frac{ik_{\rm F2}}{n_1}\left\{n_2^{S2}|E_{\rm F2}|^2+2\left[n_2^{X3}|E_1^{'}|^2\varsigma\mu(z^{''})+n_2^{X4}|E_2^{'}|^2[\varsigma\mu(y^{''})+(1-\varsigma)\mu(y^{'})]\right]\right\}E_{\rm F2} \quad (26\text{-}2)$$

where ∇_T^2 is the Laplace operator with respect to the x and y axes and describes the diffraction. The y'' and z'' axes denote the orientations of EIG1 and EIG2, respectively. In these equations, $\mu(\xi)=\cos^2(\pi\xi/\Lambda_i)$ for $\xi\geq 1$ and $\mu(\xi)=1$ for $\xi<1$ ($\xi=x',y',y'',z''$) represent the periodically modulated refractive index pattern inside the EIGs ($\xi\geq 1$) and the uniform index outside ($\xi<1$) the EIGs ($\xi=x',y''$ for EIG1 and $\xi=y',z''$ for EIG2), respectively. Surface solitons can be generated at the interface of these two regions with a high refractive index contrast. The factor $\varsigma=0$ or 1 is introduced to describe the assembling of EIG1 and EIG2 into EIL, i.e. $\varsigma=1$ for sufficiently large overlapping area as in Fig. 32 (d), and $t\varsigma=0$ when overlapping area is not sufficiently large as in Fig. 32 (b). With $\varsigma=1$ both FWM signals suffer from the modulations of the lattice with the indices varying periodically in two directions according to $\mu(y'')$ and $\mu(z'')$. In Eq. (26-2), n_1 is the linear refractive index at ω_1; $n_2^{S1,2}$ are the self-Kerr coefficients of $\boldsymbol{E}_{\rm F1}$ and $\boldsymbol{E}_{\rm F2}$, and n_2^{X1-X4} are the cross-Kerr coefficients from and $\boldsymbol{E}_{1,2}$ and $\boldsymbol{E}_{1,2}^{'}$ respectively. These Kerr nonlinear coefficients can all be calculated by the general expression $n_2=\mathrm{Re}\chi^{(3)}/(\epsilon_0 c n_1)$.

A qualitative analysis of the Eq. (26-2) is available when the diffraction and SPM terms are neglected, in which the phase profile distortion of FWM by the EIL or EIG is considered[19]. This will allow the linearization of Eq. (26-2) with respect to x and y, and obtain a set of solutions with phases for $\boldsymbol{E}_{\rm F1}$ and $\boldsymbol{E}_{\rm F2}$ as $\phi_{\rm F1}=2k_{\rm F1}\{n_2^{X1}|E_1^{'}|^2[\varsigma\mu(y'')+(1-\varsigma)\mu(x')]+n_2^{X4}|E_2^{'}|^2\varsigma\mu(z'')\}z/n_1$ and $\phi_{F2}=2k_{\rm F2}\{n_2^{X3}|E_2^{'}|^2\varsigma\mu(z'')+n_2^{X4}|E_1^{'}|^2[\varsigma\mu(y'')+(1-\varsigma)\mu(y)]\}z/n_1$, both of which is 2D (1D) periodic at $\varsigma=1$ ($\varsigma=0$). The curvature of such distorted phase front is periodically alternative to be positive and negative, so the FWM signal is 2D or 1D periodically modulated. We also can obtain the modulation periodic of FWM signal: FWM1 (FWM2) has period $\Lambda_{\rm F1,F2}^{x',y'}=n_1\Lambda_1^2/k_{\rm F1,F2}\pi|E_{1,2}^{'}|^2 n_2^{X1,X4}z$ along x' (y') axis at $\varsigma=0$, and $\Lambda_{\rm F1,F2}^{y''}=n_1\Lambda_1^2/k_{\rm F1,F2}\pi|E_1^{'}|^2 n_2^{X1,X3}z$ and $\Lambda_{\rm F1,F2}^{z''}=n_1\Lambda_1^2/k_{\rm F1,F2}\pi|E_2^{'}|^2 n_2^{X2,X3}z$ along y'' and z'' axis at $\varsigma=1$.

In Ref. [20], one can find the details of 1D surface soliton, here we will focus on the 2D surface soliton. After adjusting the parameters such as frequency detuning, power set at their optimal values, sufficient intersection area becomes essential for the formation of the lattice state and EIL illustrated in Figs. 32 (d2) and (d1), and the generation of 2D surface solitons propagating along the corner of this EIL, so the beam configuration is reconstructed. In this reconstruction, the orientations EIG1 (EIG2) are anticlockwise (clockwise) rotated in the Y-Z plane. We define γ as the angle between the orientations of the two EIGs and the maximum is 45°. The images of FWM1 are recorded at ten discrete positions in the rotation process of EIG1, as shown in Figs. 33 (a1) and (a2). FWM1 in Fig. 33 (a1) only shows modulation in y''-direction due to the small intersection area when EIG2 is not rotated, though the rotation of EIG1 increases the area on a certain extent. In contrast, in Fig. 33 (a2), there are periodic modulations of FWM1 in two directions, which become increasingly significant with increasing γ, because the intersection area has been gradually enlarged and the area with lattice state gradually extends.

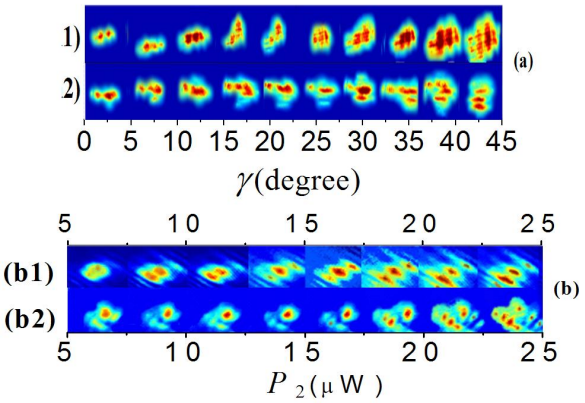

FIG. 33. (a) The images of the FWM1 signal when EIG1 is rotated by ten discrete angles with EIG2 not rotated in (a1) and rotated in (a2). (b) The images of FWM1 signal (b1) when the power P_1 of the pump beam $\boldsymbol{E}_1^{'}$ is successively set at eight discrete values (6 μW, 8 μW, 10 μW, 12 μW, 14 μW, 16 μW, 18 μW and 20 μW) with EIG1 rotated and EIG2 not rotated, respectively; (b2) the images of the FWM1 signal when the power of $\boldsymbol{E}_2^{'}$ changes as that of $\boldsymbol{E}_1^{'}$ in (b1) and the power of $\boldsymbol{E}_1^{'}$ is fixed at 10 μW, with EIG1 rotated and EIG2 both rotated

Next, the evolution of the FWM1 solitons is investigated when the pump fields $\boldsymbol{E}_1^{'}$ and $\boldsymbol{E}_2^{'}$ are changed, respectively. In Fig. 33 (b1), EIG1 is rotated to have large γ, while EIG2 is not rotated. Thus, one can easily see that the FWM signal remains periodically modulated in y''-direction. Here, increasing P_1 only has the effect of decreasing the modulation period. In Fig. 33 (b2), EIG2 is rotated, and therefore the 2D

modulation of FWM1 is formed. When the power of $\boldsymbol{E}_2^{'}$ increases, the periodic stripes in one direction of such 2D modulations become denser. Such tunability can be well explained by the expression $\Lambda_{\mathrm{F1}}^{y_2''} = n_1\Lambda_1^2/k_{\mathrm{F1}}\pi|E_2^{'}|^2 n_2^{X2} z$ in which larger P_2 will lead to a smaller modulation period and it further verifies that the 2D EIL is composed of two tunable EIGs with different spatial orientations.

In summary, we have discussed the formation and dynamics of the 2D surface solitons in FWM signals in the atomic medium. Such surface solitons propagate along the interface between the uniform medium and the EIL, which is composed of two EIGs. Such investigation will be important in understanding the fundamental mechanisms in soliton formation and dynamics. It also open new ways to flexibly control the diffraction of optical beams and designing new devices for optical image storage, processing and communication.

V. QUANTUM CONTROL OF MWM

A. Fluorescence in MWM

Traditional fluorescence is defined as emitted light by an object which usually has a longer wavelength than the absorbed radiation. However, in the case that there are two photons absorbed by one atom, the emission with wavelength shorter than the photon absorbed can be obtained. Furthermore, the emitted field may also be of the same wavelength as the absorbed radiation, termed "resonance fluorescence". FWM process is often accompanied by single-photon, two-photon and three-photon fluorescence processes, which can be also affected by dressing effect.

1. Two- and Three-Photon Fluorescencesf accompanying with FWM

This section provides a brief description of two-photon fluorescence process which is accompanied with the MWM process. In our theoretical and experimental scheme, both MWM and fluorescence signals are transmitted in EIT window. Therefore, compared with resonance fluorescence, the fluorescence process with MWM has several distinct differences and advantages. First, extremely narrow fluorescence signals (about 50 MHz) can be obtained in an open-cycle atomic system, since the generated fluorescence signals fall into EIT windows. Such fluorescence signals with extremely narrow linewidths have not been reported before, either experimentally or theoretically. This will allow us to investigate the quantum correlation and narrow linewidth laser since the generated fluorescence signal is of very high in coherence and monochromaticity. Second, by individually controlling the EIT windows, fluorescence signals can be clearly separated or superimposed selectively. Third, the amplitude of the fluorescence signal can be controlled by changing the intensity and frequency of pumping laser via Dark states.

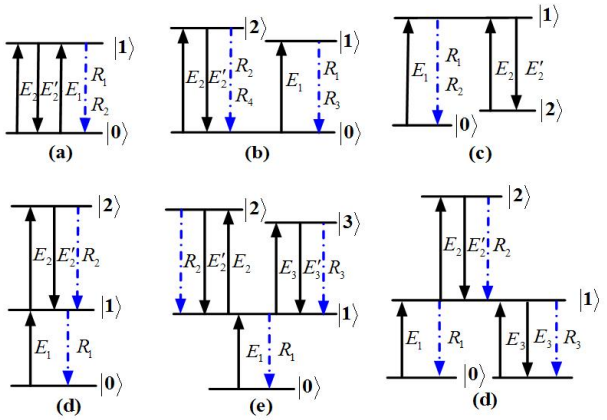

FIG. 34. The diagrams of (a) two-level, (b) a three-level V-type, (c) a three-level Λ-type, (d) a three-level Ξ-type, and (e) four-level Y-type atomic systems, respectively

In order to give a clear physical description of the fluorescence process, we consider six kinds of atomic level structures, two-level, three level V-, Λ-, and Ξ-type, four-level Y- and inverted Y-type atomic systems, as shown in Fig. 34. First, for two-level system (Fig. 34 (a)), the single- and two-photon fluorescence signals R_1 and R_2 will be generated due to spontaneous emission of photons from $|1\rangle$ to $|0\rangle$, which can be described by the Liouville pathways (R_1) $\rho_{00}^{(0)} \xrightarrow{\omega_1} \rho_{10}^{(1)} \xrightarrow{-\omega_1} \rho_{11}^{(2)}$ and (R_2) $\rho_{00}^{(0)} \xrightarrow{\omega_1} \rho_{10}^{(1)} \xrightarrow{-\omega_2} \rho_{00}^{(2)} \xrightarrow{\omega_2} \rho_{10}^{(3)} \xrightarrow{-\omega_1} \rho_{11}^{(4)}$, respectively. Next, for the three-level V-type system (Fig. 34 (b)), there exist two single-photon fluorescence signals R_1 (from $|1\rangle$ to $|0\rangle$) and R_2 (from $|2\rangle$ to $|0\rangle$), and two two-photon fluorescence signals R_3 (from $|1\rangle$ to $|0\rangle$) and R_4 (from $|2\rangle$ to $|0\rangle$), which can be described by the Liouville pathways (R_1) $\rho_{00}^{(0)} \xrightarrow{\omega_1} \rho_{10}^{(1)} \xrightarrow{-\omega_1} \rho_{11}^{(2)}$, ($R_2$) $\rho_{00}^{(0)} \xrightarrow{\omega_2} \rho_{20}^{(1)} \xrightarrow{-\omega_2} \rho_{22}^{(2)}$, ($R_3$) $\rho_{00}^{(0)} \xrightarrow{\omega_1} \rho_{10}^{(1)} \xrightarrow{-\omega_2} \rho_{12}^{(2)} \xrightarrow{\omega_2} \rho_{10}^{(3)} \xrightarrow{-\omega_1} \rho_{11}^{(4)}$ and (R_4) $\rho_{00}^{(0)} \xrightarrow{\omega_2} \rho_{20}^{(1)} \xrightarrow{-\omega_1} \rho_{21}^{(2)} \xrightarrow{\omega_1} \rho_{20}^{(3)} \xrightarrow{-\omega_2} \rho_{22}^{(4)}$. Then, for the three-level Λ-type system (Fig. 34 (c)), the decay of photons from $|1\rangle$ to $|0\rangle$ will generate single- and two-photon fluorescence signals R_1 and R_2, which can be described via the Liouville pathways (R_1) $\rho_{00}^{(0)} \xrightarrow{\omega_1} \rho_{10}^{(1)} \xrightarrow{-\omega_1} \rho_{11}^{(2)}$ and (R_2) $\rho_{00}^{(0)} \xrightarrow{\omega_1} \rho_{10}^{(1)} \xrightarrow{-\omega_2} \rho_{20}^{(2)} \xrightarrow{\omega_2} \rho_{10}^{(3)} \xrightarrow{-\omega_1} \rho_{11}^{(4)}$, respectively. While for the Ξ-type system (Fig. 34 (d)), there is only one single-photon and one two-photon fluorescence signals R_1 and R_2, which can be

represented by the Liouville pathways (R_1) $\rho_{00}^{(0)} \xrightarrow{\omega_1} \rho_{10}^{(1)} \xrightarrow{-\omega_1} \rho_{11}^{(2)}$ (spontaneous emission from $|1\rangle$ to $|0\rangle$) and (R_2) $\rho_{00}^{(0)} \xrightarrow{\omega_1} \rho_{10}^{(1)} \xrightarrow{\omega_2} \rho_{20}^{(2)} \xrightarrow{-\omega_1} \rho_{21}^{(3)} \xrightarrow{-\omega_2} \rho_{22}^{(4)}$ (spontaneous emission from $|2\rangle$ to $|1\rangle$), respectively. Further, for the four-level Y-type system (Fig. 34 (e)), there is additional two-photon fluorescence signal R_3 compared to the three-level Ξ-type system (Fig. 34 (d)), which is the spontaneous emission form $|3\rangle$ to $|1\rangle$), and can be expressed by the Liouville pathway (R_3) $\rho_{00}^{(0)} \xrightarrow{\omega_1} \rho_{10}^{(1)} \xrightarrow{\omega_3} \rho_{30}^{(2)} \xrightarrow{-\omega_1} \rho_{31}^{(3)} \xrightarrow{-\omega_3} \rho_{33}^{(4)}$. Here, we only give the corresponding doubly dressed density matrix elements for the four-level Y-type system as follows:

$$\rho_{11}^{(2)} = -|G_1|^2/[\Gamma_{11}(d_1 + |G_2|^2/d_2 + |G_3|^2/d_3)] \tag{27}$$

$$\rho_{22}^{(4)} = |G_1|^2|G_2|^2/[\Gamma_{22}d_1d_4(d_2 + |G_2|^2/(d_1 + |G_3|^2/d_3))] \tag{28}$$

$$\rho_{33}^{(4)} = |G_1|^2|G_3|^2/[\Gamma_{33}d_1d_5(d_3 + |G_3|^2/(d_1 + |G_2|^2/d_2))] \tag{29}$$

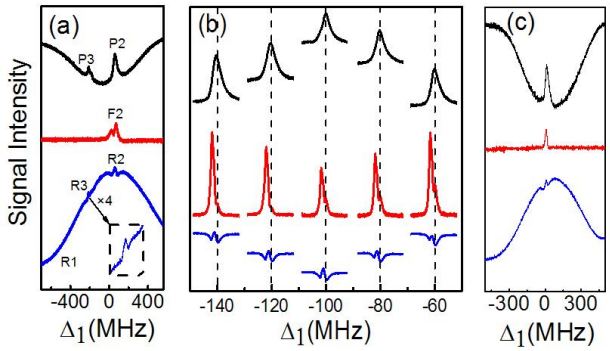

FIG. 35. Measured probe transmission (upper curves), MWM (middle curves) and fluorescence (bottom curves) ((a) and (c)) versus Δ_1, (b) versus Δ_2 at discrete Δ_1 in four-level Y-type ((a) and (b)) and inverted Y-type (c) atomic system

where $d_1 = \Gamma_{10} + i\Delta_1$, $d_2 = \Gamma_{20} + i(\Delta_1 + \Delta_2)$, $d_3 = \Gamma_{30} + i(\Delta_1 + \Delta_2)$, $d_4 = \Gamma_{21} + i\Delta_2$ and $d_5 = \Gamma_{31} + i\Delta_3$. Finally, the four-level inverted Y-type system (Fig. 34 (f)), will also generate an additional two-photon fluorescence signal R_3 compared with Ξ-type system, which can be presented as (R_3) $\rho_{00}^{(0)} \xrightarrow{\omega_1} \rho_{10}^{(1)} \xrightarrow{-\omega_3} \rho_{30}^{(2)} \xrightarrow{\omega_3} \rho_{10}^{(3)} \xrightarrow{-\omega_1} \rho_{11}^{(4)}$ (spontaneous emission from $|1\rangle$ to $|0\rangle$).

With Δ_1 scanned, the probe transmission, FWM and fluorescence signals (Fig. 35 (a)) in Y-type system are obtained. In the fluorescence signals, the big background represents the single-photon fluorescence R_1 $(\rho_{11}^{(2)})$, and the other two small sharp peaks on it are the two-photon fluorescence R_2 $(\rho_{22}^{(4)})$ and R_3 $(\rho_{33}^{(4)})$. And Fig. 35 (b) represents the measured signals by scanning Δ_2 at discrete Δ_1 . Similarly, for the fluorescence signal, the profile expresses the dressed R_1 $(\rho_{11}^{(2)})$ by $\boldsymbol{E}_3$, the dip lower than the corresponding baseline represents further dressed R_1 $(\rho_{11}^{(2)})$ by $\boldsymbol{E}_2$, and the peak within the dip is the two-photon fluorescence signal R_2 $(\rho_{22}^{(4)})$. Furthermore, Fig. 35 (c) represents the probe transmission, SWM and fluorescence versus Δ_1 in inverted Y-type system. Same as before, the big background represents the fluorescence R_1 and R_3 ($\rho_{11}^{(2)}$ and $\rho_{11}^{(4)}$), and the small sharp peak on it is the two-photon fluorescence R_2 $(\rho_{22}^{(4)})$.

The difference between two-photon fluorescence and the FWM signals can be seen from Liouville pathway. First, the FWM signal is caused by the atomic coherence effect while the fluorescence signal is induced by spontaneous decay of photons pumped to the upper levels. Then, the direction of FWM the signal is determined due to the limitations of the phase-matching conditions but the fluorescence signal is not. Third, FWM process follows the closed-loop path while the fluorescence process does not. The extremely narrow fluorescence signal with very high coherence and monochromaticity introduced here can be used for the quantum correlation and narrow linewidth laser.

2. Opening Fluorescence and FWM via Dual EIT Windows

In this Section, we compare the probe transmission, FWM and fluorescence signals under dressing effects. The ultra-narrow two-photon fluorescence signal, which is sheared twice by EIT window, is obtained in ladder or Y-type atomic system. Such fluorescence with very high coherence and monochromaticity can be potentially applied in metrology, long-distance quantum communication and quantum correlation. Also, we investigate the interaction effect between two ladder subsystems on the measured signals. Moreover, the amplitude of the signals can be effectively controlled by the incident beam intensity and frequency detuning.

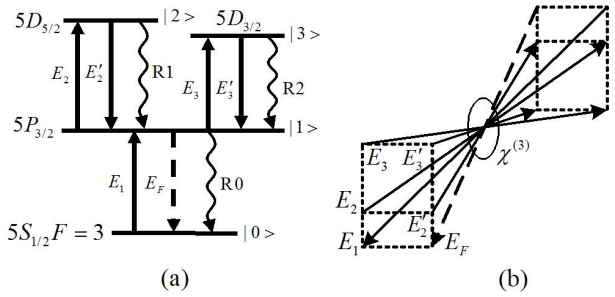

FIG. 36. (a) Relevant ^{85}Rb four-level Y-type atomic system. (b) Spatial beam geometry used in the experiment

Three types of fluorescence due to spontaneous emission are detected that the decay of photons from $|1\rangle$ to $|0\rangle$ will generate single-photon fluorescence signal R0 (wavelength 780 nm), and the decay of photons from $|2\rangle$ and $|3\rangle$ to $|1\rangle$ will generate two-photon fluorescence signals R1 and R2 (wavelength 776 nm), as shown in Fig. 36 (a). Compared with FWM, the fluorescence signals are non-directional and detected by another photodiode. The two-photon fluorescence signals can also fall into the EIT windows and form the Doppler-free sharp peaks.

As described in the Section 1, for the fluorescence signals, the single-photon fluorescence R0 is described by $\rho_{00}^{(0)} \xrightarrow{E_1} \rho_{10}^{(1)} \xrightarrow{(E_1)^*} \rho_{11}^{(2)}$. By solving the coupled density-matrix equations, the expression of the density-matrix element $\rho_{11}^{(2)}$ can be obtained as $\rho_{11}^{(2)} = -|G_1|^2/(d_1\Gamma_{11})$, the amplitude square of which is proportional to the intensity of R0. When the beams $\boldsymbol{E}_2$ and $\boldsymbol{E}_3$ are turned on, the fluorescence process R0 can be doubly dressed, and the expression of $\rho_{11}^{(2)}$ should be modified as $\rho_{11DD}^{(2)} = -|G_1|^2/[\Gamma_{11}(d_1 + |G_2|^2/d_2 + |G_3|^2/d_3)]$. For two-photon fluorescence R1, via Liouville pathway $\rho_{00}^{(0)} \xrightarrow{E_1} \rho_{10}^{(1)} \xrightarrow{E_2} \rho_{20}^{(2)} \xrightarrow{(E_1)^*} \rho_{21}^{(3)} \xrightarrow{(E_2)^*} \rho_{22}^{(4)}$ we can obtain the density-matrix element $\rho_{22}^{(4)}$ as $\rho_{22}^{(4)} = |G_1|^2|G_2|^2/(\Gamma_{22}d_1d_2d_4)$, the amplitude square of which is proportional to the intensity of R1. Considering the self-dressing effect of $\boldsymbol{E}_2$ and $\boldsymbol{E}_2'$, the expression of $\rho_{22}^{(4)}$ should be modified as $\rho_{22SD}^{(4)} = |G_1|^2|G_2|^2/[\Gamma_{22}d_1d_4(d_2 + |G_2|^2/d_1)]$. When $\boldsymbol{E}_3$ the beam is turned on, its dressing effect should be additionally considered and the doubly dressed fluorescence process R1 is given as $\rho_{22DD}^{(4)} = |G_1|^2|G_2|^2/[\Gamma_{22}d_1d_4(d_2 + |G_2|^2/(d_1 + |G_3|^2/d_3))]$. Correspondingly, the fluorescence signal R2 is related with the density-matrix element $\rho_{33}^{(4)} = |G_1|^2|G_3|^2/(\Gamma_{33}d_1d_3d_5)$. Similarly with R1, the singly dressed R2 process is given as $\rho_{33SD}^{(4)} = |G_1|^2|G_3|^2/[\Gamma_{33}d_1d_5(d_3 + |G_3|^2/d_1)]$. and doubly dressed R2 process is given as $\rho_{33DD}^{(4)} = |G_1|^2|G_3|^2/[\Gamma_{33}d_1d_5(d_3 + |G_3|^2/(d_1 + |G_2|^2/d_2))]$.

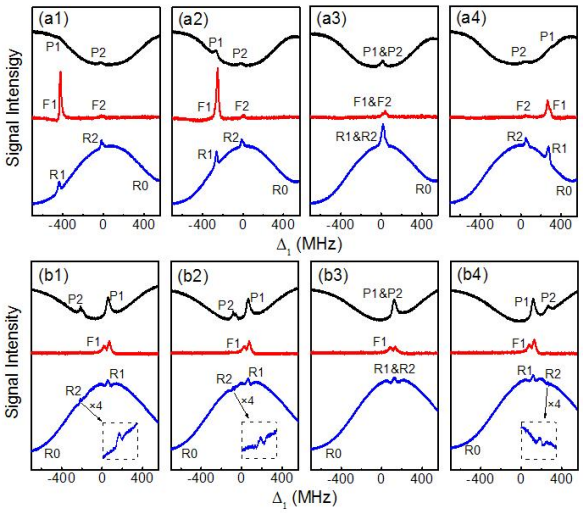

FIG. 37. Measured probe transmission (the upper curves), FWM (the middle curves) and fluorescence (the bottom curves) versus Δ_1. (a) $P_1 = 1$ mW and Δ_2 set as (a1) 400 MHz, (a2) 250 MHz, (a3) 0 and (a4) -250 MHz, respectively, with $\Delta_3 = 0$; (b) $P_1 = 6$ mW and Δ_3 set as (b1) 250 MHz, (b2) 100 MHz, (b3) -100 MHz and (b4) -250 MHz, respectively, with $\Delta_2 = -100$ MHz and $\boldsymbol{E}_3'$ blocked. The other experimental parameters are $P_2 = 12$ mW, $P_2' = 8$ mW, $P_3 = 22$ mW, $P_3' = 16$ mW

Figure 37 presents the measured FWM and fluorescence signals via the EIT windows versus Δ_1. First, with all five beams on and $P_1 = 1$ mW, the measured curves under different Δ_2 are depicted in Figs. 37 (a1)$\sim$(a4). In the probe transmission, two EIT windows arise at $\Delta_1 = -\Delta_2$ and $\Delta_1 = -\Delta_3$ (labeled as P1 and P2) within the Doppler absorption background. The FWM signals F1 and F2 fall into the two EIT windows respectively. As Δ_2 changes, the EIT window P1 and FWM signal F1 shift from left to right, and overlap with the fixed EIT window P2 and FWM signal F2 at $\Delta_2 = \Delta_3 = 0$ (Fig. 37 (a3)). For the fluorescence signals, the big background curve represents the single-photon fluorescence R0 ($\rho_{11}^{(2)}$). The other two small sharp peaks on it are the two-photon fluorescence R1 ($\rho_{22}^{(4)}$) and R2 ($\rho_{33}^{(4)}$) falling into the EIT windows. The intensity of fluorescence R1 reaches its maximum at the resonant point ($\Delta_2 = 0$, Fig. 37 (a3)) and decreases gradually as Δ_2 is set farther from resonance (from Fig. 37 (a3) to 2(a1)), due to the effect of single-photon term d_1 and d_4 in $\rho_{22}^{(4)}$. Next, when P_1 increases to 6 mW, the dressed signals are shown in Figs. 37 (b1)$\sim$(b4) where $\boldsymbol{E}_3'$ is blocked. Here, the FWM signal F2 disappears due to the absence of $\boldsymbol{E}_3'$ and the fixed FWM signal F1 shows AT splitting from the self-dressing effect of $\boldsymbol{E}_2$ ($\boldsymbol{E}_2'$), denoting by the dressing term $|G_2|^2/d_2$ in

$\rho^{(3)}_{F1DD}$. When the EIT windows P1 and P2 overlap in Fig. 37 (b3), F1 is suppressed obviously due to the dressing effect of $\boldsymbol{E}_3$ denoting by the dressing term $|G_3|^2/d_3$. In the fluorescence signals, two suppression dips lower than the background curve containing sharp peaks R1 and R2 can be observed. These suppression dips are induced by the dressing effects of $\boldsymbol{E}_2$ ($\boldsymbol{E}_2^{'}$) and $\boldsymbol{E}_3$ individually, described by the terms $|G_2|^2/d_2$ and $|G_3|^2/d_3$ in $\rho^{(2)}_{11DD}$. Such dressing effects can be modulated by $\boldsymbol{E}_1$ according to $\rho^{(2)}_{11DD}$, therefore when P_1 is small (Fig. 37 (a)) the dips are invisible. When Δ_3 moved far from resonance, the dip at $\Delta_1 = -\Delta_3$ gradually becomes shallower, corresponding with the weakened EIT. On the other hand, the R2 peak gets slightly higher with Δ_3 increasing (from Fig. 37 (b2) to 2(b1)), which is entirely different from the case in Fig. 37 (a) where R1 peak weakens with Δ_2 increasing. This is for the reason that as the power of $\boldsymbol{E}_1$ increases, its dressing effect on the two-photon term d_3 in $\rho^{(4)}_{33}$ should be considered, expressed as $d_3+|G_1|^2/d_3$. Hence the fluorescence peaks R1 and R2 are suppressed around the resonant point. More importantly, the fluorescence peak R2 within the dip can be seen with ultra-narrow linewidth (about 10 MHz), which is much narrower than the EIT windows (about 50 MHz). Such high-resolution fluorescence is generated because it has been sheared twice by the EIT window P2. First, due to the two-photon dressing term $|G_3|^2/d_3$, the single-photon term d_1 of $\rho^{(2)}_{11}$ is clipped out, resulting in the suppression dip on R0, which is of the same width as the EIT window P2. Further, such clipped single-photon term, as a factor of two-photon term d_2, participates in the process of two-photon fluorescence R2 ($\rho^{(4)}_{33}$) which also stays in the EIT window P2. Therefore, the fluorescence is sheared for the second time to an ultra-narrow peak. Similarly, in the $|0\rangle - |1\rangle - |2\rangle$ subsystem the fluorescence R1 can be also sheared twice by the EIT window P1 and therefore with ultra-narrow linewidth.

In the following, we observe the dressing effects and the interplay between two ladder subsystems by scanning Δ_2. When $\boldsymbol{E}_1$, $\boldsymbol{E}_2$ and $\boldsymbol{E}_2^{'}$ are turned on, we first study the singly dressed signals in $|0\rangle - |1\rangle - |2\rangle$ subsystem, as depicted in Figs. 38 (a1)∼3(a3) with different Δ_1. In the probe transmission signals, the heights of baselines (horizontal background) represent the Doppler absorption background at corresponding Δ_1. EIT peaks higher than baselines appear at $\Delta_1+\Delta_2=0$, EIA dips lower than baselines satisfying $\Delta_1+\Delta_2 = |G_2|^2/\Delta_1$ can be observed at large detuning (Figs. 38 (a1) and (a3)). The FWM signal F1 with double-peak structure can be observed in Fig. 38 (a2) due to the synthesis of the self-dressing effect and the two-photon emission feature. Such double-peak structure becomes unobvious in Figs. 38 (a1) and

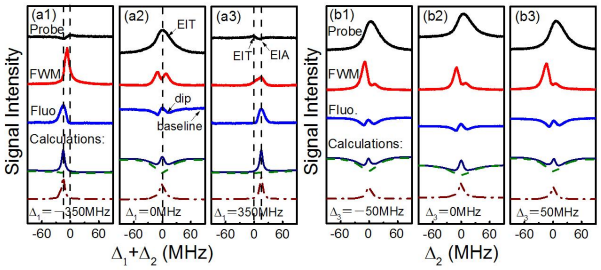

FIG. 38. Measured probe transmission, FWM and fluorescence versus Δ_2 with (a) $\boldsymbol{E}_3$ and $\boldsymbol{E}_3^{'}$ blocked and Δ_1 set as (a1) −350 MHz, (a2) 0 MHz and (a3) 350 MHz; (b) $\boldsymbol{E}_3^{'}$ blocked and Δ_3 set as (b1) −50 MHz, (b2) 0 MHz and (b3) 50 MHz with fixed $\Delta_1 = 0$. The other parameters are $P_1 = 4$ mW, $P_2 = 14$ mW, $P_2^{'} = 7$ mW, $P_3 = 25$ mW. The calculations of fluorescence are presented below the measured curves. Especially, the dash lines represent the calculated R0 and the dash-dot lines represent the calculated R1

(a3), since the dressing effect weakens at the large frequency detuning. For the detected fluorescence signal, the baselines with suppression dips represent fluorescence R0, and the peaks within the dips are fluorescence R1. With Δ_1 set far from resonance, the dip gradually becomes shallower, and eventually almost invisible at large detuning (Figs. 38 (a1) and (a3)), as corresponds to the weakening process of EIT. On the contrary, the peak gets stronger with Δ_1 increasing, for R1 is suppressed around the resonant point according to the dressed term $d_2+|G_2|^2/d_1$ in $\rho^{(4)}_{22SD}$. Moreover, the suppression dips just fall into the EIT windows satisfying $\Delta_1+\Delta_2=0$, and fluorescence peaks at large detuning are in alignment with EIA satisfying $\Delta_1+\Delta_2 = |G_2|^2/\Delta_1$. In order to demonstrate the phenomena more clearly, we present the corresponding calculations of fluorescence signals below the experimental curves. Especially, the calculated R0 (the dash lines) and R1 (the dash-dot lines) are displayed separately. Such theoretical calculations confirm our experimental analysis stated above.

When $\boldsymbol{E}_3$ is also turned on, the $|0\rangle - |1\rangle - |2\rangle$ and $|0\rangle - |1\rangle - |3\rangle$ subsystems will interplay with each other, resulting in some interesting phenomena as shown in Figs. 38 (b1)∼(b3). In the probe transmission, the profile of baselines reveals the EIT induced by $\boldsymbol{E}_3$ at $\Delta_3 = -\Delta_1 = 0$ and the peaks over each baseline are EIT induced by $\boldsymbol{E}_2$ ($\boldsymbol{E}_2^{'}$). It is obvious that the EIT induced by $\boldsymbol{E}_2$ ($\boldsymbol{E}_2^{'}$) is smaller at $\Delta_3 = 0$ (Fig. 38 (b2)) than Δ_3 is detuned (Fig. 38 (b1) and (b3)). This is the result of the strong cascade-dressing interaction between $\boldsymbol{E}_2$ ($\boldsymbol{E}_2^{'}$) and $\boldsymbol{E}_3$ near $\Delta_1 = 0$ according to the doubly dressed element $\rho^{(1)}_{10DD} = iG_1/(d_1+|G_2|^2/d_2+|G_3|^2/d_3)$. The FWM signal F1 shows double-peak structure induced by $\boldsymbol{E}_2$

($\boldsymbol{E}_2^{'}$), and is additionally suppressed by external dressing field $\boldsymbol{E}_3$ when $\Delta_3 = -\Delta_1$ (Fig. 38 (b2)). The fluorescence R0 is also suppressed by $\boldsymbol{E}_3$ as depicted by the lower fluorescence baseline in Fig. 38 (b2), in addition to suppression effect of $\boldsymbol{E}_2(\boldsymbol{E}_2^{'})$. Corresponding to the EIT window, the suppression dip induced by $\boldsymbol{E}_2(\boldsymbol{E}_2^{'})$ is shallower at $\Delta_3 = 0$ (Fig. 38 (b2)) than Δ_3 is detuned (Figs. 38 (b1) and (b3)). On the other hand, the fluorescence peak R1 in Fig. 38 (b2) is slightly stronger than the ones in Figs. 38 (b1) and (b3), resulting from the enhancement effect of $\boldsymbol{E}_3$ around $\Delta_3 = -\Delta_1$ by considering the nest-dressing term $|G_2|^2/(d_1+|G_3|^2/d_3)$ in $\rho_{22DD}^{(4)}$. The corresponding calculations of fluorescence are also presented in Fig. 38 (b), which are in agreement with the experimental results.

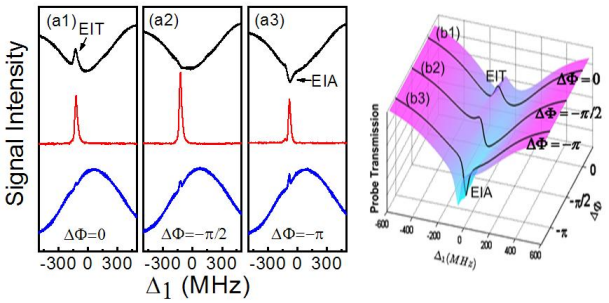

FIG. 39. (a) Transmitted probe (top curves), FWM (middle curves) and fluorescence (bottom curves) signals versus Δ_1 with $\boldsymbol{E}_3$ and $\boldsymbol{E}_3^{'}$ blocked and $\Delta_2 = 100$ MHz for different $\Delta\Phi$: (a1) 0, (a2) $-\pi/2$, (a3) $-\pi$. Powers of participated laser beams are $P_1 = 7$ mW, $P_2 = 17$ mW and $P_2^{'} = 8$ mW. (b1)- (b3) Calculations of the transmitted probe signals corresponding to the results in (a1)-(a3)[70]

3. Phase Control of FWM and Fluorescence Channels

As described in the previous section, the fluorescence and the FWM signals can be effectively modulated by dressed field frequency detuning and power. Most recently, we found a new modulation method in which dark state and bright state can be affected by the relative phase of dressing field. In this section, we demonstrate the switch between bright and dark states by controlling the relative phase in a four-level ^{85}Rb atomic vapor, which can be realized in experiment by changing the angle α (For special illustration of α, please see Ref. [1]) between incident field and the cell of atomic vapor. In the relative phase control, the enhancement and suppression conditions of the measured signals are significantly modified, and therefore we can effectively modulate the transmitted probe, FWM and fluorescence signals. The results of this section are based on Ref. [1].

As described in section I, the single-photon fluorescence signal R_0 can be obtained as $\rho_{11}^{(2)} = -|G_1|^2(\Gamma_{11}d_1)$ via $\rho_{00}^{(0)} \xrightarrow{\omega_1} \rho_{10}^{(1)} \xrightarrow{-\omega_1} \rho_{11}^{(2)}$. Such expression can be doubly dressed as $\rho_{11DD}^{(2)} = -|G_1|^2/[\Gamma_{11}(d_1+|G_3|^2/d_3+|G_2|^2\mathrm{e}^{i\Delta\Phi}/d_2)]$. The two-photon fluorescence signal R_2 can be obtained as $\rho_{22}^{(4)} = |G_1|^2|G_2|^2/\Gamma_{22}d_1d_2d_4$ via $\rho_{00}^{(0)} \xrightarrow{\omega_1} \rho_{10}^{(1)} \xrightarrow{\omega_2} \rho_{20}^{(2)} \xrightarrow{-\omega_1} \rho_{21}^{(3)} \xrightarrow{-\omega_2} \rho_{22}^{(4)}$, which can be modified as $\rho_{22DD}^{(4)} = |G_1|^2|G_2|^2/[\Gamma_{22}d_1d_4(d_2 + |G_2|^2\mathrm{e}^{i\Delta\Phi}/(d_1 + |G_3|^2/d_3))]$ with self- and external- dressing effects. The other two-photon fluorescence signal R_1 is similar to R_2. According to the expressions above, it is obvious that the dressing effect can be modulated by manipulating the relative phase $\Delta\Phi$, and so the switch between bright and dark states could be achieved. In experiment, $\Delta\Phi$ is controlled by changing the angle α (the relationship between α and $\Delta\Phi$ can be found in Ref. [1]).

When blocking $\boldsymbol{E}_3$ and $\boldsymbol{E}_3^{'}$, we first show the evolutions of the transmitted probe, FWM and fluorescence signals under three typical values of $\Delta\Phi$, as shown in Figs. 42(a1)sim(a3). Under the normal configuration where $\alpha = 0$, the relative phase $\Delta\Phi = 0$ corresponds to the factor $\mathrm{e}^{i\Delta\Phi} = 1$. Therefore, the dressing terms will degenerate to normal ones which have been investigated in Ref. [70].

The signals under such normal condition is depicted in Fig. 39 (a1), from which we can see an EIT window appearing at $\Delta_1 = -\Delta_2$ in the transmitted probe signal, relative lower FWM signal $\boldsymbol{E}_{F2}$ falling into this EIT window, and the two-photon fluorescence signal R_2 revealing as a sharp peak on the big background of single-photon fluorescence signal R_0, also falling within the EIT window. With $\Delta\Phi$ changed to $-\pi/2$ (Fig. 39 (a2)), the EIT window in the transmitted probe signal almost disappears and a small EIA dip arises. When $\Delta\Phi$ further changes to $-\pi$ (Fig. 39 (a3)), a strong EIA dip appears. Such switch between dark (EIT) and bright (EIA) states is for the reason that the dressing effect gets modulated as $\Delta\Phi$ is altered, denoting by the dressing term with a phase factor $|G_2|^2\mathrm{e}^{i\Delta\Phi}/d_2$ in $\rho_{10SD}^{(1)}$. To illustrate such phase controlled switch more clearly, we present the corresponding calculations of the transmitted probe signal in Fig. 39 (b). For $\Delta\Phi = 0$, the dressing term $|G_2|^2\mathrm{e}^{i\Delta\Phi}/d_2$ behaves positive (satisfying suppression condition) and normal dark (EIT) state appears (Fig. 39(b1)); for $\Delta\Phi = -\pi$, the dressing term behaves negative (satisfying enhancement condition) and so the dark (EIT) state switches to bright (EIA) state (Fig. 39 (b3)); for $\Delta\Phi = -\pi/2$, the transitional partial EIT/EIA could be seen (Fig. 39 (b2)). This dark/bright state switch could result in the modulation of FWM and fluorescence signals. For the

FWM signal $\boldsymbol{E}_{F2}$, it gets increased when $\Delta\Phi = -\pi/2$ (Fig. 39 (a2)) compared with that when $\Delta\Phi = 0$ (Fig. 39 (a1)), since the arising enhancement dressing effect of $\boldsymbol{E}_2$ ($\boldsymbol{E}_2^{'}$); and gets decreased again when $\Delta\Phi = -\pi$, due to strong absorption. For the two-photon fluorescence signal (in corresponding to EIA), its intensity could be observed increasing straightly from Fig. 39 (a1) to 39 (a3).

In summary, we have discussed the phase control of the switch between bright and dark states in the FWM and fluorescence channels in atomic vapors. Pure dark state can be switched to pure bright state by controlling the relative phase from 0 to $-\pi$. Such phase controlled switch could have potential applications in optical communication and quantum information processing when utilized in solid material such as Pr-doped YSO crystals.

B. MWM Process in Ring Optical Cavity

In this section, we consider MWM process in the ring resonator cavity. First, a brief discussion of the relation between atom-cavity coupling strength and cavity mode splitting, and how the intensities of input and output are effected by atom-cavity coupling strength is given. Next, noise squeezing with nonlinear media in the ring cavity is studied. As an important entanglement light source, squeezed light field with FWM process will be also briefly discussed.

1. The Competition between VRS and OB of MWM in Ring Cavity

Vacuum Rabi splitting (VRS) has been reported when single two-level atom and N two-level atoms are strongly coupled with cavity mode. The frequency distance of the VRS are $2g$ and $2G$ in above two atom-cavity systems, where g and $G = g\sqrt{N}$ are single- and multi-atom coupling strength, respectively. The coherently prepared atoms-cavity system will also result in the intra-cavity EIT results, optical bistability (OB) and multi-stability behavior, which can deduce close contact between VRS and OB behavior.

In the following, we will present investigation of the relationship between the VRS and OB of the generated MWM cavity mode and achieve the goal to control VRS and OB simultaneously through the coherent control of dark and bright states and get the inclined VRS.

As shown in Fig. 40, the coupled atom-cavity system consists of rubidium atoms confined in the four-mirror-formed ring cavity, in which only the generated FWM (SWM) signal can form the cavity mode. Figure 41 gives the transmission spectra of FWM

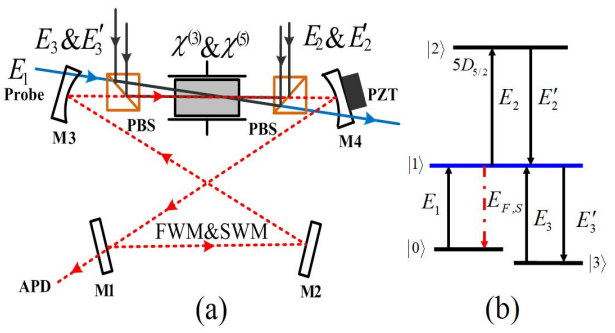

FIG. 40. (a) A scheme of a ring cavity containing the four-level atoms. (b) Scheme of four-level atomic system

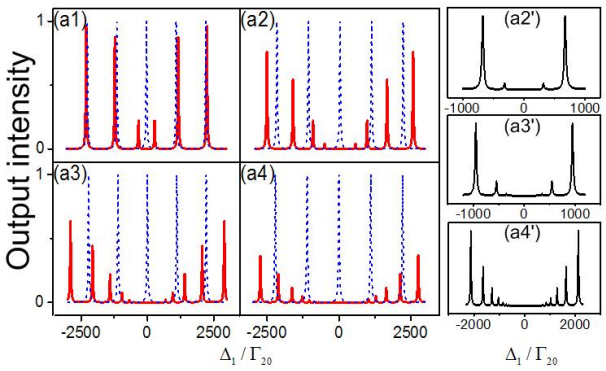

FIG. 41. (a1)-(a4) Solid curves are transmission spectra of the generated FWM cavity mode with N increasing. Dashed curves are the transmission spectra of empty cavity. The illustrations (a2′)-(a4′) FWM cavity mode transmissions in smaller regions corresponding to (a2)-(a4)

$(\boldsymbol{E}_1, \boldsymbol{E}_2, \boldsymbol{E}_2^{'})$ cavity mode, containing splitting positions and height of the multi-mode. For empty cavity, the cavity transmission spectra has Lorenzian shape and equal mode spacing (free spectral range $\Delta_{\rm FSR}$), shown as the dashed curves in Fig. 41. For the coupled atom-cavity system, not only the zero-order longitudinal mode is split with symmetrical center $\Delta_1 = 0$ (Fig. 41 (a1)), but also high-order modes are split by the cavity field when increasing the coupling strength $g\sqrt{N}$ to near or larger than $\Delta_{\rm FSR}$, as the solid curves shown in Figs. 41 (a2)sim(a4).

Next, the input-output intensity relationship under steady-state condition is shown in Fig. 42, which displays OB behavior of the transmitted FWM cavity mode influenced by dark state. In detail, Fig. 42 (a) illustrates the output intensity of FWM cavity mode versus probe input intensity (I_i) and detuning Δ_1, which represents the modulation of VRS in frequency domain and input-output relationship (OB behavior) simultaneously. With I_i increased, the spectra of the transmitted FWM cavity mode expanded rapidly when Δ_1 is scanned, as shown in Fig. 42 (b). Figure

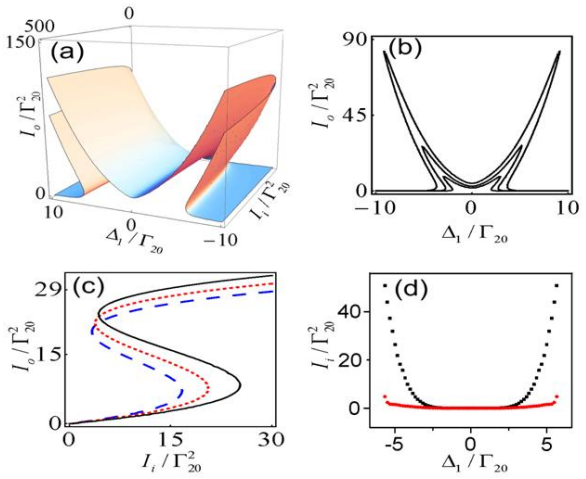

FIG. 42. The theoretically calculated input-output intensity relationship of the system. (a) FWM transmission output changes with both probe detuning and probe input intensity; (b) FWM transmission output with probe detuning at different probe input intensity; (c) OB at different probe detuning; (d) probe input intensity versus probe detuning with the dots of up branch standing for the right OB threshold of the OPA FWM process and dots of down branch standing for the left one

42 (c) obviously shows OB hysteresis cycle and the threshold of the optical parametric amplifier (OPA) FWM process, and reveals that the increased $|\Delta_1|$ can result in a significant change of the OB behavior with the increasing of right OB threshold value. Finally, Fig. 42 (d) displays the OB threshold values at different Δ_1, in which the left OB threshold value shifts slowly while the right one shifts sharply. Moreover, Fig. 42 (d) directly predicts there is no OB at or close to the position of dark state ($\Delta_1/\Gamma_{20} = 0$), which results from disappeared linear dispersion at $\Delta_1/\Gamma_{20} = 0$ by the interference between two possible absorption channels $|0\rangle \rightarrow |\pm\rangle$ induced by g^2N.

We have discussed the control of the multi-dressed VRS and OB behavior of transmitted cavity MWM signal. We find that the VRS results from the atom-cavity collective effect induced by high atom density while the OB behavior results from the sufficiently strong feedback effect.

2. Squeezed Noise Power with MWM in Cavity

The quantum correlations have been revealed in the output and idler signals from type-I and type-II[3,4] OPA inside an optical cavity, which have attracted increasing interests recently. Moreover, the FWM and SWM processes, which are assisted by the EIT in multi-level atomic systems, are efficient sources for squeezed radiation and correlated photons. Recent experiments have demonstrated the slowing down[5~7], storage and retrieval[8,9] of squeezed states of light through EIT in multi-level atomic systems[10~12], which are important to implement quantum network protocol[13,14].

In this section, we theoretically investigate the quantum correlations (noise power) of the generated FWM and SWM signals inside an optical cavity, in which the generated FWM signal can be considered as the input field to participate in SWM nonlinear process, and vice versa. These processes can be expressed with interaction Hamiltonian $H_{\rm int} = i\hbar\kappa\hat{a}_{\rm F}^{\dagger}\hat{a}_{\rm S}^{\dagger} + c.c.$, where $\kappa = \chi^{(3)}E_2^2 + \chi^{(5)}E_2^2E_3^2$ is the nonlinear coupling coefficient proportional to the susceptibilities ($\chi^{(3)}$ and $\chi^{(5)}$) and the amplitudes ($\boldsymbol{E}_2$ and $\boldsymbol{E}_3$) of the other two intensive coherent fields, $\hat{a}_{\rm F}$ and $\hat{a}_{\rm S}$ are annihilation operators of the generated FWM and SWM fields. For random annihilation operator, it can be described with amplitude $\hat{x}$ and phase $\hat{y}$ as quadrature components $\hat{a} = (\hat{x} + i\hat{y})/2$, in which $\hat{x}$ and $\hat{y}$ satisfy the canonical commutation relation $[\hat{x}, \hat{y}] = 2i$.

The equations of motion for the two cavity modes ($\hat{a}_{\rm F}$ and $\hat{a}_{\rm S}$) can be obtained by solving the Langevin equation:

$$\frac{{\rm d}\hat{a}_{\rm F}}{{\rm d}t} = -i(\Delta - \frac{ck_{\rm F}}{n_{0\rm F}}n_{1\rm F})\hat{a}_{\rm F} - (\gamma + \gamma_{\rm c})\hat{a}_{\rm F} + \kappa\hat{a}_{\rm S}^{\dagger} + \sqrt{2\gamma}\hat{a}_{\rm F}^{\rm in} + \sqrt{2\gamma_{\rm c}}\hat{c}_{\rm F} \quad (30)$$

$$\frac{{\rm d}\hat{a}_{\rm S}}{{\rm d}t} = -i(\Delta - \frac{ck_{\rm S}}{n_{0\rm S}}n_{1\rm S})\hat{a}_{\rm S} - (\gamma + \gamma_{\rm c})\hat{a}_{\rm S} + \kappa\hat{a}_{\rm F}^{\dagger} + \sqrt{2\gamma}\hat{a}_{\rm S}^{\rm in} + \sqrt{2\gamma_{\rm c}}\hat{c}_{\rm S} \quad (31)$$

where $\hat{a}_{\rm F}^{\rm in}$ ($\hat{a}_{\rm S}^{\rm in}$) and $\hat{a}_{\rm F}$ ($\hat{a}_{\rm S}$) represent input and intracavity FWM (SWM) mode, $\hat{c}_{\rm F}$ ($\hat{c}_{\rm S}$) is the vacuum mode coupled into the FWM (SWM) mode, Δ is cavity detuning, γ represents the same decay rate of FWM (SWM) signal, $\gamma_{\rm c}$ is the other losses in cavity. $n_{0\rm F}$ ($n_{0\rm S}$) and $n_{1\rm F}$ ($n_{1\rm F}$) are the linear refractive index at $\omega_{\rm F}$ ($\omega_{\rm S}$) of FWM (SWM) signal in vacuum and medium, respectively. In our energy level system, $k_{\rm F} = k_{\rm S} = \omega_1 n_0/c$ with $\omega_{\rm F} = \omega_{\rm S} = \omega_1$ and $n_{0\rm F} = n_{0\rm S} = n_0$ and $n_{1\rm F} = n_{1\rm S} = \sqrt{1 + {\rm Re}\chi^{(1)}_{\rm F(S)}}$, where the linear susceptibility is given by $\chi^{(1)}_{\rm F(S)} = D\rho^{(1)}_{10\rm F(S)}$ with $D = N\mu^2_{\rm F(S)}/(\hbar\epsilon_0 G_{\rm F(S)})$. $\mu_{\rm F(S)}$ is the dipole matrix element between the states coupled by $\boldsymbol{E}_{\rm F}(\boldsymbol{E}_{\rm S})$. Here, we can control the quantum correlations through the control of dark and bright states introduced from $n_{1\rm F}$ ($n_{1\rm S}$).

As shown by the dashed line in Fig. 43, when the other coherent fields are blocked, there are no generated FWM and SWM processes, so the quantum correlations of the FWM and SWM output modes correspond to the shot-noise limit (SNL). However, when the coherent fields are injected into the cavity, the noise power spectra of the quantum correla-

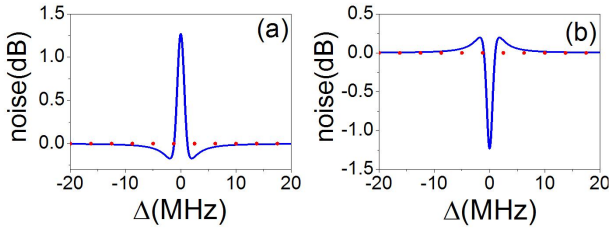

FIG. 43. The noise power spectra of the quantum correlations of the quadrature versus Δ. (a) for amplitude correlation and phase anticorrelation. (b) for amplitude anticorrelation and phase correlation

tion of the quadrature of the FWM and SWM output fields are observed shown as the solid lines in Fig. 43, which show that the amplitude correlation and the phase anticorrelation become more noisy (Fig. 43 (a)), while the degrees of the amplitude anticorrelation and phase correlation increase. These phenomena satisfy the Heisenberg uncertainty relation.

3. Generation of Three-Mode Continuous-Variable Entanglement with MWM

Quantum entanglement attracts great interests in recent years since it is the central resource for the applications in quantum communication and computation. Bipartite continuous-variable (CV) entanglement was experimentally obtained by Ou *et al.*[15~17] and multipartite entangled state was also produced by using one single-mode squeezed state and linear optics[18~20]. In this section, we will consider the quantum nature of the pump in above-threshold OPA.

Here, we consider two beams, a pump field ($\hat{a}_{\rm p}$) with frequency $\omega_{\rm p}$ and a probe field ($\hat{a}_1$) (considered as a weak injected field) with frequency ω_1, entering into the optical cavity, shown in Fig. 41. The Stokes ($\hat{a}_{\rm S}$) and anti-Stokes ($\hat{a}_{\rm AS}$) fields with frequencies $\omega_{\rm S}$ and $\omega_{\rm AS}$ can be generated simultaneously by the third-order nonlinear process. To produce a Stokes photon and an anti-Stokes photon, a pump photon and a probe photon must annihilate. For this scheme, the Hamiltonian of the free modes in the optical cavity can be written as $H_1 = \hbar\omega_{\rm p}\hat{a}_{\rm p}^{\dagger}\hat{a}_{\rm p} + \hbar\omega_1\hat{a}_1^{\dagger}\hat{a}_1 + \hbar\omega_{\rm S}\hat{a}_{\rm S}^{\dagger}\hat{a}_{\rm S} + \hbar\omega_{\rm AS}\hat{a}_{\rm AS}^{\dagger}\hat{a}_{\rm AS}$, and the interaction Hamiltonian in this third-order nonlinear process can be written as $H_2 = i\hbar\kappa(\hat{a}_{\rm p}\hat{a}_1\hat{a}_{\rm S}^{\dagger}\hat{a}_{\rm AS}^{\dagger} - \hat{a}_{\rm p}^{\dagger}\hat{a}_1^{\dagger}\hat{a}_{\rm S}\hat{a}_{\rm AS})$, where κ is the effective coupling constant proportional to the third-order nonlinear susceptibility ($\chi^{(3)}$). Moreover, the Hamiltonian for the external inputs of the pump and probe fields is given by $H_3 = i\hbar(\epsilon_{\rm p}\hat{a}_{\rm p}^{\dagger} - \epsilon_{\rm p}^{*}\hat{a}_{\rm p}) + i\hbar(\epsilon_1\hat{a}_1^{\dagger} - \epsilon_1^{*}\hat{a}_1)$, where $\epsilon_{\rm p}$ and ϵ_1 are the classical pump and probe field amplitudes. The losses of these modes in cavity are given by $L_i\hat{\rho} = \gamma_i(2\hat{a}_i\hat{\rho}\hat{a}_i^{\dagger} - \hat{a}_i^{\dagger}\hat{a}_i\hat{\rho} - \hat{\rho}\hat{a}_i^{\dagger}\hat{a}_i)$

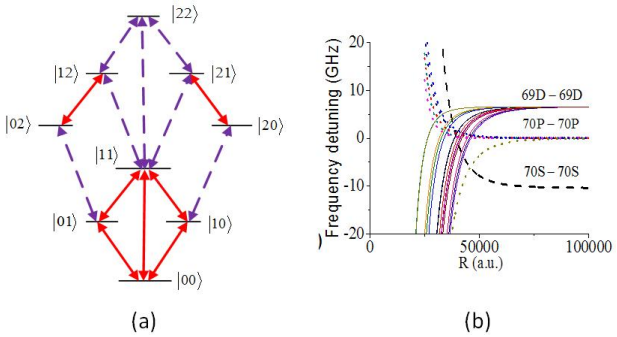

FIG. 44. (a) The diatomic systems consisting of 3×3. (b) The energy level shift curves for different symmetries of 70s-70s (dashed lines), 70p-70p (dotted lines) and 69d-69d (solid lines) of rubidium

($i = {\rm p}, 1, {\rm S}, {\rm AS}$), where γ_i is the damping constant for these cavity modes. Based on the above equations, one can investigate the entanglement characteristics of our scheme. Meanwhile, we can also introduce the effect of dark state to control the entanglement between these cavity modes.

We have considered a scheme to directly produce bright three color CV entanglement by OPA FWM process above-threshold. In our scheme, three color entangled beams can be produced $\chi^{(3)}$ nonlinear process, in which the nonlinear interaction and conversion efficiency can be enhanced through dark state.

C. MWM with Rydberg Blockade

With the development of modern laser cooling and trapping techniques, the so-called ultra-cold Rydberg gases and plasmas have been experimentally created, in which the atomic or plasmic density is very high and the Rydberg interaction becomes very strong[21~24], which attracts more and more attention due to their wide range of applications, such as quantum computing and scalable quantum information processing[24,25]. Among such applications, it has been proposed to realize the quantum logic gates by employing the sensitivity of the highly excited state energy to the interaction between neigh boring Rydberg atoms[26,27]. Also, the phenomena related to atomic coherence, such as coherent population trapping[28], stimulated Raman adiabatic passage[29] have been demonstrated in Rydberg atomic assemble. Such progresses give the possibility of controlling the dressed MWM process by the Rydberg blockade.

It is well known that the probe transmission, and enhancement and suppression of FWM signal can be controlled by the dressing effect of light field which modifies the unperturbed levels significantly[2,30,31] and depends on the detuning of dressing field strongly.

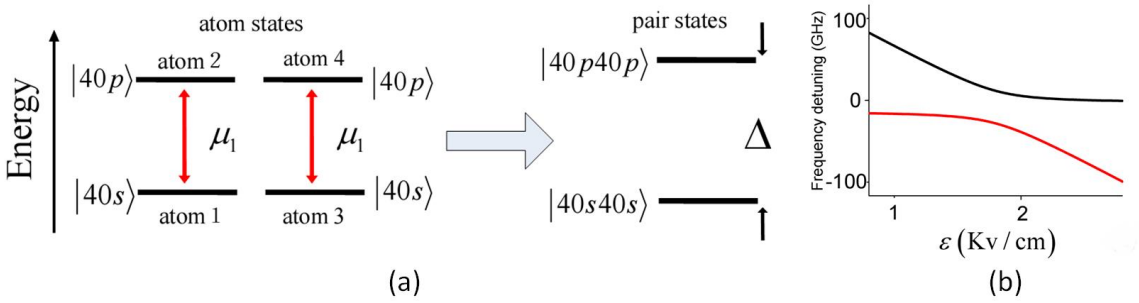

FIG. 45. (a) The energy levels of a quadratomic system in atom states; μ_1 is the dipole matrix element between $|40s\rangle$ and $|40p\rangle$. The right panel illustrates the corresponding energy levels in pair sates, in which Δ is the energy gap between $|40s40s\rangle$ and $|40p40p\rangle$. The eigen-frequencies of the two levels $\boldsymbol{E}_+(R)$ (the upper curve) and $\boldsymbol{E}_-(R)$ (the lower curve) versus ϵ (R fixed) with both the primary and secondary Rydberg blockades being considered

As the Rydberg blockade could shift energy levels, it can modulate the probe transmission and FWM signal via the modified dressing field detuning. Our work is focused on the MWM process under the modulation of both the dressing effect and Rydberg blockade.

In the follwing, we will introduce that the principle of how to control the probe transmission and MWM processes by the interaction between the dressing effect and primary blockad (or between the dressing effect and secondary blockade).

For two atoms with Rydberg levels, there exists considerable interaction between them, and therefore they constitute a diatomic system, in which the atomic coherence and FWM can occur. For two single atoms with the three-level subsystem ($|0\rangle \rightarrow |1\rangle \rightarrow |2\rangle$), 3×3=9 energy levels will be generated in the corresponding diatomic system, as shown in Fig. 44 (a). Due to the long-range interaction potential between Rydberg atoms with high principal quantum number n, there will be an energy level shift from the unperturbed energy level. Such interaction-induced energy shift is called as blockade effect. In Fig. 45 (b), the energy level shifts around $n = 70$ in Rubidium are displayed. The inter-nuclear distance R can be experimentally controlled by changing the atomic intensity, i.e., the cooling conditions in magneto-optical trap in ultra-cold gas or the temperature in hot atom vapor, and such level shift can effectively influence the dressing effect and therefore the MWM process.

Furthermore, if the Rydberg energy level of a diatomic system has strong probability of dipole transiting to that of another diatomic system, the perturbation will make the eigen-frequency shift again, as shown in Fig. 45 (a), in which Δ is the energy gap between the levels without transition perturbation. We call this effect as the secondary blockade to distinguish from the first blockade. The eigen-frequancies of the perturbed system can be written as $\boldsymbol{E}_\pm = \Delta_{|ss\rangle\pm}(\epsilon) = \Delta(\epsilon)/2 \pm \sqrt{(\Delta(\epsilon/2))^2 + (\mu_1^2/R^3)^2}$, which is obviously related to Δ and equivalent to the energy level shift after twice blockade. Here, μ_1 is the transition dipole moment between two diatomic levels. Moreover, Δ can be changed by the external electric filed intensity ϵ. Therefore, the energy level shift based on primary and secondary Rydberg interactions can also be Δ-dependent, as shown in Fig. 45 (b), in which the upper curve is for $\Delta_{|ss\rangle+}(\epsilon)$, and the lower for $\Delta_{|ss\rangle-}(\epsilon)$. Therefore, the dressed FWM processes can be also controlled by tuning ϵ directly.

In recent works, we have proposed a scheme to control the MWM signal in Rydberg atoms by the interaction between the dressing effect and Rydberg blockade. In the diatomic system, the primary blockade can be employed to modulate the enhancement, suppression and avoided crossing of doubly dressed FWM and singly dressed SWM signals, by controlling the atomic internuclear distance. In the quadr-atomic system, secondary blockade occurs and besides the internuclear distance, the external electric field intensity can be also exploited to effectively control the enhancement and suppression of MWM signals. Moreover, we have also demonstrated the anti-blockade effect, i.e., the elimination of primary blockade effect in MWM process, through the counteraction between Rydberg blockade and dressing effect from light field. Such investigation can have potential applications in the quantum computing with Rydberg atom as the carrier of qubit.

VI. SUMMARY

MWM process has shown profound impact upon optical science. Hopefully, we have succeeded in explaining the relationship between MWM and the earlier related ideas of coherent preparation of atoms by fields and especially linked it with the concept of the dressed state. Based on this relationship, the quantum control of MWM in many domains have been achieved, as presented in the main body. Specifically, we have

presented the coexisting and controllable MWM, as well as the mutual competition with energy exchange and spatio-temporal interference between coexisting MWM processes. Also, the spatial shift and splitting of MWM, as well as spatial gap solitons, vortex solitons, charged dipole-mode solitons, and 2D surface solitons are described. Furthermore, many nonlinear optical phenomena related to the quantum nature of light, such as fluorescence accompanying with MWM, MWM process in cavity, correlated and squeezed light and MWM in Rydberg atomic system have been investigated and presented. Coherent control of MWM provides a new way to change the optical characteristics of matter, and therefore paves a way to alter the propagation of optical fields and enhances the generation of new fields.

ACKNOWLEDGMENTS

This work was supported by the National Basic Research Program of China (2012CB921804) and NSFC (10974151, 61078002, 61078020, 11104214, 61108017, 11104216, and 61205112).

REFERENCES

[1] Harris S E. *Physics Today*, 1997, **50**: 36-42
[2] Gea-Banacloche J, Li Y, Jin S, Xiao M. *Phys. Rev. A*, 1995, **51**: 576-584
[3] Agarwal G S, Harshawardhan W. *Phys. Rev. Lett.*, 1996, **77**: 1039-1042
[4] Zibrov A S, Ye C Y, Rostovtsev Y V, Matsko A B, Scully M O. *Phys. Rev. A*, 2002, **65**: 043817
[5] Li Y, Xiao M. *Opt. Lett.*, 1996, **21**: 1064-1066
[6] H. Kang, G. Hernandez, Y. Zhu, Superluminal and slow light propagation in cold, Physical Review A, 70 (2004) 061804
[7] Kang H, Hernandez G, Zhu Y. *Phys. Rev. Lett.*, 2004, **93**: 073601
[8] Zuo Z, Sun J, Liu X, Jiang Q, Fu G, Wu L, Fu P. *Phys. Rev. Lett.*, 2006, **97**: 193904
[9] Ma H, de Araújo C B. *Phys. Rev. Lett.*, 1993, **71**: 3649-3652
[10] Zhang Y, Brown A W, Xiao M. *Phys. Rev. Lett.*, 2007, **99**: 123603
[11] Wu Z, Yuan C, Zhang Z, Zheng H, Huo S, Zhang R, Wang R, zhang Y. *Europhys Lett.*, 2011, 94: 64005
[12] Zhang Y, Brown A W, Xiao M. *Opt. Lett.*, 2007, **32**: 1120-1122
[13] Zhang Y, Xiao M. *Appl. Phys. Lett.*, 2007, **90**: 111104
[14] Zhang Y, Khadka U, Anderson B, Xiao M, *Phys. Rev. Lett.*, 2009, **102**: 13601
[15] Chen C, Yin Y Y, Elliott D S. *Phys. Rev. Lett.*, 1990, **64**: 507-510
[16] Yamazaki R, Elliott D S. *Phys. Rev. Lett.*, 2007, **98**: 053001
[17] Dupont E, Corkum P B, Liu H C, Buchanan M, Wasilewski Z R. *Phys. Rev. Lett.*, 1995, **74**: 3596-3599
[18] Saito S, Ohmine I, *Phys. Rev. Lett.*, 2002, **88**: 207401
[19] Agrawal G P, *Phys. Rev. Lett.*, 1990, **64**: 2487-2490
[20] Stentz A J, Kauranen M, Maki J J, Agrawal G P, Boyd R W, *Opt. Lett.*, 1992, **17**: 19-21
[21] Hickmann J M, Gomes A S L, de Araújo C B. *Phys. Rev. Lett.*, 1992, **68**: 3547-3550
[22] Desyatnikov A S, Sukhorukov A A, Kivshar Y S, *Phys. Rev. Lett.*, 2005, **95**: 203904
[23] Bennink R S, Wong V, Marino A M, Aronstein D L, Boyd R W, Stroud C R, Lukishova Jr S, Gauthier D J. *Phys. Rev. Lett.*, 2002, **88**: 113901
[24] Wang H, Goorskey D, Xiao M. *Phys. Rev. Lett.*, 2001, **87**: 073601
[25] Harris S E, Yamamoto Y. *Phys. Rev. Lett.*, 1998, **81**: 3611-3614
[26] Truscott A G, Friese M E J, Heckenberg N R, Rubinsztein-Dunlop H. *Phys. Rev. Lett.*, 1999, **82**: 1438-1441
[27] Jain M, Xia H, Yin G Y, Merriam A J, Harris S E. *Phys. Rev. Lett.*, 1996, **77**: 4326-4329
[28] Firstenberg O, Shuker M, Davidson N, Ron A. *Phys. Rev. Lett.*, 2009, **102**: 043601
[29] Zhang Y, Nie Z, Zheng H, Li C, Song J, Xiao M. *Phys. Rev. A*, 2009, **80**: 013835
[30] Zhang Y, Zuo C, Zheng H, Li C, Nie Z, Song J, Chang H, Xiao M. *Phys. Rev. A*, 2009, **80**: 055804
[31] Kivshar Y S, Agrawal G P. *Academic Press*, 2003
[32] Bortman-Arbiv D, Wilson-Gordon A D, Friedmann H. *Phys. Rev. A*, 1998, **58**: R3403-R3406
[33] Chen Z, Martin H, Eugenieva E, Xu J, Yang J. *Opt. Express*, 2005, **13**: 1816-1826
[34] Zhang P, Liu S, Zhao J, Lou C, Xu J, Chen Z. *Opt. Lett.*, 2008, **33**: 878-880
[35] Neshev D, Sukhorukov A A, Hanna B, Krolikowski W, Kivshar Y S. *Phys. Rev. Lett.*, 2004, **93**: 083905
[36] Eggleton B J, Slusher R E, de Sterke C M, Krug P A, Sipe J E. *Phys. Rev. Lett.*, 1996, **76**: 1627-1630
[37] Eiermann B, Anker T, Albiez M, Taglieber M, Treutlein P, Marzlin K P, Oberthaler M K, *Phys. Rev. Lett.*, 2004, **92**: 230401
[38] André A, Lukin M D. *Phys. Rev. Lett.*, 2002, **89**: 143602
[39] Swartzlander G A, Law C T. *Phys. Rev. Lett.*, 1992, **69**: 2503-2506
[40] Gorbach A V, Skryabin D V, Harvey C N. *Phys. Rev. A*, 2008, **77**: 063810
[41] Gorbach A V, Skryabin D V. *Phys. Rev. Lett.*, 2007, **98**: 243601
[42] Krolikowski W, Ostrovskaya E A, Weilnau C, Geisser M, McCarthy G, Kivshar Y S, Denz C, Luther-Davies B. *Phys. Rev. Lett.*, 2000, **85**: 1424-1427
[43] Yang J, Makasyuk I, Bezryadina A, Chen Z. *Opt. Lett.*, 2004, **29**: 1662-1664
[44] Chen Z, Bezryadina A, Makasyuk I, Yang J. *Opt. Lett.*, 2004, **29**: 1656-1658
[45] Makris K G, Suntsov S, Christodoulides D N, Stegeman G I, Hache A. *Opt. Lett.*, 2005, **30**: 2466-2468
[46] Suntsov S, Makris K G, Christodoulides D N, Stegeman G I, Haché A, Morandotti R, Yang H, Salamo

G, Sorel M. *Phys. Rev. Lett.*, 2006, **96**: 063901
[47] Kivshar Y. *Nature Phys.*, 2006, **2**: 729-730
[48] Neto A H C, Guinea F, Peres N, Novoselov K, Geim A. *Rev. Mod. Phys.*, 2009, **81**: 109
[49] Kivshar Y S. *Laser Phys. Lett.*, 2008, **5**: 703-713
[50] Yeh P, Yariv A, Hong C S. *J. Opt. Soc. Am.*, 1977, **67**: 423-438
[51] Alfassi B, Rotschild C, Manela O, Segev M, Christodoulides D N. *Phys. Rev. Lett.*, 2007, **98**: 213901
[52] Sukhorukov A A, Neshev D N, Dreischuh A, Fischer R, Ha S, Krolikowski W, Bolger J, Mitchell A, Eggleton B J, Kivshar Y S. *Opt. Express*, 2006, **14**: 11265-11270
[53] Chong A, Renninger W H, Christodoulides D N, Wise F W. *Nat. Photonics*, 2010, **4**: 103-106
[54] Rosberg C R, Neshev D N, Krolikowski W, Mitchell A, Vicencio R A, Molina M I, Kivshar Y S. *Phys. Rev. Lett.*, 2006, **97**: 83901
[55] Wang X, Bezryadina A, Chen Z, Makris K, Christodoulides D, Stegeman G. *Phys. Rev. Lett.*, 2007, **98**: 123903
[56] Heinrich M, Kartashov Y, Ramirez L, Szameit A, Dreisow F, Keil R, Nolte S, Tünnermann A, Vysloukh V, Torner L. *Phys. Rev. A*, 2009, **80**: 06383
[57] Zhang Y, Wang Z, Zheng H, Yuan C, Li C, Lu K, Xiao M. *Phys. Rev. A*, 2010, **82**: 053837
[58] Zhang Y, Wang Z, Nie Z, Li C, Chen H, Lu K, Xiao M. *Phys. Rev. Lett.*, 20011, **106**: 093904
[59] Lukin M D, Yelin S F, Fleischhauer M, Scully M O. *Phys. Rev. A*, 1999, 60: 3225-3228
[60] Yan M, Rickey E G, Zhu Y. *Phys. Rev. A*, 2001, **64**: 013412
[61] Joshi A, Xiao M. *Phys. Rev. A*, 2005, **72**: 062319
[62] Joshi A, Xiao M. *Phys. Rev. A*, 2005, **71**: 041801
[63] Zhang Y, Xiao M. *Opt. Express*, 2007, **15**: 7182-7189
[64] Zhang Y, Anderson B, Xiao M. *J. Phys B-At. Mol. Opt.*, 2008, **41**: 045502
[65] Nie Z, Zheng H, Li P, Yang Y, Zhang Y, Xiao M. *Phys. Rev. A*, 2008, **77**: 063829
[66] Li C, Zheng H, Zhang Y, Nie Z, Song J, Xiao M, *Appl. Phys. Lett.*, 2009, **95**: 041103
[67] Wang Z, Zhang Y, Chen H, Wu Z, Fu Y, Zheng H. *Phys. Rev. A*, 20011, **84**: 013804
[68] Zhang Y, Nie Z, Wang Z, Li C, Wen F, Xiao M. *Opt. Lett.*, 2010, **35**: 3420-3422
[69] Zhang Y, Li P, Zheng H, Wang Z, Chen H, Li C, Zhang R, Xiao M. *Opt. Express*, 2011, **19**: 7769-7777
[70] Li P, Zhao Z, Wang Z, Zhang Y, Lan H, Chen H, Zheng H. *Appl. Phys. Lett.*, 2012, **101**: 081107
[71] DBraje D A, Balić V, Goda S, Yin G, Harris S. *Appl. Phys. Lett.*, 2004, **93**: 183601
[72] van der Wal C H, Eisaman M D, André A, Walsworth R L, Phillips D F, Zibrov A S, Lukin M D. *Science*, 2003, **301**: 196-200
[73] Kuzmich A, Bowen W P, Boozer A D, Boca A, Chou C W, Duan L M, Kimble H J. *Nature*, 2003, **423**: 731-734
[74] Balić V, Braje D A, Kolchin P, Yin G, Harris S. *Phys. Rev. Lett.*, 2005, **94**: 183601
[75] Kolchin P, Du S, Belthangady C, Yin G Y, Harris S E. *Phys. Rev. Lett.*, 2006, **97**: 113602
[76] Yan H, Zhang S, Chen J, Loy M M, Wong G K L, Du S. *Phys. Rev. Lett.*, 2011, **106**: 033601
[77] Boyer V, Marino A, Lett P. *Phys. Rev. Lett.*, 2008, **100**: 143601
[78] Pooser R, Marino A, Boyer V, Jones K, Lett P. *Phys. Rev. Lett.*, 2009, **103**: 10501
[79] Boyer V, Marino A, Pooser R C, Lett P D. *Science*, 2008, **321**: 544-547
[80] Marino A, Pooser R, Boyer V, Lett P. *Nature*, 2009, **457**, 859-862
[81] Corzo N V, Marino A M, Jones K M, Lett P D. *Phys. Rev. Lett.*, 2012, **109**: 043602
[82] Glasser R T, Vogl U, Lett P D. *Phys. Rev. Lett.*, 2012, **108**: 173902
[83] Klinner J, Lindholdt M, Nagorny B, Hemmerich A. *Phys. Rev. Lett.*, 2006, **96**: 23002
[84] Hernandez G, Zhang J, Zhu Y. *Phys. Rev. A*, 2007, **76**: 053814
[85] Zhu Y, Gauthier D J, Morin S, Wu Q, Carmichael H, Mossberg T. *Phys. Rev. Lett.*, 1990, **64**: 2499-2502
[86] Thompson R, Rempe G, Kimble H. *Phys. Rev. Lett.*, 1992, **68**: 1132-1135
[87] Yu X, Xiao M, Zhang J. *Appl. Phys. Lett.*, 2010, **96**: 041101-041103
[88] Lane A, Reid M, Walls D. *Phys. Rev. Lett.*, 1988, **60**: 1940-1942
[89] Zukowski M, Zeilinger A, Weinfurter H. *Ann. Ny. Acad. Sci.*, 1995, **755**: 91-102
[90] Thompson J K, Simon J, Loh H, Vuletić V. *Science*, 2006, **313**: 74-77
[91] Xiong H, Scully M O, Zubairy M S. *Phys. Rev. Lett.*, 2005, **94**: 23601
[92] Wu H, Xiao M. *Phys. Rev. A*, 2009, **80**: 063415
[93] Tong D, Farooqi S, Stanojevic J, Krishnan S, Zhang Y, CôtéR, Eyler E, Gould P. *Phys. Rev. Lett.*, 2004, **93**: 63001
[94] Dudin Y, Kuzmich A. *Science*, 2012, **336**: 887-889
[95] Born M, Wolf E. *Principle of Optics*, ch. 10, in, New York: Pergamon Press, 1980
[96] Esq H F T, LXXVI. Facts relating to optical science. No. IV, *The London and Edinburgh Philosophical Magazine and Journal of Science*, 9 (1836) 401
[97] Rayleigh L. *Philos. Mag*, 1881, 11: 196-205
[98] Zhang Y, Wen J, Zhu S, Xiao M. *Phys. Rev. Lett.*, 2010, **104**: 183901
[99] Wen J, Zhang Y, Zhu S N, Xiao M. *JOSA B*, 2011, **28**: 275-280
[100] Wen J, Du S, Chen H, Xiao M. *Appl. Phys. Lett.*, 2011, **98**: 081108
[101] Patorski K. *Prog. Opt.*, 1989, **27**: 1-108
[102] Andre A, Lukin M. *Phys. Rev. Lett.*, 2002, **89**: 143602
[103] Shen Y R. The principles of nonlinear optics, New York, Wiley-Interscience, 1984, 575 p
[104] Boyd R W. *Nonlinear optics*, Academic Pr, 2003
[105] Christodoulides D N, Eugenieva E D.*Phys. Rev. Lett.*, 2001, **87**: 233901
[106] Fink Y, Winn J N, Fan S, Chen C, Michel J, Joannopoulos J D, Thomas E L. *Science*, 1998, **282**: 1679-1682
[107] Oulton R F, Sorger V J, Zentgraf T, Ma R M, Gladden C, Dai L, Bartal G, Zhang X. *Nature*, 2009, **461**: 629-632

Symbol

P	polarization	Λ	grating period
χ	susceptibility	$g\sqrt{N}$	coupling strength
k	wave vector	A	the envelope amplitude
$\boldsymbol{E}$	electric field intensity	$c_{m,n}$	the Fourier coefficient
ω	Frequency	μ	the dipole matrix element
G	Rabi Frequency	Δn	refractive index contrast
Δ	frequency detuning	α	the ellipse orientation
$\hat{\rho}$	atomic density	χ_m	Fourier coefficients of the susceptibility
P	power	Ω	the Raman resonant frequency
l	coherence length	$\delta k_{\perp}$	transverse propagation wave-vector
λ	wavelength	n^S	the self-Kerr nonlinear coefficient
N	atomic density	ϕ	the azimuthal coordinate
I	intensity	n^X	the cross-Kerr nonlinear coefficient
n_2	nonlinear index	m	the integer number
n_g	modified group index	ϕ_{NL}	phase shift
n_0	nonlinear index	H	Hamiltonian

Abbreviation

EIT	electromagnetically induced transparency
FWM	four-wave mixing
SWM	six-wave mixing
EWM	eight-wave mixing
SPM	self-phase modulation
XPM	cross-phase modulation
EISD	electromagnetically induced spatial dispersion
1D	one-dimensional
DDFWM	doubly dressed FWM
AT	Autler-Townes
SPDC	spontaneous parametric down-conversion
RWA	rotating-wave approximation
DSFD	double-sided Feynman diagrams
APD	avalanche photodiode detector
EIG	electromagnetically induced grating
EIL	electromagnetically induced lattice
PBG	photonic band gap
EIF	electromagnetically induced focusing
CQ	cubic-quintic
EID	electromagnetically induced diffraction
VRS	vacuum Rabi splitting
OB	optical bistability
SNL	shot-noise limit

原子介质中的多波混频相干控制

楼　兰[1]，问　峰[2]，秦勐哲[2]，贺嘉楠[2]，张彦鹏[2]，肖　敏[3]

1. 广东省公安消防总队，中国 广州 510640
2. 西安交通大学电子物理与器件教育部重点实验室 & 陕西省信息光子技术重点实验室，中国 西安 710049
3. 阿肯色大学物理系，费耶特维尔，美国 阿肯色 72701 & 南京大学固体微结构物理国家实验室，中国 南京 210093

摘要：多波混频是一种重要的非线性光学过程，其在非线性光学和量子信息科学中有重要的应用。本文详细讲述了该领域的进展。在频域中，首先通过电磁诱导透明在实验上得到了共存的四六波混频信号，继而观察到了它们之间伴随着能量交换和时空干涉的相互竞争。 此外，两个竞争的四六波混频之间的抑制增强以及相应的 AT 分裂也被实验证实了。 在空间域中，研究了因为两束泵浦光之间干涉导致的电磁诱导光栅，对多波混频信号的空间移动和分裂也进行了讨论，并且得到了带隙孤子，涡旋孤子，有荷偶极孤子，以及二维表面孤子。 这些概念可以扩展到量子领域，并且与之相关的一些效应具有研究价值。本文同时也讨论了多波混频在腔量子电动力学中，里德堡态中，以及全固态量子计算中的发展前景以及潜在应用。

关键词： 四波混频；六波混频；电磁诱导透明；腔；偶极孤子